

University of Cincinnati

Date: 3/10/2022

I, FNU Dileep Bengaluru Chandrashekar, hereby submit this original work as part of the requirements for the degree of Master of Science in Civil Engineering.

It is entitled:

Numerical Investigation of Local Buckling Behavior of High Strength Steel Wide Flange Columns

Student's name: **FNU Dileep Bengaluru Chandrashekar**

This work and its defense approved by:

Committee chair: Rachel Chicchi, Ph.D.

Committee member: Alireza Asgari Hadad, Ph.D.

Committee member: James Swanson, Ph.D.



41676

Numerical Investigation of Local Buckling Behavior of High Strength Steel Wide Flange Columns

A thesis submitted to the
Dept. of Civil and Architectural Engineering and Construction Management
In partial fulfillment of the requirements for the degree of
of
Master of Science in Civil Engineering
College of Engineering and Applied Sciences
University of Cincinnati

By



Dileep Bengaluru Chandrashekar
Bachelor of Technology in Civil Engineering
From PES University, Bengaluru, India

Committee Chair: Rachel Chicchi, Ph.D., PE, SE

Committee Members:

James A. Swanson, Ph.D.

Alireza A. Hadad, Ph.D.

March 2022

ABSTRACT

High strength structural steel (HS3), which in this context is being defined as steel with a yield strength greater than 65 ksi (450 MPa), has gained popularity worldwide in the building industry due to its superior strength to weight ratio, and satisfactory ductility and toughness. However, the use of HS3 steel for design as a structural member in the United States has been limited in part because of limitations and a lack of guidance within the *AISC Specification*. This study aims to evaluate the local buckling behavior of HS3 stub columns of grades 100 ksi (690 MPa), 120 ksi (800 MPa), 140 ksi (960 MPa) subjected to axial compression. This study also throws light on the interactive buckling behavior of 120 ksi HS3 columns subjected to axial compression. Finite element models were developed and validated in ABAQUS from preexisting experimental data to capture the local buckling behavior and interactive buckling behavior of HS3 wide flange stub columns.

A parametric study was conducted to investigate the effect of section slenderness on the local buckling behavior of the column. Three initial column sizes were used, and the web slenderness and flange slenderness were varied. The ultimate load capacity of these columns was investigated, and numerical results were then compared with the current local buckling design method in *AISC 360 (2016) Specification* for conventional steel. It was found that the design method in the *AISC Specification* nearly predicted the nominal strength of the HS3 column and can be used the design of HS3 wide flange columns of grade 100 ksi, 120 ksi and 140 ksi, respectively. During study of interactive buckling in 120 ksi built-up columns, it was found that the design method in the *AISC Specification* slightly overestimated the ultimate load capacity of the column specimen.

Blank Page

ACKNOWLEDGMENT

I would like to express my sincere gratitude to Dr. Chicchi for being my research guide and helping me in completing my thesis. I would also like to thank her for her research guidance, patience, and support during my research time. Her valuable and engaging lectures on the design of steel structures and the steel design project have been extremely helpful in my research work. Without her, this research work would not have been possible.

I would like to thank Dr. Swanson and Dr. Hadad for their valuable advice and comments during the proposal. I would like to acknowledge Dr. Swanson for his valuable lectures on finite element modeling which was extremely helpful in my research work. Special thanks to Dr. Rassati and Dr. Swanson for their valuable feedback on my research work. I would also like to thank SSRC for accepting my conference paper and allowing me to present my paper.

I would also like to thank Varun Aprameya for his support in ABAQUS and for helping me to understand finite element analysis. Special thanks to Varun Aprameya, Eshaan Khanapuri, Shashank Iyengar, and Harsh Dave for their moral support during my research work. I would like to acknowledge Jyothindra Chettri, Nikki Baider, and Varun Aprameya for their valuable comments on my research work.

Finally, I would like to thank my family for supporting me all these times. Especially my mother and father without whom my adventure at the University of Cincinnati would not have been possible.

TABLE OF CONTENTS

ABSTRACT.....	i
ACKNOWLEDGMENT	iii
TABLE OF CONTENTS	iv
LIST OF FIGURES	vii
LIST OF TABLES	xii
NOTATIONS AND SYMBOLS	xiv
1.0 INTRODUCTION.....	1
1.1 RESEARCH OBJECTIVE	6
1.2 THESIS OVERVIEW	6
2.0 LITERATURE REVIEW	8
2.1 EXPERIMENTAL STUDIES.....	8
2.2 ANALYTICAL STUDIES	12
3.0 NUMERICAL MODEL	18
3.1 DEVELOPMENT OF FE MODEL	18
3.1.1 PARTITIONS.....	18
3.1.2 MATERIAL AND BOUNDARY CONDITIONS.....	20
3.1.3 INITIAL GEOMETRIC IMPERFECTIONS.....	20
3.1.4 RESIDUAL STRESSES AND DISPLACEMENT CONTROL METHOD.....	22

3.2 VALIDATION OF FE MODEL.....	24
3.2.1 EFFECT OF RESIDUAL STRESSES AND IMPERFECTIONS	24
3.2.2 COMPARISON OF ABAQUS RESULTS	27
4.0 PARAMETRIC STUDY OF HS3 COLUMNS	34
4.1 LOCAL BUCKLING OF BUILT-UP W SHAPES	34
4.1.1 PARAMETERS.....	34
4.1.2 RESIDUAL STRESS	36
4.1.3 RESULTS	38
4.1.4 EVALUATION OF AISC DESIGN EQUATIONS	44
4.2 LOCAL BUCKLING OF ROLLED W SHAPES.....	51
4.2.1 PARAMETERS.....	51
4.2.2 RESIDUAL STRESS	52
4.2.3 RESULTS	54
4.2.4 EVALUATION OF AISC DESIGN EQUATIONS	61
4.2 INTERACTIVE BUCKLING OF BUILT-UP W SHAPES	66
5.0 CONCLUSIONS AND FUTURE WORK	73
5.1 FUTURE WORK	76
6.0 REFERENCES.....	77
APPENDIX A – RESIDUAL STRESSES	80
A.1 CALCULATION OF RESIDUAL STRESSES.....	80

A.1.1 Calculation of Residual Stresses for 140 ksi built-up specimen:	80
A.1.2 Calculation of Residual Stresses for 120 ksi built-up specimen:	83
A.1.3 Calculation of Residual Stresses for 100 ksi built-up specimen:	85
A.1.4 Calculation of Residual Stresses for 100 ksi hot-rolled specimen:	87
A.2 RESIDUAL STRESSES IN BUILT-UP W SHAPES	88
A.3 RESIDUAL STRESSES IN HOT-ROLLED W SHAPES	93
APPENDIX B – INITIAL GEOMETRIC IMPERFECTIONS	98
B.1 Permitted variation in length and camber in HS3 plates	98
B.2 Permitted variation in length, camber, and sweep in W shapes	101
APPENDIX C – AISC SLENDERNESS LIMITS	103
C.1 Section Slenderness Limit	103
C.2 Member Slenderness Limit	104
APPENDIX D – ABAQUS MACROS AND PYTHON CODE EDITING	105
APPENDIX E – CALCULATION OF NOMINAL COMPRESSIVE STRENGTH	121
APPENDIX F – AXIAL LOAD VS AXIAL DISPLACEMENT CURVES	124
F.1 Axial load vs axial deformation curves for built-up W shapes	124
F.2 Normalized axial load vs axial deformation for hot-rolled W shapes	127

LIST OF FIGURES

Fig. 1: Comparison of Stress-Strain curves of HS3 vs CMS steel - (Ban et al., 2018)	2
Fig. 2: Local Buckling mode observed in one of the test specimens. (Shi et al., 2015).....	5
Fig. 3: Interactive mode observed in one of the test specimens - (Cao et al., 2021).....	5
Fig. 4: Different types of HS3 column cross-section - (Rasmussen et al., 1992).....	9
Fig. 5: Test configuration of Axial Compression Test - (Shi et al., 2014)	10
Fig. 6: Experimental Setup for the study of Interactive Buckling - (Cao et al., 2021).....	11
Fig. 7: Three different sets of Finite Element Models - (Shi et al., 2011).....	12
Fig. 8: Design methods on the ultimate stress of flange of the wide flange section - (Shi et al., 2014).....	13
Fig. 9: Typical dimensional notations for the cross-sections modeled.....	19
Fig. 10: A FE model of 140 ksi stub column model showing partitions	19
Fig. 11: Coupled kinematic constraints in the FE model.....	20
Fig. 12: Mesh cross-section (left) and elevation (right) of the FE model.....	21
Fig. 13: First eigenmode for one of the FE models in 3D	21
Fig. 14: Axial load setup using displacement control method.....	22
Fig. 15: Axial load vs. axial deformation for I1 specimen	25
Fig. 16: Residual stress distribution in I2 FE model.....	25
Fig. 17: Axial load vs strain in lateral direction of flange for I1 specimen	27
Fig. 18: Axial load vs strain in lateral direction of web for I1 specimen	27
Fig. 19: Axial load vs. lateral deflection of flange for I1 specimen	28
Fig. 20: Axial load vs. lateral deflection of web for I1 specimen.....	28
Fig. 21: Axial load vs. strain in the lateral direction of flange for I2 specimen	29

Fig. 22: Axial load vs. strain in the lateral direction of web for I2 specimen.....	29
Fig. 23: Axial load vs. lateral deflection of flange for I2 specimen	30
Fig. 24: Axial load vs. lateral deflection of web for I2 specimen.....	30
Fig. 25: Axial load vs axial deformation for I3 specimen	31
Fig. 26: Axial load vs. axial deformation for I4 specimen	32
Fig. 27: Axial load vs. axial deformation for I5 specimen	32
Fig. 28: Local buckling mode observed in W12×12×0.4×0.4 (left) and W12×12×0.7×0.7 (right) sections.....	38
Fig. 29: Normalized axial load vs. axial deformation for W6×6 built-up stub columns of grade 100 ksi.....	39
Fig. 30: Normalized axial load vs. axial deformation for W12×12 built-up stub columns of grade 100 ksi.....	40
Fig. 31: Normalized axial load vs. axial deformation for W10×16 built-up stub columns of grade 100 ksi.....	40
Fig. 32: Normalized axial load vs. axial deformation for W6×6 built-up stub columns of grade 140 ksi.....	41
Fig. 33: Normalized axial load vs. axial deformation for W12×12 built-up stub columns of grade 140 ksi.....	42
Fig. 34: Normalized axial load vs. axial deformation for W10×16 built-up stub columns of grade 140 ksi.....	42
Fig. 35: Comparison of Axial load vs. axial deformation for built-up W12×12 with different steel grades	43

Fig. 36: Comparison of load ratio - P_u/P_n and interactive slenderness - $(\lambda_f/\lambda_{rf})(\lambda_w/\lambda_{rw})$ for built-up members.....	47
Fig. 37: Comparison of P_u (FE analysis) and P_n (AISC) for 100 ksi built-up members.....	48
Fig. 38: Comparison of P_u (FE analysis) and P_n (AISC) for 140 ksi built-up members.....	48
Fig. 39: Comparison of load ratio and interactive slenderness for 100 ksi built-up members	49
Fig. 40: Comparison of load ratio and interactive slenderness for 140 ksi built-up member.....	50
Fig. 41: Local buckling observed in W10×11×0.5×0.3 column - left (front view), right (top view)	54
Fig. 42: Flexural buckling observed in W10×11×1×0.6 column - left (3D view), right (side view)	55
Fig. 43: Axial load vs. axial deformation for W10×11 hot-rolled stub columns of grade 100 ksi	55
Fig. 44: Axial load vs. axial deformation for W12×12 hot-rolled stub columns of grade 100 ksi	56
Fig. 45: Axial load vs. axial deformation for W14×14 hot-rolled stub columns of grade 100 ksi	57
Fig. 46: Axial load vs. axial deformation for W10×11 hot-rolled stub columns of grade 120 ksi	57
Fig. 47: Axial load vs. axial deformation for W12×12 hot-rolled stub columns of grade 120 ksi	58
Fig. 48: Axial load vs. axial deformation for W14×14 hot-rolled stub columns of grade 120 ksi	58
Fig. 49: Comparison of Axial load vs. axial deformation for hot-rolled W12×12 with different steel grades	59
Fig. 50: Comparison of Axial load vs. axial deformation built-up W12×12 sections and hot-rolled W12×12 sections.....	60
Fig. 51: Comparison of load ratio - P_u/P_n and interactive slenderness - $(\lambda_f/\lambda_{rf})(\lambda_w/\lambda_{rw})$ for hot-rolled members.....	63
Fig. 52: Comparison of P_u (FE analysis) and P_n (AISC) for 100 ksi hot-rolled members	63

Fig. 53: Comparison of P_u (FE analysis) and P_n (AISC) for 120 ksi hot-rolled members	64
Fig. 54: Comparison of load ratio and interactive slenderness for 100 ksi hot-rolled members ..	65
Fig. 55: Comparison of load ratio and interactive slenderness for 120 ksi hot-rolled members ..	65
Fig. 56: Mode 1 of eigen buckling analysis for interactive buckling specimens.....	68
Fig. 57: Mode 2 of eigen buckling analysis for interactive buckling specimens.....	68
Fig. 58: Interactive buckling mode in one of the column specimens: a. Global buckling (left) b. Local buckling (right)	69
Fig. 59: Axial load vs. axial deformation for W14×14×4 built-up columns of grade 120 ksi	70
Fig. 60: Ultimate load vs member slenderness for W14×14×4 column	71
Fig. 61: Comparison of P_u (FE analysis) and P_n (AISC) for 120 ksi built-up columns.....	72
Fig. A 1:Ban et al. (2013) residual stress model.....	81
Fig. A 2:Cao et al. (2020) residual stress model.....	83
Fig. A 3: Sun et al. (2019) residual stress model.....	85
Fig. A 4: Galambos et al. (1959) residual stress model	87
Fig. B 1: Flatness defects in hot-rolled steel: bow shaped defects and waviness defects (Sunthorn and Kittiphath, 2014)	101
Fig. B 2: Camber and sweep in wide flange sections	102
Fig. D 1:Steps for creating ABAQUS macro.....	105
Fig. D 2: Schematic diagram showing part of I-section	106

Fig. F 1: Axial load vs. axial deformation for W6×6 built-up stub columns of grade 100 ksi...	124
Fig. F 2: Axial load vs. axial deformation for W12×12 built-up stub columns of grade 100 ksi	124
Fig. F 3: Axial load vs. axial deformation for W10×16 built-up stub columns of grade 100 ksi	125
Fig. F 4: Axial load vs. axial deformation for W6×6 built-up stub columns of grade 140 ksi...	125
Fig. F 5: Axial load vs. axial deformation for W12×12 built-up stub columns of grade 140 ksi	126
Fig. F 6: Axial load vs. axial deformation for W10×16 built-up stub columns of grade 140 ksi	126
Fig. F 7: Normalized axial load vs. axial deformation for W10×11 hot-rolled stub columns of grade 100 ksi.....	127
Fig. F 8: Normalized axial load vs. axial deformation for W12×12 hot-rolled stub columns of grade 100 ksi.....	127
Fig. F 9: Normalized axial load vs. axial deformation for W14×14 hot-rolled stub columns of grade 100 ksi.....	128
Fig. F 10: Normalized axial load vs. axial deformation for W10×11 hot-rolled stub columns of grade 120 ksi.....	128
Fig. F 11: Normalized axial load vs. axial deformation for W12×12 hot-rolled stub columns of grade 120 ksi.....	129
Fig. F 12: Normalized axial load vs. axial deformation for W14×14 hot-rolled stub columns of grade 120 ksi.....	129

LIST OF TABLES

Table 1: Different kinds of HS3 Grades - (Ban and Shi 2018).....	3
Table 2: Dimensions of the developed FE model.....	19
Table 3: Residual stress in the FE model.....	23
Table 4: Applied residual stress in the FE model.....	26
Table 5: Ultimate load and local buckling load comparison.....	33
Table 6: List of specimens for study of local buckling of wide flange built-up stub columns.....	36
Table 7: Applied residual stresses in built-up specimen.....	37
Table 8: Comparison of AISC compressive strength with ultimate load and local buckling load for 100 ksi built-up columns.....	45
Table 9: Comparison of AISC compressive strength with ultimate load and local buckling load for 140 ksi built-up columns.....	46
Table 10: List of specimens for study of local buckling of wide flange hot-rolled stub columns	52
Table 11: Applied residual stresses in hot-rolled specimen.....	53
Table 12: Comparison of AISC compressive strength with ultimate load and local buckling load for 100 ksi hot-rolled columns.....	61
Table 13: Comparison of AISC compressive strength with ultimate load and local buckling load for 120 ksi hot-rolled columns.....	62
Table 14: List of specimens for study of interactive buckling of wide flange built-up columns .	67
Table 15: Comparison of AISC compressive strength with ultimate load for 120 ksi built-up columns.....	72

Table A 1: Applied residual stresses in built-up specimen.....	88
Table A 2: Applied residual stresses in hot-rolled specimen.....	93
Table B 1: Permitted variations from flat surface for plates (ASTM, 2019).....	99
Table B 2: Permitted variation in waviness (ASTM, 2019)	100
Table B 3: Permitted variations from length for wide flange sections (ASTM, 2019)	101

NOTATIONS AND SYMBOLS

The notations and symbols used in this thesis are described below in alphabetical order.

A_e	—	Effective area of the cross-section
A_g	—	Gross area of the cross-section
B	—	Width of the flange
b	—	Half-width of the flange excluding the thickness of the web
b_e	—	Reduced effective width
b_f	—	Half-width of the flange in the residual stress model
CMS	—	Conventional mild steel (Grades of structural steel less than 65 ksi)
COV	—	Coefficient of variance
C_w	—	Warping torsional constant
d	—	Depth of the web in the residual stress model
d_e	—	Reduced effective depth
E	—	Modulus of elasticity of steel
F_{cr}	—	Critical stress
F_{crx}	—	Critical stress in the minor axis
F_{cry}	—	Critical stress in the major axis
F_{elf}	—	Elastic local buckling stress in flange

F_{elw}	—	Elastic local buckling stress in web
F_{ex}	—	Flexural torsional elastic buckling stress in the minor axis
F_{ey}	—	Flexural torsional elastic buckling stress in the major axis
F_y	—	Yield strength of the material
f_{fc}	—	Compressive residual stress in the flange (Sun et al., 2019)
f_{ft}	—	Tensile residual stress in the flange (Sun et al., 2019)
f_{wc}	—	Compressive residual stress in the web (Sun et al., 2019)
f_{wt}	—	Tensile residual stress in the web (Sun et al., 2019)
G	—	Modulus of rigidity
H	—	Depth of the W shape
HS3	—	High strength structural steel
h_0	—	Depth of the web
h_w	—	Depth of the web in the residual stress model
I_x	—	Area moment of inertia along the minor axis
I_y	—	Area moment of inertia along the major axis
J	—	St. Venant Torsional Constant
L	—	Length of the column
L_c	—	Effective length of the column

t_e	—	Thickness of the weld
t_f	—	Thickness of the flange
t_w	—	Thickness of the web
P_u	—	Ultimate load capacity of the column
P_L	—	Local buckling load of the column
P_n	—	Nominal strength of the column
P_y	—	Yield load of the column
r_x	—	Radius of gyration along minor axis
r_y	—	Radius of gyration along major axis
Y/T	—	Yield strength to tensile strength ratio
ε	—	Engineering strain
Δ	—	Lateral displacement
λ	—	Member slenderness
λ_f	—	Flange slenderness
λ_w	—	Web slenderness
λ_l	—	Limiting effective slenderness ratio
λ_r	—	Limiting width-to-thickness ratio
λ_{rf}	—	Limiting width-to-thickness ratio of the flange

λ_{rw}	—	Limiting width-to-thickness ratio of the web
σ_c	—	Compressive residual stress (Galambos and Ketter, 1959)
σ_t	—	Tensile residual stress (Galambos and Ketter, 1959)
σ_{fc}	—	Compressive residual stress in the flange (Ban et al., 2013)
σ_{fte}	—	Tensile residual stress at flange end (Ban et al., 2013)
σ_{ft}	—	Tensile residual stress at flange center (Ban et al., 2013)
σ_{wrc}	—	Compressive residual stress in the web (Ban et al., 2013)
σ_{fc}	—	Compressive residual stress in the flange (Cao et al., 2020)
σ_{ft}	—	Tensile residual stress at flange center (Cao et al., 2020)
σ_{fte}	—	Tensile residual stress at flange end (Cao et al., 2020)
σ_{wc}	—	Compressive residual stress in the web (Cao et al., 2020)
σ_{wt}	—	Compressive residual stress in the web (Cao et al., 2020)

Blank Page

1.0 INTRODUCTION

High Strength Structural Steel (HS3) is defined as steel with a yield strength (F_y) greater than 65 ksi (450 MPa). It also possesses adequate ductility for performance-based design or conventional plastic design and must exhibit sufficient toughness and weldability to be used as a structural building member (Ban et al., 2018).

There are many grades of HS3 steel available in the markets that are used for construction purposes. The steel properties, national standards, and national codes are periodically improved to include the most optimal properties and the latest advances in the research. China and Europe have developed national standards for all HS3 steel grades available in their market and their national codes support the use of HS3 steel. There exist many other HS3 grades that are not currently mentioned in the design codes. Further research is needed to determine their performance prior to incorporation in these codes. Table 1 lists various kinds of HS3 grades available in the market around the globe along with their applicable national standards.

HS3 steel has significantly higher yield strength when compared with conventional mild steel (CMS). CMS are steels commonly used in building applications with yield strengths less than 65 ksi, such as ASTM A36 and ASTM A992 steels. It is unreasonable to apply conventional design methods to HS3 structures without analysis and investigation because these advanced steels exhibit different material properties compared with CMS. HS3 steel has no defined yield plateau which makes it to be quite different from that of the CMS. Fig. 1 shows the comparison of the engineering stress-strain relationship of HS3 and CMS steel. HS3 steel has a higher yield to tensile strength ratio including higher resistance to loading without increasing the amount of steel (Shi et al., 2014). There are various methods of manufacturing HS3 steel, the two most important methods of

achieving HS3 are quenching and tempering, and Thermo-mechanical control process. Heating Quenched and Tempered steel beyond the tempering temperature can reduce the yield strength of such material. Hence, post-weld heat treatment temperature should be carefully selected.

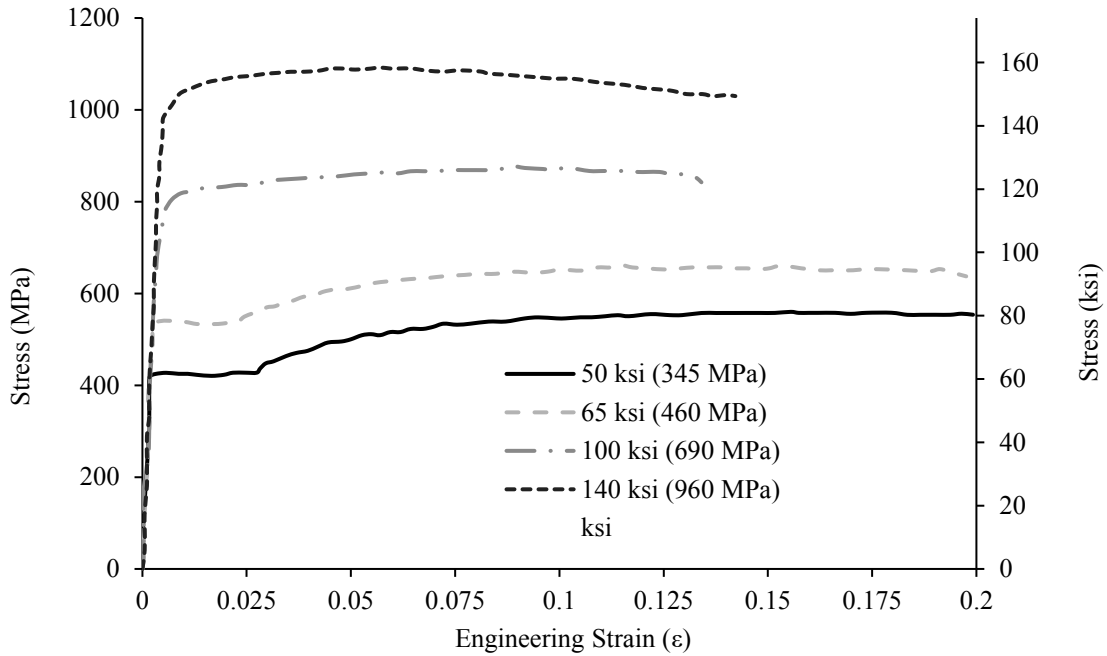


Fig. 1: Comparison of Stress-Strain curves of HS3 vs CMS steel - (Ban et al., 2018)

HS3 steel exhibits the following properties beyond its yield point relative to CMS: (Ban et al., 2012)

1. Lower ductility (but acceptable for plastic or performance-based design)
2. Higher yield-to-tensile strength (Y/T) ratios
3. Higher impact energy
4. Higher toughness
5. Lower ratios between residual compressive stresses and yield strengths of the steel

The efficient use of HS3 steel can optimize the utilization of steel which may, in turn, lead to reduced construction costs and a reduced carbon footprint.

Table 1: Different types of HS3 Grades - (Ban et al., 2018)

HS3 Grade	Yield Strength (F _y)	National Standard	National Code
A514/A514M	100 ksi (690 MPa)	ASTM A514/A514M-14	AISC 360 (2016)
HPS 70W	70 ksi (485 MPa)	ASTM A709/A709M-16	AISC 360 (2016), AASHTO (2017)
HPS 100W	100 ksi (690 MPa)	ASTM A709/A709M-16	AISC 360 (2016), AASHTO (2017)
HPS 70	70 ksi (485 MPa)	ASTM A913/A913M-15	AISC 360 (2016), AASHTO (2017)
TMCP 130	130 ksi (890 MPa)	ASTM A514/A514M-13	AASHTO (2017)
S500	72.5 ksi (500 MPa)	EN 10025-6: 2004	Eurocode 3 (2007)
S550	80 ksi (550 MPa)	EN 10025-6: 2004	Eurocode 3 (2007)
S620	90 ksi (620 MPa)	EN 10025-6: 2004	Eurocode 3 (2007)
S690	100 ksi (690 MPa)	EN 10025-6: 2004	Eurocode 3 (2007)
S890	130 ksi (890 MPa)	EN 10025-6: 2004	Eurocode 3 (2007)
S960	140 ksi (960 MPa)	EN 10025-6: 2004	Eurocode 3 (2007)
Q500	72.5 ksi (500 MPa)	GB/T 1591-2008	Chinese code (2017)
Q550	80 ksi (550 MPa)	GB/T 1591-2008	Chinese code (2017)
Q620	90 ksi (620 MPa)	GB/T 1591-2008	Chinese code (2017)
Q690	100 ksi (690 MPa)	GB/T 1591-2008	Chinese code (2017)
Q620GJ	90 ksi (620 MPa)	GB/T 19879-2015	Chinese code (2017)
Q690GJ	100 ksi (690 MPa)	GB/T 19879-2015	Chinese code (2017)
SHY685	100 ksi (685 MPa)	JIS G 3128: 2009	AIJ 2005
SBHS700	100 ksi (700 MPa)	JIS G 3140: 2011	AIJ 2005

New design methods and modified design approaches were developed for HS3 steel in major national codebooks. However, there is still a need to optimize the allowance of load-carrying capacities and member ductility parameters when using HS3 members in most national codebooks (Ban et al., 2018). No new design provisions for HS3 members are provided in AISC 360 (2016) because more extensive research is required to include them. AASHTO (2017) provides design provisions for HS3 plate girders up to 100 ksi (690 MPa). A proposal was submitted to the review

board during the code cycle development for AISC (2016) to increase the current limit of 65 ksi (450 MPa) on the yield strength to 70 ksi. This proposal was in cases where plastic hinging is anticipated, and rotation capacity is required to redistribute the moments (Fahnestock et al., 2019). In support of this proposal, several test data for small-scale bend tests were submitted as evidence for the material ductility of 70 ksi HS3 members. Evidence of large-scale member-level ductility involving rotation capacity was not enough to justify the increase in the yield strength (F_y) (Fahnestock et al., 2019). Eurocode (2007) has some new design rules for HS3 members for grades up to 100 ksi. But they were developed on extending the research done on CMS members to include HS3 members. Such design rules may be questionable due to extremely limited analytical and experimental data proving the research (Ban et al., 2012). Chinese code (2017) provides some design provisions for HS3 columns but, these are limited to grades up to 67 ksi (460 MPa).

The issues of buckling in the columns can be classified into three types namely-

1. Global Buckling.
2. Local Buckling.
3. Interactive Buckling.

In columns with high width-to-thickness ratios and low member slenderness, the mode of failure is usually due to the crippling of flanges and webs at a particular location due to the high axial load. Sometimes, this mode of failure may occur at two or more points usually at the center and at one-fourth location of its length. This buckling mode which is observed because of the crippling of flanges and web is called local buckling. This phenomenon is a little different in columns than with beams because of the difference in stress state. Fig. 2 (Shi et al., 2015) shows the flanges and the web of a test column buckling together.



Fig. 2: Local Buckling mode observed in one of the test specimens. (Shi et al., 2015)

In columns with high width-to-thickness ratios and intermediate member slenderness (global slenderness between 40 to 80), local buckling is observed, (Cao et al., 2021) but the mode of failure is still flexural buckling. In such columns, the local buckling will instigate the process of flexural buckling. This mode of buckling is called interactive buckling or local-overall buckling. This mode of buckling will usually occur at a particular location, which is usually at the center of the column. Fig. 3 shows the mode of failure of a column undergoing interactive buckling.

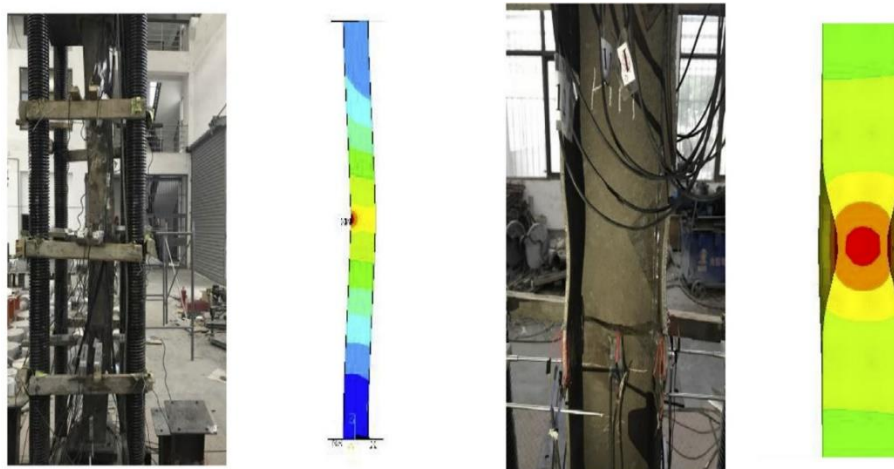


Fig. 3: Interactive mode observed in one of the test specimens - (Cao et al., 2021).

1.1 RESEARCH OBJECTIVE

A study was previously conducted by Akhtar and Chicchi (2021) to examine the behavior of HS3 wide flange columns under flexural buckling. That study found that the current AISC 360 (2016) design equations for flexural buckling can adequately predict flexural buckling capacity. This work will build upon that previous study to explore local buckling effects in HS3 stub columns through data obtained from numerical simulations and experimental studies. It also studies the applicability of the AISC 360 (2016) *Specification's* local buckling design equations for the HS3 column. Axially loaded wide flange built-up and hot-rolled gravity stub columns with yield strengths of 100 ksi, 120 ksi, and 140 ksi were studied to obtain their local buckling strengths. Stub columns were selected to be studied because of the ease in capturing the local buckling effects in the HS3 steel.

1.2 THESIS OVERVIEW

Chapter 2 presents a summary of relevant experimental and analytical studies pertaining to the study of local and interactive buckling in HS3 columns. Chapter 3 talks about the development and validation of the FE model with an explanation of the materials, partitions, boundary conditions, initial geometric imperfections, residual stresses, and displacement control method. Chapter 3.2.2 compares the experimental results with that of the ABAQUS results. Chapter 4 has a detailed explanation of the parametric study conducted for the study of local and interactive buckling of columns. Chapter 4 also discusses the results associated with the parametric study with great emphasis on graphical and tabular findings and discusses the probable cause for such findings. Chapter 5 presents a summary of the results obtained in the previous sections and presents the ideas for future research work. Appendices A through E have information related to the residual

stresses, initial geometrical imperfections, AISC slenderness limits, the usage of ABAQUS macros, and the calculation of nominal compressive strength.

2.0 LITERATURE REVIEW

2.1 EXPERIMENTAL STUDIES

Usami and Fukumoto (1982; 1984) studied HS3 stub columns fabricated from 65 ksi (460 MPa) to 100 ksi (690 MPa) grades and performed axial compression tests on built-up box section stub columns with relatively large width-to-thickness ratios. All the specimens tested were subjected to either concentric or eccentric axial loading through the axial compression test. A new formula for estimating the ultimate stress after the local buckling was proposed. This formula approach provided satisfactory predictions for columns with large width to thickness ratios but was not consistent with columns with smaller width-to-thickness ratios.

Rasmussen and Hancock (1992) studied the plate slenderness limits of the HS3 specimens by performing stub column tests on wide flange section, box section, and cruciform sections made by plates of HS3 BISALLOY of yield strength 100 ksi (690 MPa). Fig. 4 shows the typical cross-section details of stub columns used in the study. The stub column specimens prepared were sufficiently short to exclude the overall instability effects and were sufficiently long to allow unrestrained effects of local buckling. Separate stub column specimens were prepared to determine the residual stresses. The test strengths of the specimen were then compared to the plate strength curves of the AS4100, AISC LRFD, BS 5950 Part1, and Eurocode 3. It was found that the same yield slenderness limits apply to CMS and HS3 plates. Since the stocky plates were less affected by the residual stress than the slender plates, the HS3 plates had inferior strain hardening properties compared with the CMS plates. This means that the non-dimensional strength of stocky HS3 is less than that of stocky CMS plates.

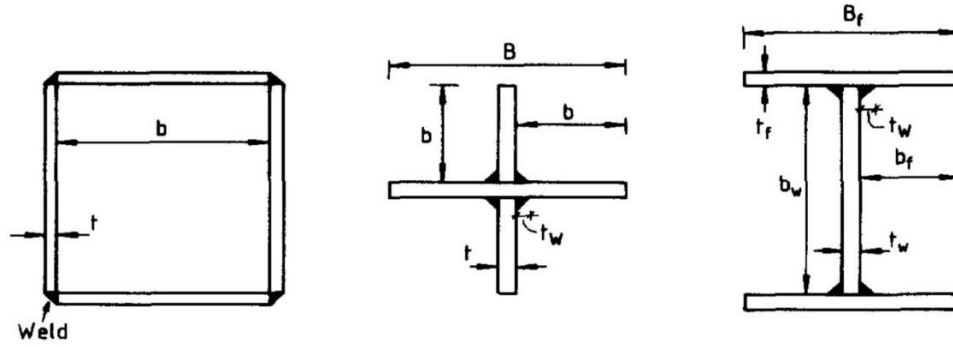


Fig. 4: Different types of HS3 column cross-section - (Rasmussen et al., 1992)

Shi et al. (2014) performed experimental studies on the local buckling behavior of both built-up box section and built-up wide flange section columns made of grade 67 ksi (460 MPa) HS3. The experimental results showed that the local buckling stress, the ultimate stress, and the stress ratio (the ratio of local buckling stress to ultimate stress) decreased with the increase in the width-to-thickness ratio of the plates. This indicated that the local buckling mode occurred before the steel yielded and helped to determine the ultimate strength of the specimen of high width-to-thickness ratios. The post-buckling strength of the specimen increased with the increase in the width-to-thickness ratio. Fig. 5 shows the typical test configuration for the axial compression test.

Shi et al. (2020) studied the local and interactive buckling behavior of CMS built-up wide flange section specimens of grades 34 ksi (235 MPa) and 50 ksi (345 MPa) subjected to axial compression tests. Axial compression tests were conducted on sixteen built-up wide flange section specimens that had varied width-to-thickness ratios. The failure mode of all specimens was found to be local-overall interactive buckling wherein local buckling was first observed in the flanges or the webs and then followed by the overall horizontal buckling. It was concluded that both AISC 360 (2016) and Eurocode 3 (2007) were reliable and consistent in predicting the load-carrying capacity of column specimens.

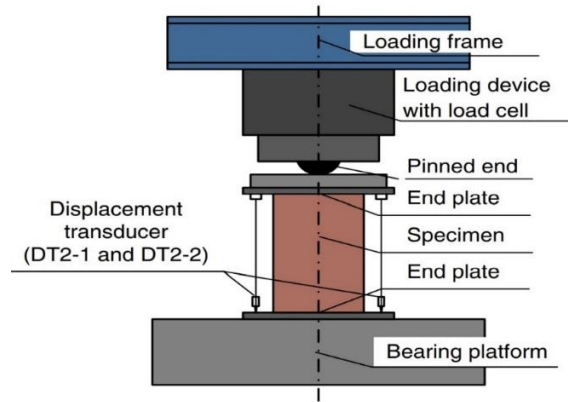


Fig. 5: Test configuration of Axial Compression Test - (Shi et al., 2014)

Yang et al. (2017) performed experimental tests on box sections fabricated from 34 ksi (235 MPa) and 50 ksi (345 MPa) steel subjected to axial compression. The results showed that Eurocode 3 (2007) and AISC 360 (2010) overestimated the ultimate load-bearing capacity (P_U) of box-section columns. The design methods in Eurocode 3 (2007) underestimated the interactive buckling resistance in box section columns and AISC 360 (2010) provided overestimated and scattered predictions for the same. A new design method was suggested for estimating the P_U of box section columns made of CMS and HS3 grades.

Cao et al. (2020) studied the local buckling behavior of 120 ksi (800 MPa) HS3 stub columns subjected to axial compression. New embedding coefficients based on the Chinese code (2017) were proposed. These coefficients included the effect of a flange on the web buckling and the effect of a web on the flange buckling. The experimental results showed that the design models in Chinese code (2017), Eurocode 3 (2007), and AISC 360 (2016) slightly overestimated the ultimate load-bearing capacity of built-up wide flange columns.

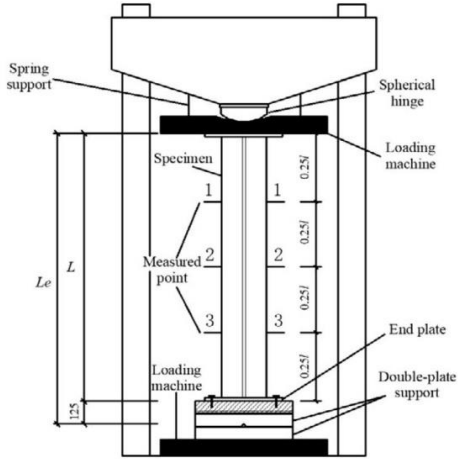
Cao et al. (2021) performed an experimental study on three different kinds of HS3 stub columns of grade 120 ksi (800 MPa). An investigation was done on columns with a low width-to-thickness

ratio of the plates, columns with a high height-to-thickness ratio of the web, and columns with a high width-to-thickness ratio of the flange. Height-to-thickness ratios of the web and width-to-thickness ratios of the flange were varied. It was found that the current specifications – (Eurocode 3 (2007) and AISC 360 (2016)) slightly underestimated the ultimate load of 120 ksi (800 MPa) HS3 built-up wide flange section members. Fig. 6 shows the experimental setup and a schematic diagram for the stub column test.

Su et al. (2021) performed comprehensive testing of HS3 stub columns of grade 140 ksi (960 MPa) to determine the membrane residual stresses and the local buckling behavior of the specimen columns. The comprehensive testing included material testing, local geometric imperfection measurements, membrane residual stress measurements, and sixteen stub column tests. A predictive model for obtaining the residual stress of 140 ksi HS3 stub columns was proposed which was later validated through the finite element (FE) analysis.



(a) Experimental setup



(b) Schematic diagram

Fig. 6: Experimental Setup for the study of Interactive Buckling - (Cao et al., 2021)

2.2 ANALYTICAL STUDIES

Beg and Hladnik (1996) performed a numerical analysis supplementing their experimental study in FINAS (FE analysis computer program) to investigate the influence of width-to-thickness ratio on the P_U of the wide flange sections (I-section). Based on the analytical results considering the interactions of the flange and web an expression for demarcation between slender and semi-compact wide flange sections was derived.

Shi et al. (2011) compiled experiments relating to HS3 stub columns subjected to axial compression and performed FE analysis to develop an analytical model to simulate the exact effects and results of experimental models. The proposed FE model was able to analyze the local buckling behavior of HS3 columns under axial compression after incorporating both the initial imperfections and the residual stresses. Fig. 7 displays three different sets of FE models studied by Shi et al. (2011).

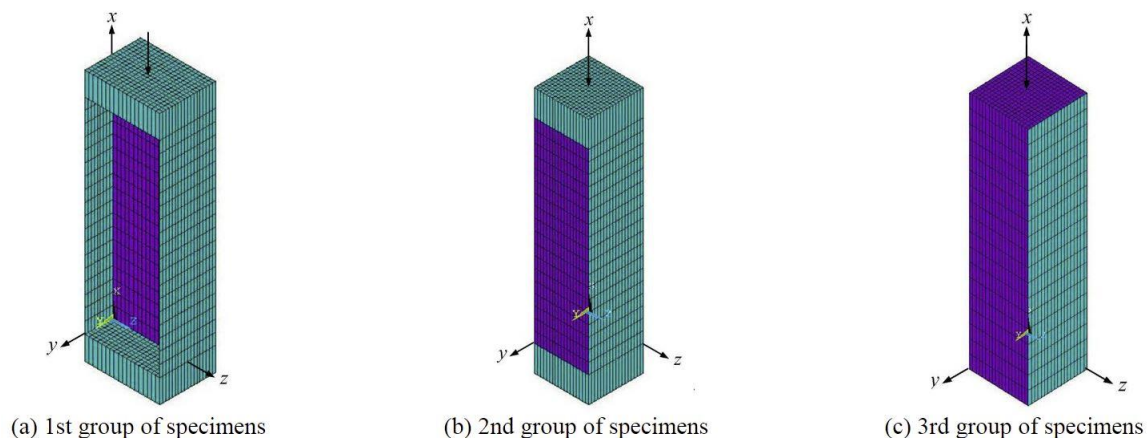


Fig. 7: Three different sets of Finite Element Models - (Shi et al., 2011)

Shi et al. (2014) performed stub column tests on four box sections and nine wide flange section specimens of 67 ksi (460 MPa) to validate the FE model established by the ANSYS software. A parametric analysis was performed based on the validated modeling approach to study the effect

of the width-to-thickness ratio on the local buckling behavior of stub columns. It was found that with the increase in the width-to-thickness ratio the ultimate stress at the location of local buckling decreased. This indicated that for wide flange section specimens, the flange and the web could be designed separately without considering the interaction between them. On comparing the results of the experiment and FE model with the estimates from different codes, it was found that for box specimens, the current design methods overpredicted the ultimate load but for the flange of wide flange section specimens, they appeared to be too conservative for cases of relatively high width-to-thickness ratio. The results showed that AISC 360 (2010) and Eurocode 3 (2007) predicted a more accurate ultimate load than the Chinese code (2017). Fig. 8 shows the comparison of ultimate flange stress to yield strength ratio and flange slenderness between the design methods and FE analysis results.

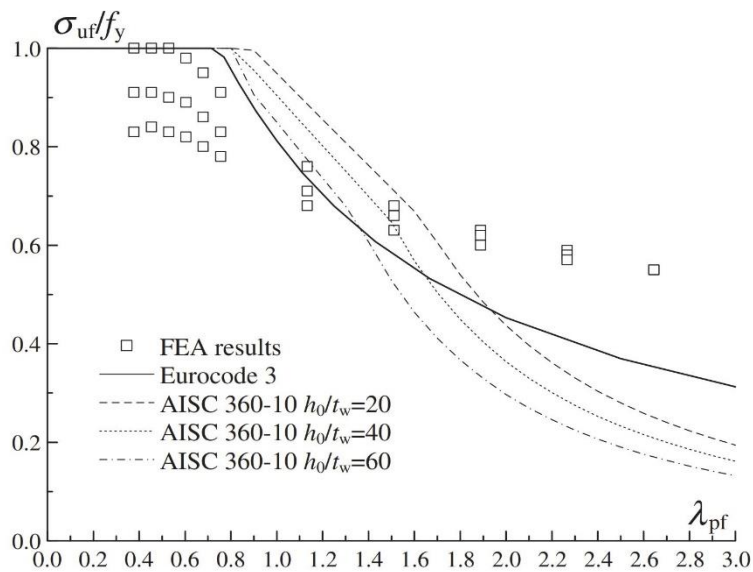


Fig. 8: Design methods on the ultimate stress of flange of the wide flange section - (Shi et al., 2014)

Shi et al. (2015) studied the local buckling behavior of 140 ksi (960 MPa) HS3 stub columns by performing experimental axial compression tests with both wide flange sections and box sections.

Validation of the experimental results was done with FE analysis in ANSYS. It was found that for the design of flange both AISC 360 (2010) and Eurocode 3 (2007) underpredicted the ultimate stress when the width-to-thickness ratio was comparatively smaller. With the increase of the width-to-thickness ratio, both design standards turned out to be conservative.

Shi et al. (2016) performed FE analysis to investigate the local buckling behavior of the built-up box section and built-up wide flange stub columns which were of HS3 and CMS grades. It was found that AISC 360 (2010), Eurocode 3 (2007), and Chinese code (2017) were inconsistent with the FE analysis results and the existing test results. New design formulas were proposed for estimating the post-buckling ultimate stress and the local buckling stress.

Javidan et al. (2016), Nassirnia et al. (2016), and Farahi et al. (2017) proposed an innovative process for enhancing the overall buckling behavior of the column. HS3 materials were applied at the corner interface between joints of CMS materials inside the hollow box column. Stub column tests were performed for specimens of grade 108 ksi (750 MPa) and 180 ksi (1250 MPa) to determine the compressive strengths of the specimen. FE analysis was performed by validating the results of the experiments with the FE models. It was found that the proposed HS3 tubes had twice and three times the load-bearing limit of ordinary hollow box section column for 108 ksi and 180 ksi steel tubes, respectively.

Schillo and Feldmann (2018); Schillo et al. (2018) performed axial compression tests from a series of built-up box-section columns with grades of 72.5 ksi (500 MPa) and 140 ksi (960 MPa) to investigate the interaction of local and global buckling. Thirteen stub column tests that were conducted were split into two group test series of 72.5 ksi and 140 ksi and the member slenderness for each was kept the same. Only the length of the member was varied along each group. The test results were used to construct a numerical model using FE analysis using ANSYS software for

further parametric studies. A new optimized resistance curve for estimating the ultimate load was suggested and an analytical approach denoted as “Generalized Slenderness Approach” was proposed to determine the slenderness of the specimen.

Sun et al. (2019) performed stub column tests on eight wide flange section stub columns of grade 100 ksi (690 MPa). The experimental results were validated with the FE analysis results through a comparison of the local buckling stresses, residual stresses, and the load-carrying capacities of the specimen columns. A predictive model was proposed for obtaining the membrane residual stresses in HS3 stub columns of grade 100 ksi. An investigation was done to determine the applicability of several specifications on the buckling behavior of built-up wide flange section stub columns. It was concluded that both AISC 360 (2016) and AS 4100 were accurate in predicting the ultimate strength of columns undergoing local buckling.

Cao et al. (2019) performed experimental tests consisting of eleven T-section stub columns to investigate the local buckling behavior of the built-up T-section columns of grade 120 ksi (800 MPa) HS3 steel. New coefficients based on Chinese code (2017) were proposed which included the effect of a flange on the web buckling and the effect of a web on the flange buckling. An FE analysis was performed to validate the experimental results and it was found that the FE model predicted the experimental results accurately. New width-to-thickness ratio limits for flange and web of the built-up T-section specimen of grade 120 ksi HS3 stub columns were suggested. A new model for estimating the ultimate load-bearing capacity (P_u) was proposed.

Cao et al. (2020) validated the experimental results obtained by a comprehensive study done on HS3 stub columns of grade 120 ksi (800 MPa) through a FE analysis. It was found that Eurocode 3 (2007), Chinese code (2017), and AISC 360 (2016) overestimated the ultimate load-bearing capacity of 800 MPa HS3 built-up wide flange section columns. A new model for estimating the

ultimate load-bearing capacity of 120 ksi HS3 columns was proposed by adjusting the stability factor in the Chinese code (2017) of the column through magnifying the slenderness of the column.

Shi et al. (2020) performed stub column tests on sixteen built-up wide flange section specimens of grade 34 ksi (235 MPa) and 50 ksi (345 MPa) to study the local and interactive behavior of stub columns. The experimental data was used to validate the FE models created in the ANSYS software. From the predictions of FE models on HS3 grades, it was found that AISC 360 (2016) overestimated the buckling strength of the columns while Eurocode 3 (2007) was slightly conservative. A design method based on the Chinese code (2017) was proposed which best fit the analyzed FE data better than the other two specifications.

Su et al. (2021) performed finite element analysis validating the results of the comprehensive study done by experimental analysis. A parametric study was done to determine the applicability of present code specifications for HS3 stub columns of grades ranging between 100 ksi (690 MPa) and 140 ksi (960 MPa) with the FE analysis results. It was found that the slenderness limits for plate elements in compression as discussed in Eurocode 3 (2007), AISC 360 (2016), and AS4100 can be used for classifying flanges and webs of 140 ksi HS3 built-up wide flange section columns. It was also found that all three code specifications had codified design provisions that yield accurate and consistent compression strengths predictions for 140 ksi HS3 built-up wide flange section stub columns.

Cao et al. (2021) performed stub column tests and validated the FE model to investigate the effects of width-to-thickness ratio, height-to-thickness ratio on the local buckling behavior of the specimen. Ninety-four different FE models were modeled to estimate the accurate ultimate load-carrying capacity of the specimen. A new model was proposed to calculate the ultimate load of a 120 ksi (800 MPa) HS3 built-up wide flange section column. Reliability analysis was performed

on the experimental and analytical data against the design methods of AISC 360 (2016), Eurocode 3 (2007), and the proposed model.

The above research works focus on the local buckling behavior of HS3 built-up stub columns. However, the investigation of the behavior of HS3 built-up wide flange section columns fabricated from grades above 100 ksi (690 MPa) is limited. Also, there are not many research works that compare the applicability of the design methods that use AISC 360 (2016) for predicting the local buckling strength of columns. The purpose of this study is to investigate the local buckling behavior of wide flange section HS3 columns of grades above 100 ksi (690 MPa) subjected to axial compression through FE analysis. This study also focuses to perform a parametric analysis on the influence of width-to-thickness ratio, section slenderness, and the length of a column on the local buckling behavior of HS3 columns of the grade above 690 MPa (100 ksi) and compare these parameters with the local buckling design method in AISC 360 (2016).

3.0 NUMERICAL MODEL

3.1 DEVELOPMENT OF FE MODEL

ABAQUS (SIMULIA, 2020), a finite element analysis software, was used to simulate the local and interactive buckling behavior of HS3 stub columns. The experimental results of Shi et al. (2015) for the 140 ksi stub column, Cao et al. (2020; 2021) for the 120 ksi stub column, and Sun et al. (2019) for the 100 ksi stub column were used to benchmark the numerical model. A total of five stub columns were modeled in ABAQUS, which are identified as I1 through I5. Columns I1 through I4 were used to simulate local buckling behavior in the FE model. Column I5 was used to simulate interactive buckling behavior in the FE model. The column was modeled using solid elements with dimensional properties consistent with the experimental specimens, as shown in Table 2 and Fig. 9. Appendix D has more information on modeling in ABAQUS using the ABAQUS macros.

3.1.1 PARTITIONS

Partitions in this context are small portions of an element in the ABAQUS model that would behave similar and could exhibit similar stresses before analysis. Partitions were necessary for modeling, as the residual stress varied along the cross-section of the wide flange (I-section). Each stub column was partitioned to enable proper residual stress distribution along the cross-section of the built-up wide flange section. Fig. 10 shows one of the modeled wide flange columns with various partitions. Welds in the wide flange section were modeled as a part of the wide flange section with the same properties as that of the wide flange section. This was done for ease of modeling and because welds did not fail during the experimental testing.

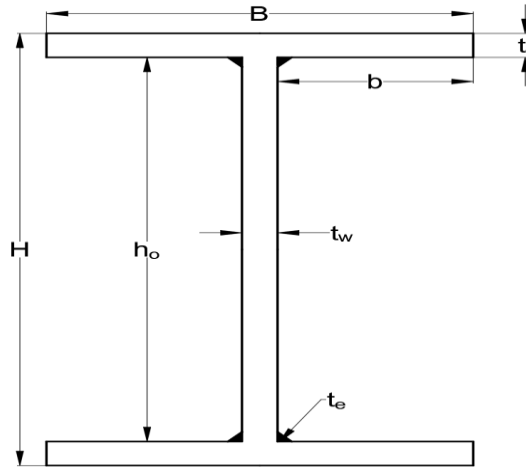


Fig. 9: Typical dimensional notations for the cross-sections modeled

Table 2: Dimensions of the developed FE model

Specimen ID	F_y (MPa)	L (in)	B (in)	H (in)	b (in)	h_o (in)	t_f (in)	t_w (in)	t_e (in)
11	960 (140ksi)	15.76	8.27	8.36	3.86	7.26	0.55	0.55	0.24
12	960 (140ksi)	19.69	10.51	10.47	4.98	9.37	0.55	0.55	0.24
13	800 (120ksi)	21.61	12.18	9.61	5.94	9.03	0.29	0.29	0.24
14	690 (100ksi)	16.44	3.91	7.85	1.86	7.46	0.20	0.20	0.24
15	800 (120ksi)	105.43	7.09	7.53	3.40	6.97	0.28	0.28	0.24

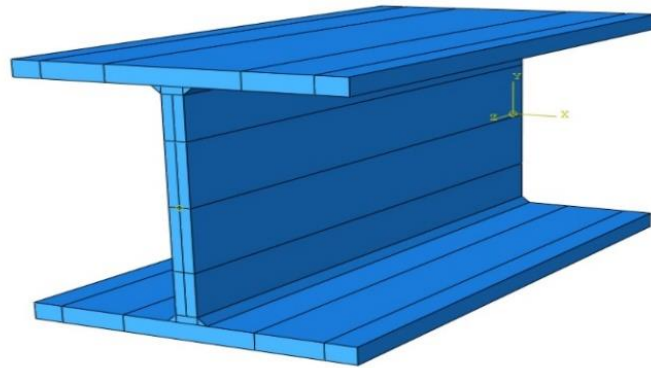


Fig. 10: A FE model of 140 ksi stub column model showing partitions

3.1.2 MATERIAL AND BOUNDARY CONDITIONS

The material for the stub column in ABAQUS was modeled as an isotropic material with both elastic and plastic properties. An isotropic material hardening was employed for material modeling based on the benchmarked studies. The wide flange stub column in the benchmarked studies was simply supported with a pinned end condition at one end and roller end condition at the other. The FE model was constrained as pinned on each face to a single point at the centroid of the cross-section with kinematic coupling constraint. Fig. 11 shows coupled kinematic constraints at the centroid of both ends of the wide flange section in the FE model. The FE model was meshed with a C3D8R (8 node linear brick with reduced integration and hourglass control) mesh element with a global seed size of 5mm. The global seed size was determined based on a mesh sensitivity analysis until a good match was obtained and this seed size was uniform throughout the model. Fig. 12 displays the meshed cross-sectional view and elevation view for the FE model.

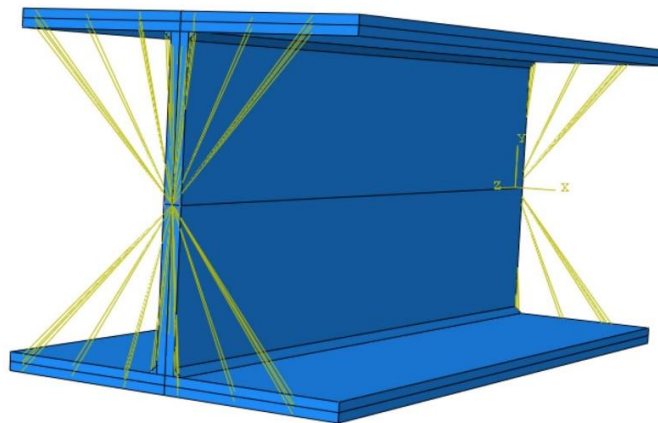


Fig. 11: Coupled kinematic constraints in the FE model

3.1.3 INITIAL GEOMETRIC IMPERFECTIONS

The initial geometric imperfection originating from out of straightness of the shape was applied in the FE model by updating the FE model geometry based on the relevant eigen buckling modes.

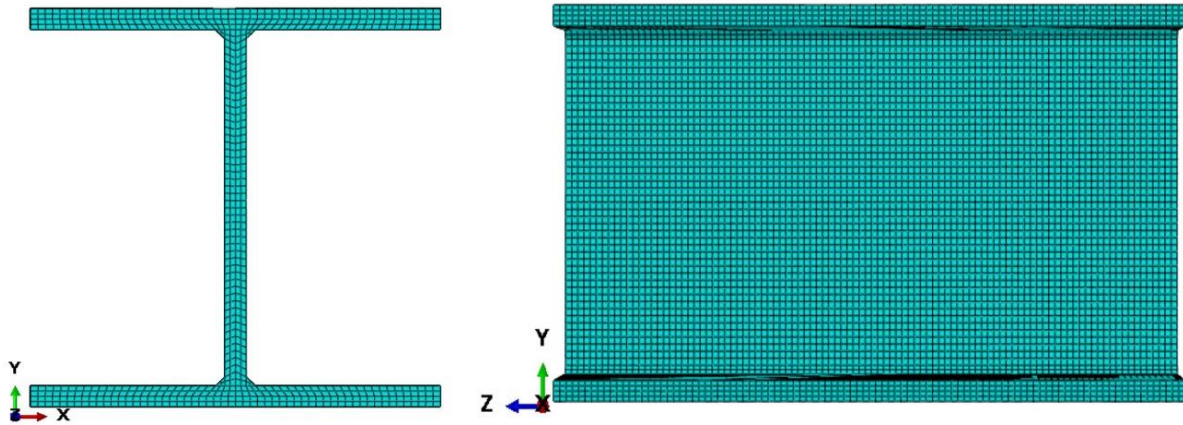


Fig. 12: Mesh cross-section (left) and elevation (right) of the FE model

This was done by first performing an eigenvalue buckling analysis on the FE model for fifty eigenmodes. Then, each eigenmode was evaluated for both web and flange buckling. Usually, the first eigenmode exhibited both web and flange buckling and was used to simulate the initial local imperfections of the cross-section. Global imperfections were not included for the FE models from I1 through I4 but were included for the I5 model. Fig. 13 shows the first eigenvalue buckling mode for the stub column FE model. Section 4.2 talks more about the deformed shape in the interactive buckling model. Fig. 52 shows the deformed shape in the interactive buckling model.

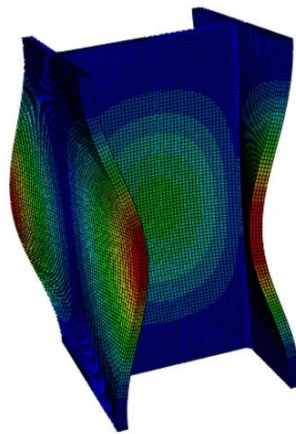


Fig. 13: First eigenmode for one of the FE models in 3D

3.1.4 RESIDUAL STRESSES AND DISPLACEMENT CONTROL METHOD

The residual stresses for the FE model were obtained using the following residual stress models from the experimental studies used to benchmark the experimental test: Ban et al. (2013) for 140 ksi (960 MPa) specimens, Cao et al. (2020) for 120 ksi (800 MPa) specimens and Sun et al. (2019) for 100 ksi (690 MPa) specimens. The residual stresses obtained from the models were applied to the cross-section of the FE model using the distribution shown in Table 3. This table shows the equations and the distribution of residual stresses in the developed FE model.

Displacement-control was used to simulate the axial compression loading effect in ABAQUS. Two steps were created in ABAQUS to model the displacement control method. The first step simulated the unloaded state of the stub column with both constraints pinned ($U1=U2=U3=0$ & $UR3=0$ for bottom constraint). In the second step, a displacement of 1.5 in. was applied to the top of the column. This created a roller end condition for the FE model. A step displacement of 1.5 in. was not enough to simulate the interactive buckling behavior in I5 model as its length was sufficiently longer than other models. Displacement of 10 in. was applied to I5 model. Fig. 14 shows the loading setup using the displacement method at the constraint point in one of the FE models.

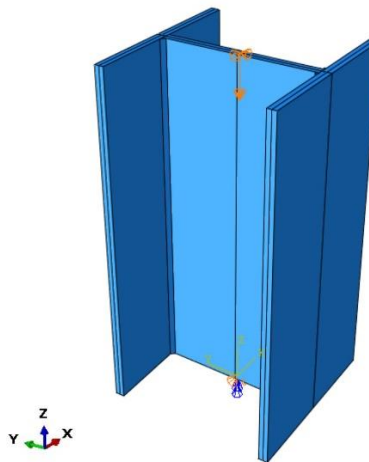


Fig. 14: Axial load setup using displacement control method.

Table 3: Residual stress in the FE model

Residual Stress Model	Equations (Units in MPa) ¹	Distribution
Ban et al. (2013) For 140 ksi material	$\sigma_{frc} = 100 - 930 \left(\frac{1}{\frac{b}{t_f}} \right) - 2205 \left(\frac{1}{t_f} \right)$ $(-960 \leq \sigma_{frc} \leq -96)$ $\sigma_{wrc} = 20 - 2200 \left(\frac{1}{\frac{h_o}{t_w}} \right) - 660 \left(\frac{1}{t_w} \right)$ $(-960 \leq \sigma_{wrc} \leq -96)$ $\sigma_{frt} = \sigma_{wrt} = 460 \text{ MPa}; \sigma_{frte} = 288 \text{ MPa}$	
Cao et al. (2020) For 120 ksi material	$\frac{b}{t_f} > 6$ $\sigma_{fc} = -670 + 33 \left(\frac{b}{t_f} \right) - 0.5 \left(\frac{b}{t_f} \right)^2$ $(-800 \leq \sigma_{fc} \leq -80)$ $\sigma_{wc} = -550 + 45 \left(\frac{h_o}{t_w} \right) - 1.36 \left(\frac{h_o}{t_w} \right)^2$ $(-800 \leq \sigma_{wc} \leq -80)$ $\sigma_{ft} = \sigma_{wt} = 380 \text{ MPa}$ $\sigma_{fte} = 135 \text{ MPa}$	
Sun et al. (2019) For 100 ksi material	$f_{ft} = 0.8F_y$ $f_{fc} = 0.8F_y$ $a = 0.225B$ $b = 0.15B$ $c = 0.075h_o$ $d = 0.225h_o$	

¹ 1 MPa = 0.145 ksi

3.2 VALIDATION OF FE MODEL

The experimental results of Shi et al. (2015) for the 140 ksi stub column, Cao et al. (2020; 2021) for the 120 ksi stub column, and Sun et al. (2019) for the 100 ksi stub column were used to validate the FE model. The local buckling load, which is the load that triggers the local buckling failure in columns, can be obtained by two methods from the experiment:

1. Top-of-the-knee method (Hu et al., 1946)
2. Maximum mid-surface strain method (Tillman et al., 1989)

The local buckling load according to the top-of-the-knee method is the load corresponding to the top of the knee of the curve of axial load against lateral deflection of the column as shown in Fig.19. If the lateral deflection cannot be measured, any other quantity that increases in substantially the same manner as that of lateral deformation is plotted against load to get the local buckling strength of the column. One such quantity can be differential strain along the axial direction which is consistent with the lateral deformation of the column. In this context, the axial deformation is taken to obtain the local buckling load as shown in Fig. 25. The local buckling load according to the maximum mid-surface strain method is the load corresponding to the maximum mid-surface strain value obtained by the curve of axial load against the mid-surface (center of the column) lateral strain of either the web or the flanges of the column. The maximum mid-surface strain method is most inconsistent, as it always assumes that the local buckling takes place at the center of the column, which is not the case in many columns. In this research, the top-of-the-knee method was used to determine the local buckling load of the FE model.

3.2.1 EFFECT OF RESIDUAL STRESSES AND IMPERFECTIONS

The applied residual stresses and the imperfections had great impact on the local buckling behavior of the CMS column (Shi et al., 2016). This impact was also noticeable in HS3 columns. It was

found that with the application of residual stresses and imperfections the ultimate load (P_u) decreased (by 10.5%) and was closer to the experimental result. Fig. 15 displays the comparison of the variation of axial load with axial displacement for the I1 FE model considering the impact of residual stresses and imperfections. Fig. 16 shows the distribution of residual stress in the I1FE model. Table 4 shows the applied residual stress along the cross-section of flange and web for all FE models. The residual stresses in Fig. 16 are in MPa.

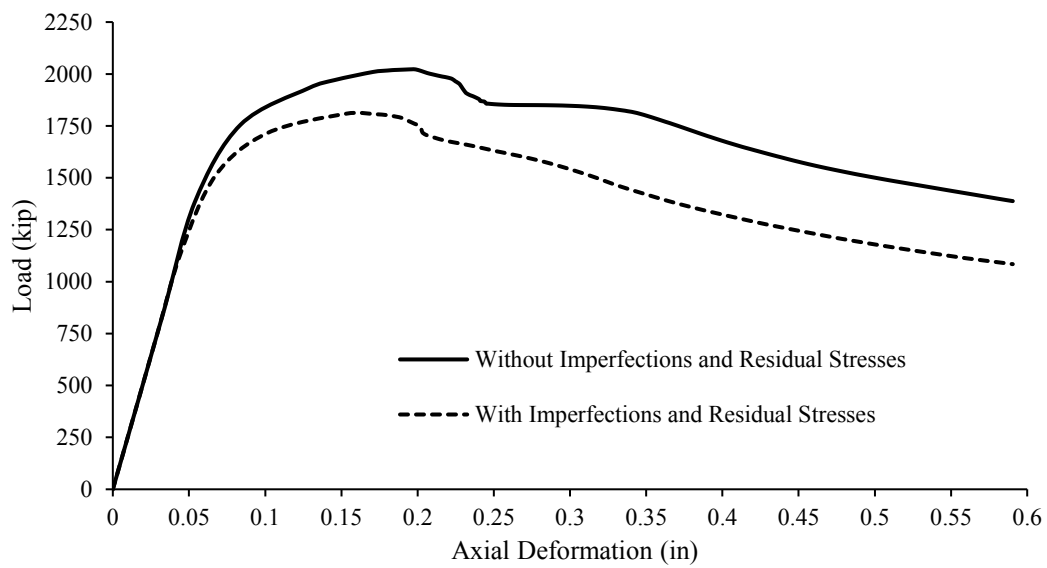


Fig. 15: Axial load vs. axial deformation for I1 specimen

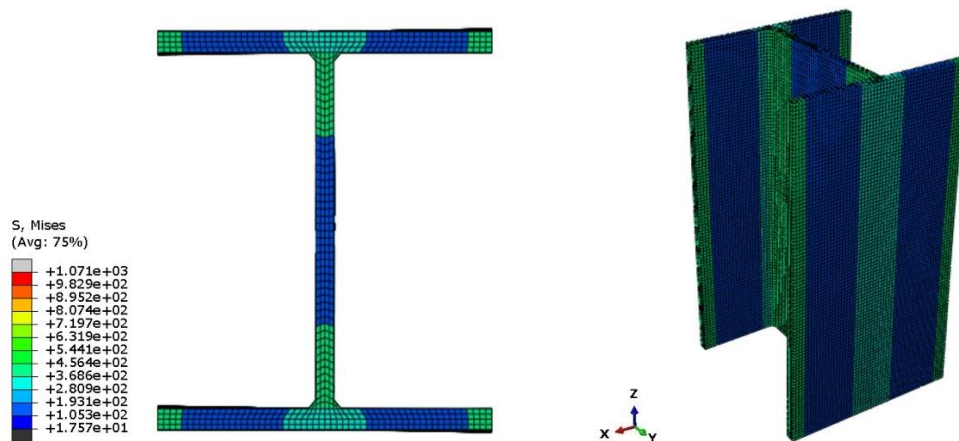
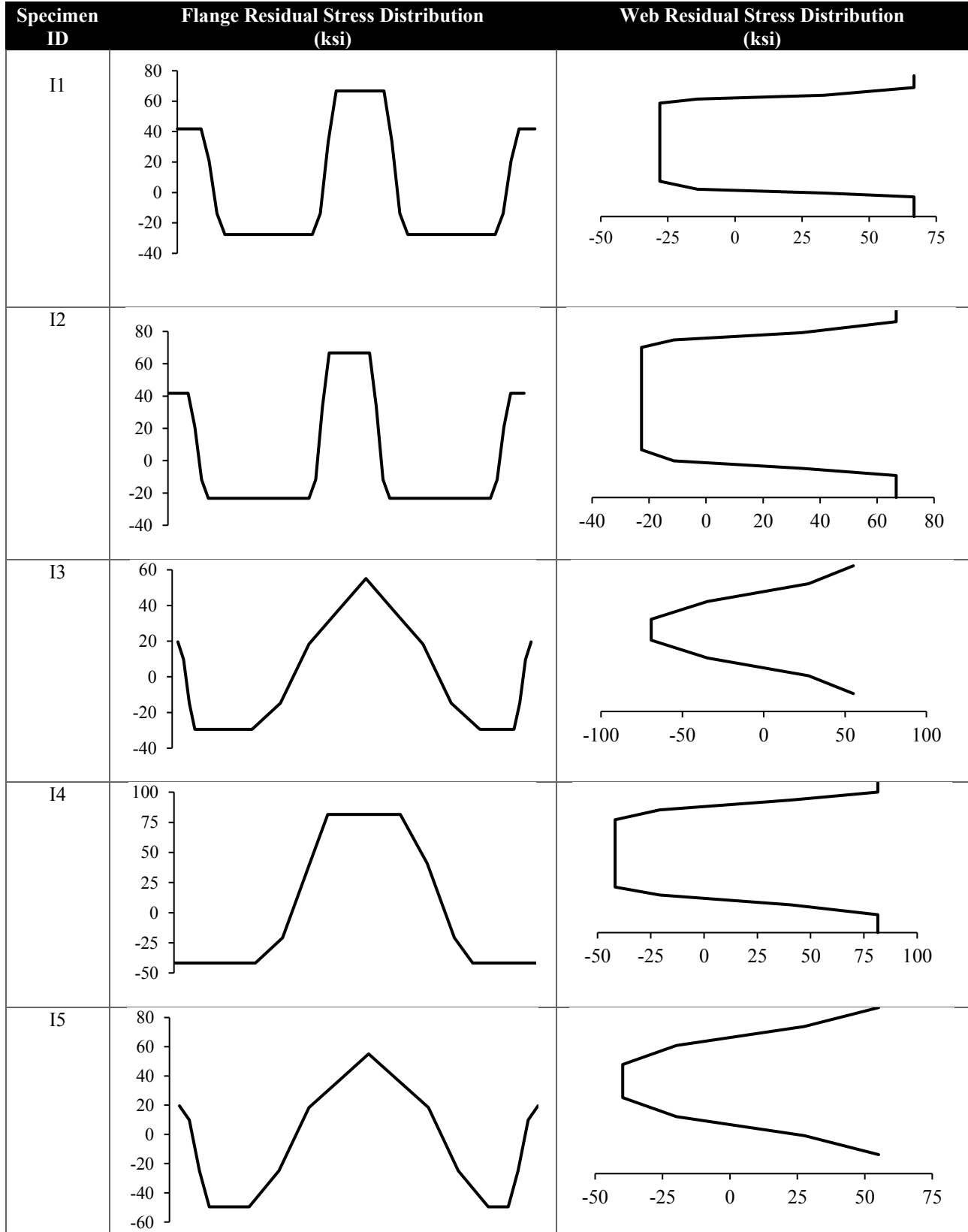


Fig. 16: Residual stress distribution in I2 FE model

Table 4: Applied residual stress in the FE model



3.2.2 COMPARISON OF ABAQUS RESULTS

The curves of axial load and lateral displacement and the curves of axial load and engineering strain in the lateral direction of the wide flange specimen were plotted at the mid-height of the specimens and were compared with that of the experimental studies. The obtained curves closely matched the experimental results with less than 10 percent deviation. Fig. 17 displays the comparison of the variation of axial load with engineering strain in the lateral direction for the I1 FE model in the flange. Fig. 18 shows the comparison of the variation of axial load with engineering strain in the lateral direction for the I1 FE model in the web.

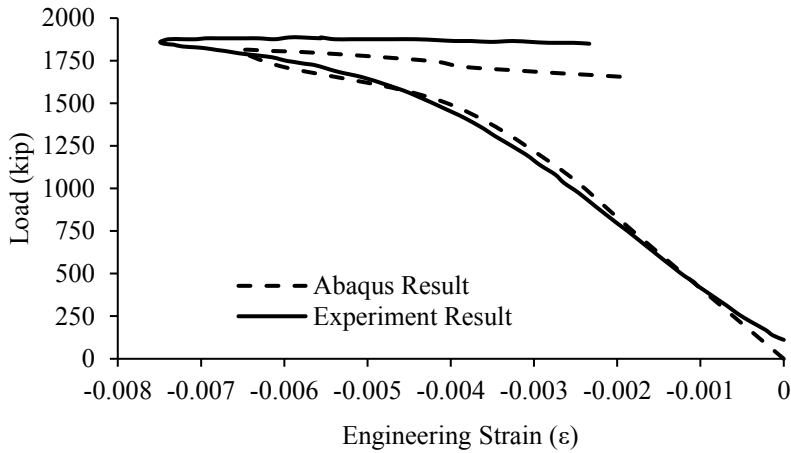


Fig. 17: Axial load vs strain in lateral direction of flange for I1 specimen

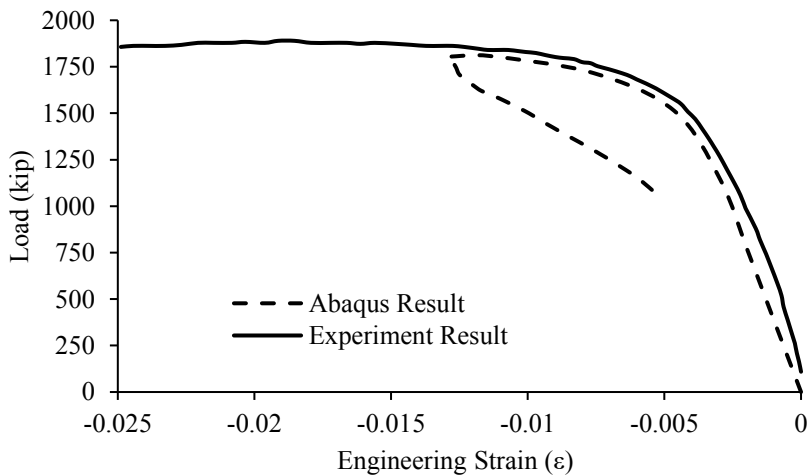


Fig. 18: Axial load vs strain in lateral direction of web for I1 specimen

Fig. 19 and Fig. 20 display the comparison of the variation of axial load with lateral displacement for the I1 FE model in the flange and the web. Fig. 21 and Fig. 22 show the comparison of the variation of axial load with strain for the I2 FE model in the flange and the web.

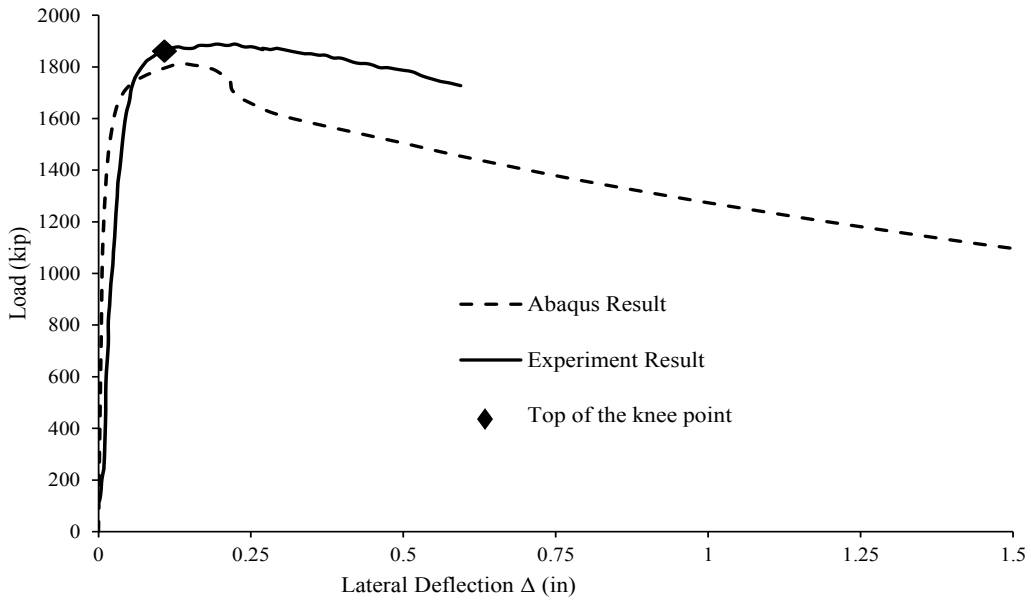


Fig. 19: Axial load vs. lateral deflection of flange for I1 specimen

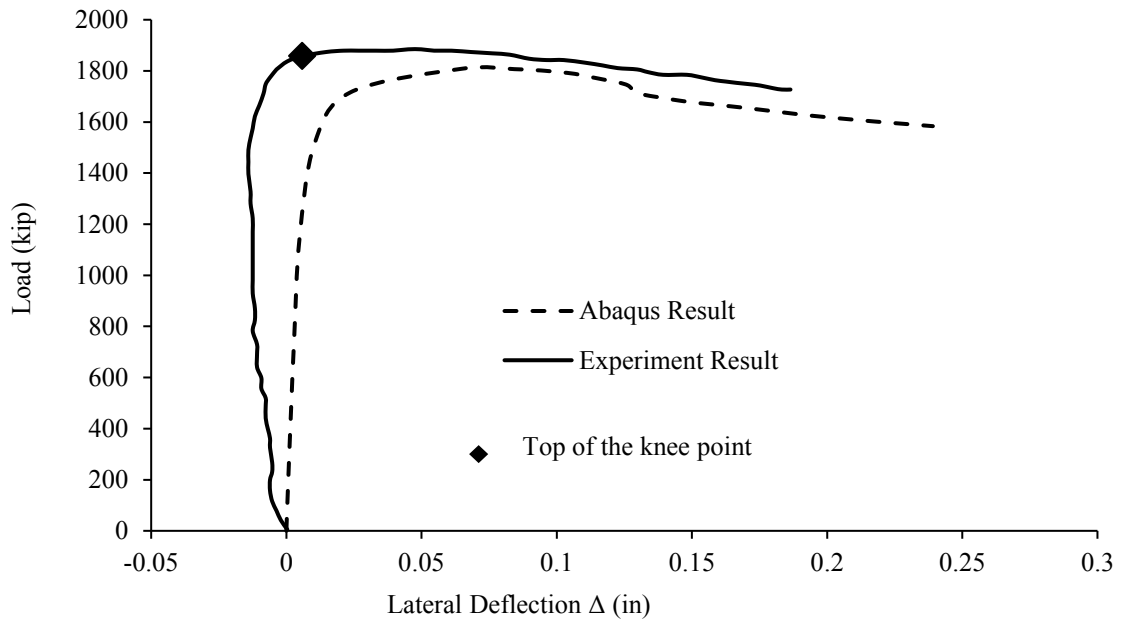


Fig. 20: Axial load vs. lateral deflection of web for I1 specimen

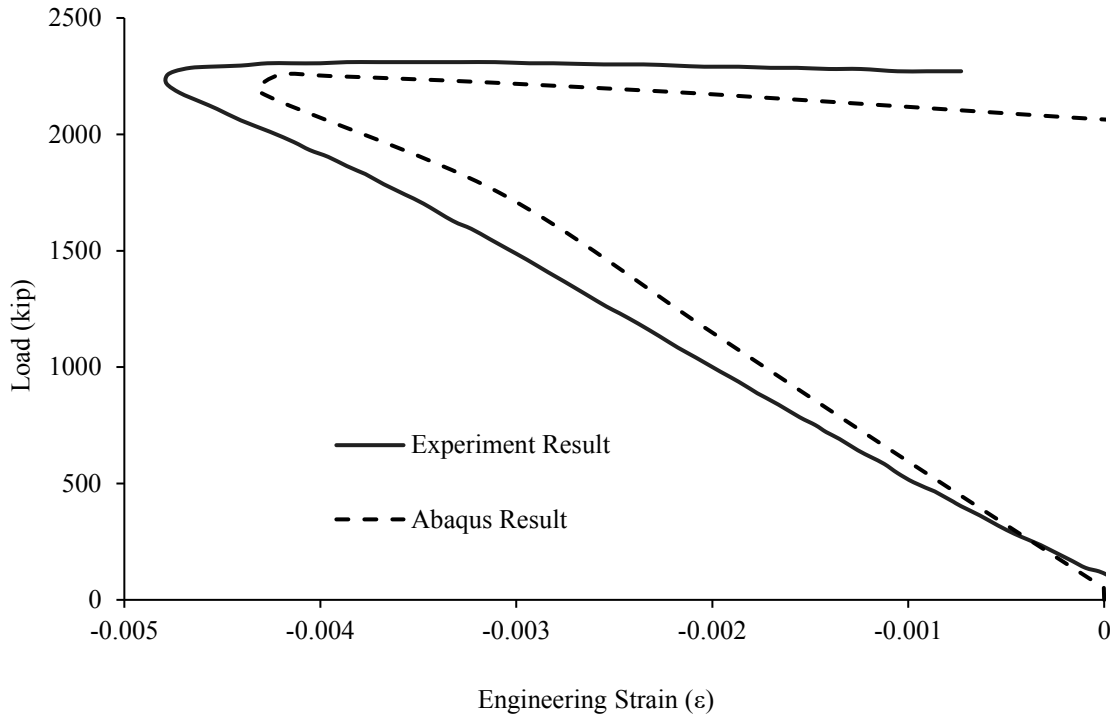


Fig. 21: Axial load vs. strain in the lateral direction of flange for I2 specimen

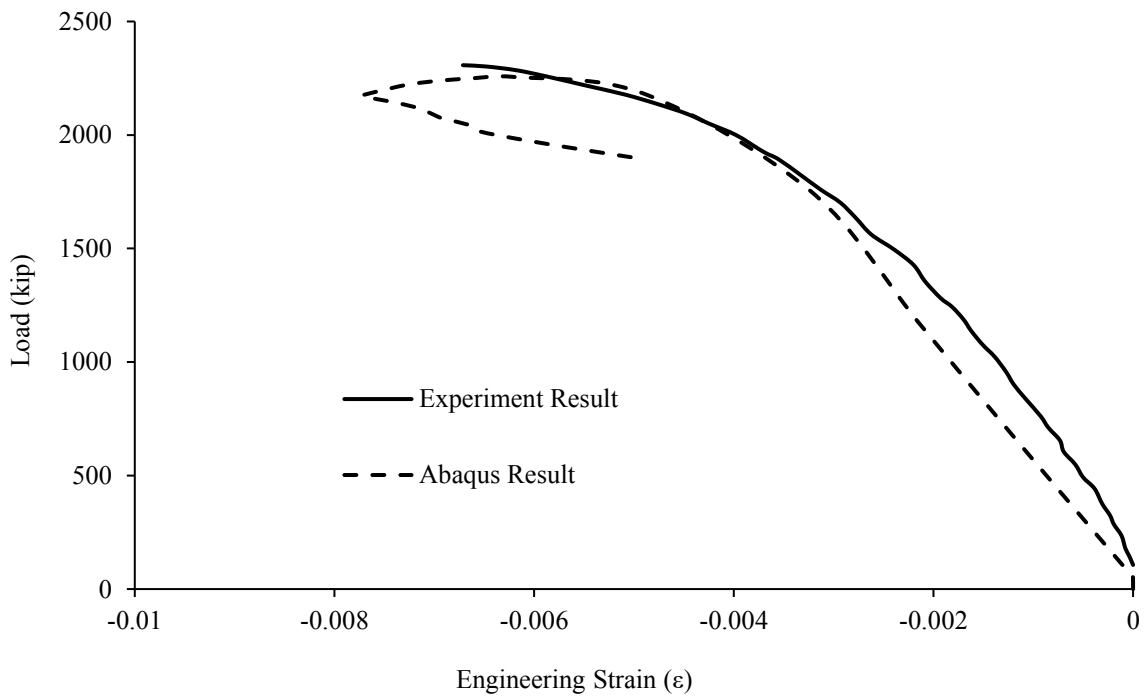


Fig. 22: Axial load vs. strain in the lateral direction of web for I2 specimen

Fig. 23 and Fig. 24 display the comparison of the variation of axial load with lateral displacement for the I2 FE model in the flange and the web. The obtained curves closely matched the experimental results with less than 10 percent deviation.

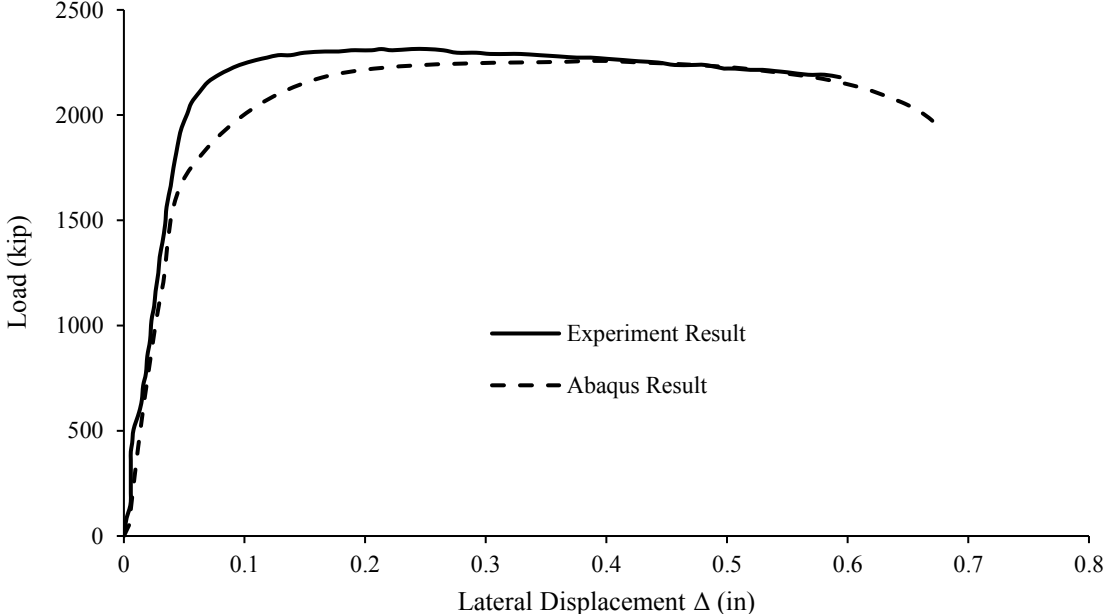


Fig. 23: Axial load vs. lateral deflection of flange for I2 specimen

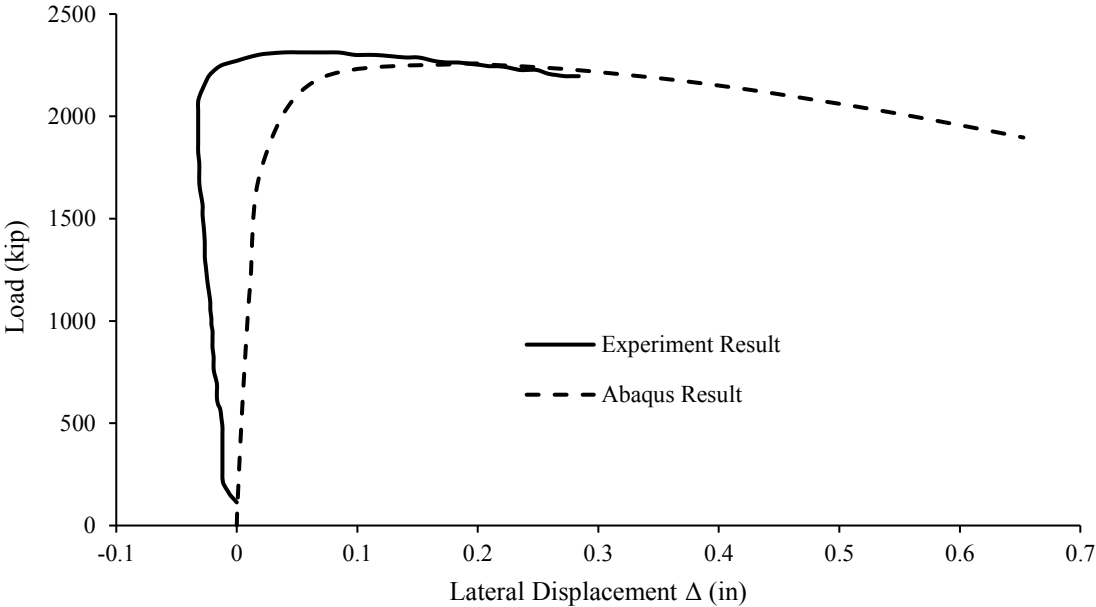


Fig. 24: Axial load vs. lateral deflection of web for I2 specimen

Fig. 25, Fig. 26, and Fig.27 display the comparison of the variation of axial load with axial deformation for I3, I4, and I5 FE models respectively. Table 5 gives a detailed comparison of the experimental ultimate load ($P_{u\text{ exp}}$) and experimental local buckling load ($P_{L\text{ exp}}$) with simulated ultimate load ($P_{u\text{ FE}}$) and simulated local buckling load ($P_{L\text{ FE}}$) from the FE model. Among the five tests, the mean value of the ultimate load ratio ($P_{u\text{ exp}}/P_{u\text{ FE}}$) was found to be 0.99 with a coefficient of variation (COV) of 7.36%, and the mean value of the local buckling load ratio ($P_{L\text{ exp}}/P_{L\text{ FE}}$) was found to be 1.00 with a COV of 7.74%. This shows that the FE model can predict the ultimate load and local buckling load of HS3 stub columns.

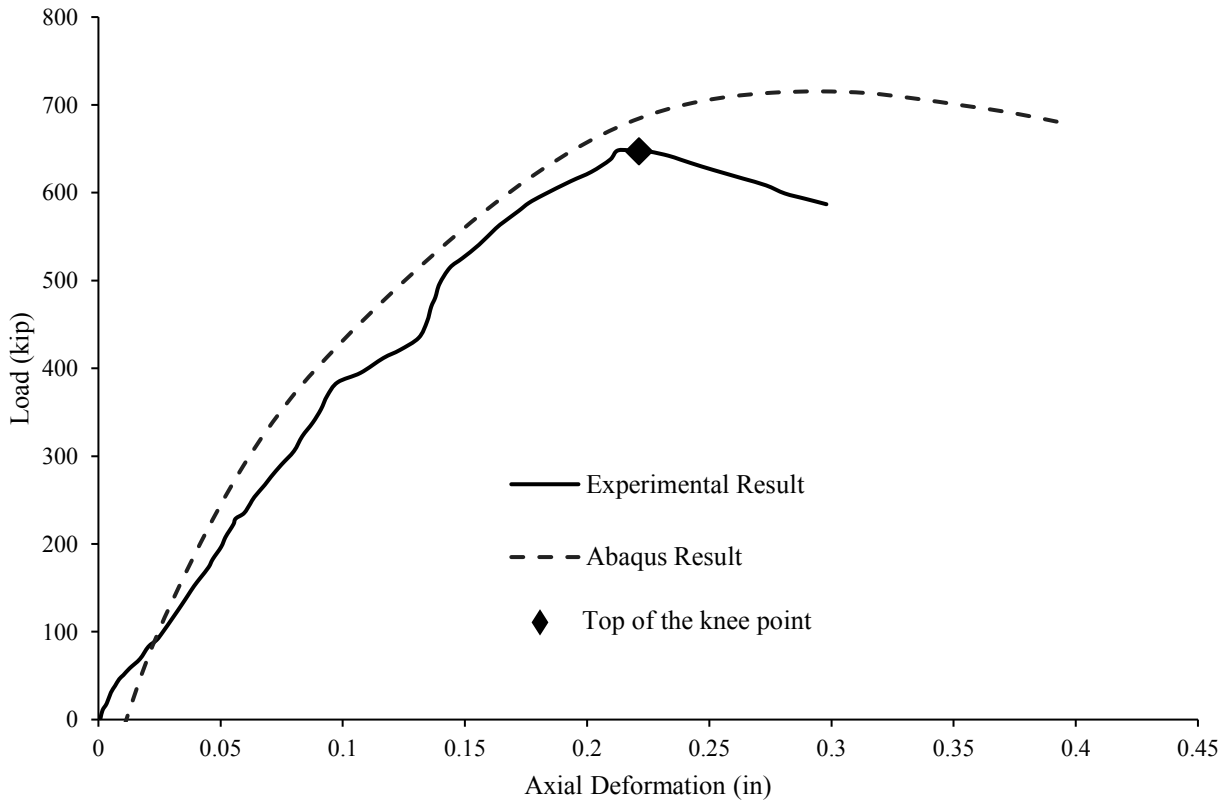


Fig. 25: Axial load vs axial deformation for I3 specimen

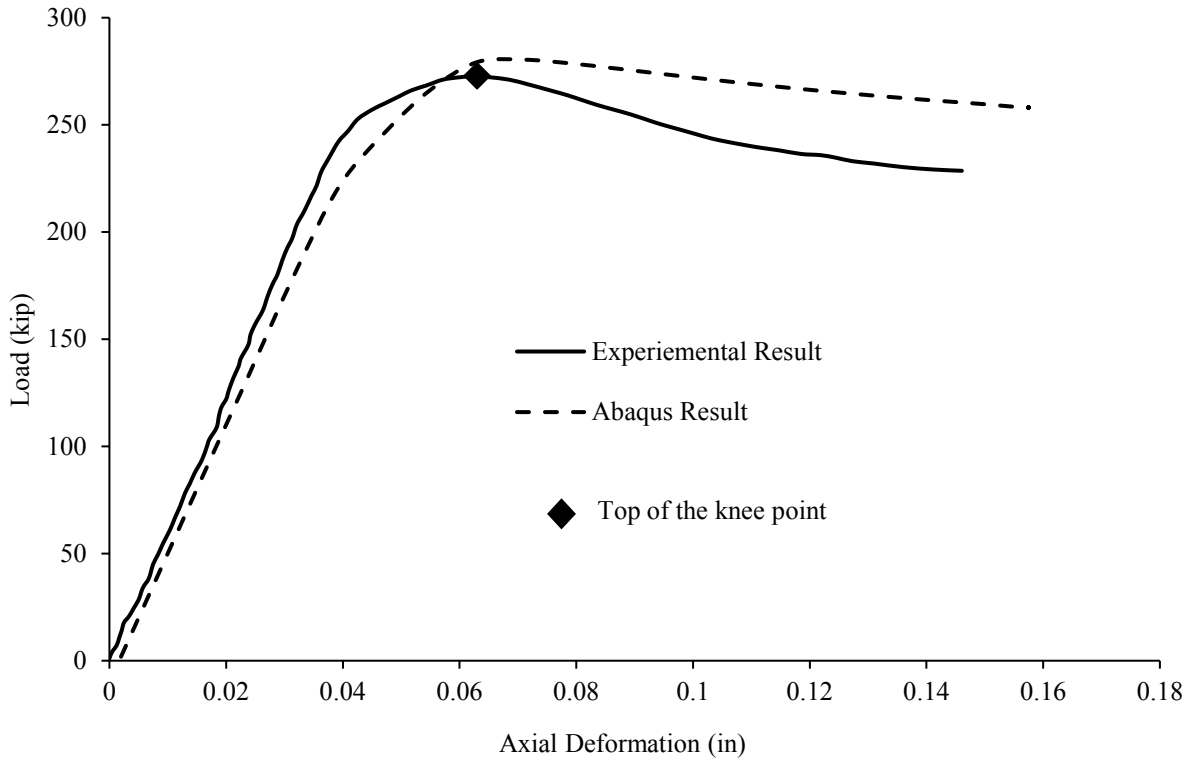


Fig. 26: Axial load vs. axial deformation for I4 specimen

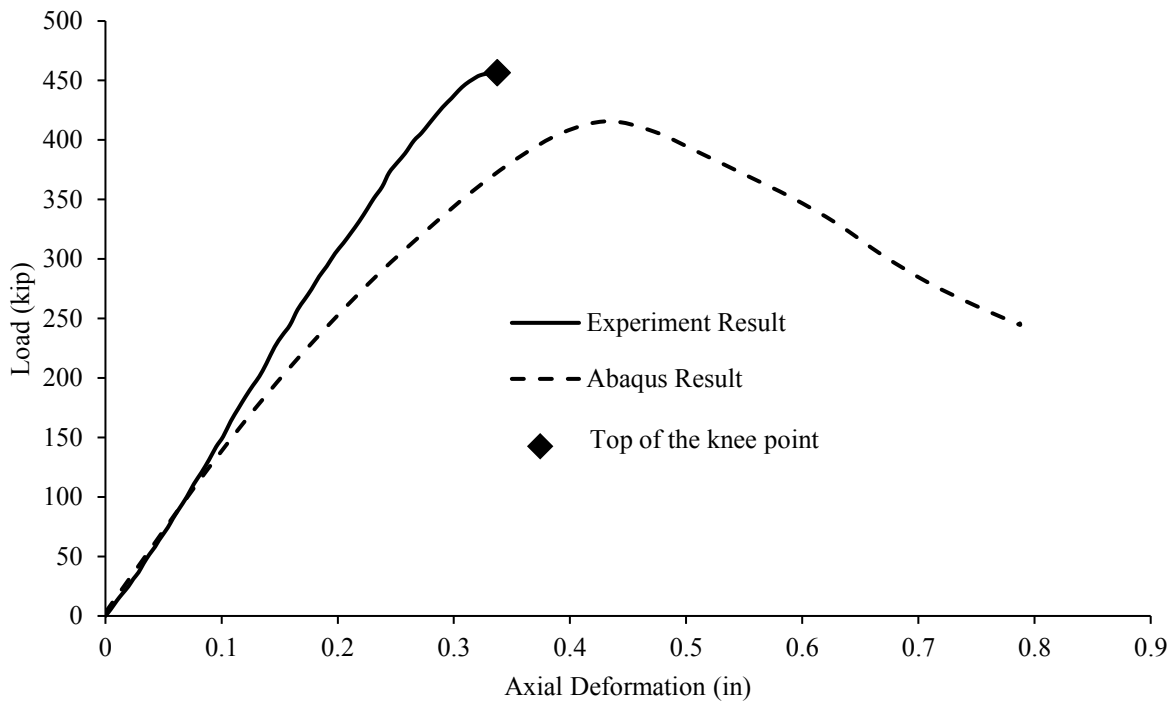


Fig. 27: Axial load vs. axial deformation for I5 specimen

Table 5: Ultimate load and local buckling load comparison

Specimen	F_y	$P_{u \text{ exp}}$	$P_{u \text{ FEM}}$	$P_{u \text{ FEM}} / P_{u \text{ exp}}$	$P_{L \text{ exp}}$	$P_{L \text{ FEM}}$	$P_{L \text{ FEM}} / P_{L \text{ exp}}$
ID	ksi	kip	kip		kip	kip	
I1	140 (960 MPa)	1886.02	1808.27	0.96	1886.02	1808.27	0.96
I2	140 (960 MPa)	2313.68	2262.15	0.98	2313.68	2255.90	0.98
I3	120 (800 MPa)	648.35	715.37	1.10	640.71	708.49	1.11
I4	100 (690 MPa)	272.94	280.41	1.03	266.10	279.37	1.05
I5	120 (800 MPa)	456.51	415.75	0.91	456.51	415.75	0.91
Mean				0.996			1.000
COV				7.364%			7.741%

4.0 PARAMETRIC STUDY OF HS3 COLUMNS

4.1 LOCAL BUCKLING OF BUILT-UP W SHAPES

4.1.1 PARAMETERS

Various parameters influence the compressive strength of wide flange columns. The most important parameters that affect the compressive strength are yield strength, section slenderness, member slenderness, and load eccentricity. Since the study of local buckling is important, the parameters of member slenderness and load eccentricity were kept constant, and local buckling effects were explored by varying section slenderness and yield strength. The residual stresses were different in hot-rolled and built-up sections. Because of this difference in residual stresses, a parametric study was conducted for both built-up and rolled members for three different wide flange sections of grade 100ksi (690 MPa), 120ksi (800 MPa), and 140ksi (960 MPa) across four different kinds of cross-sections for each column. Table 6 shows the list of specimens that were chosen for the study of local buckling in HS3 built-up stub columns, respectively. The modeling approach, material properties, boundary conditions, and initial geometrical imperfections were the same as those described in Chapter 3 for built-up W shapes.

Three initial column sizes: $W6 \times 6 \times 0.2 \times 0.2$, $W12 \times 12 \times 0.6 \times 0.6$, and $W10 \times 16 \times 0.3 \times 0.3$ were selected and their flange and web thickness were varied for built-up sections. A $W6 \times 6 \times 0.2 \times 0.2$ column from Table 6 had a width (B) of 5.9 in., depth (H) of 5.9 in., thickness of both the web and the flange of 0.197 in. respectively. These columns closely represent the dimensions of hot-rolled shapes of $W6 \times 20$, $W12 \times 96$, and $W16 \times 67$ sections. It should be noted that column $W6 \times 6 \times 0.2$ is generally atypical as a column size given the shallow depth of the column, but it was considered to evaluate the effect of web slenderness on the ultimate load capacity of the column. For each of these columns, the thickness of the flange (t_f) and the thickness of the web (t_w) were varied while

keeping the width and the depth of the original column size the same. Each of the different permutations of column cross-sections was evaluated using 100 ksi and 140 ksi steel material for built-up sections. From these various permutations, a total of twenty-four simulations were performed to study these parameters.

The length (L) of each column specimen was fixed as per the SSRC (2010) stub column equation, where L is in inches.

$$L = \min. ((2H + 10), (3H)) \quad (1)$$

Flange slenderness (λ_f) is the ratio of section width (B) to the flange thickness (t_f) and web slenderness (λ_w) is the ratio of section depth (h_o) to the web thickness (t_w). The combined parameters of flange and web slenderness control the section slenderness of the column. The thickness of each section was varied (keeping the width and depth of the section constant). The limiting width-to-thickness ratios (λ_r) from AISC 360 (2016) were used to classify each element as slender or non-slender. The AISC slenderness limits were applicable for steel grades only up to 65 ksi. These slenderness limits were used to test their applicability in classifying the elements of built-up W shapes of 100 ksi and 140 ksi. Appendix C gives detailed information on AISC slenderness limits. The W6×6×0.2×0.2 column had slender flanges and a slender web, with both λ_f and λ_w values less than their corresponding λ_r values. The slenderness ratios, λ_f and λ_w were varied to create slender - non-slender, non-slender - slender, and non-slender - non-slender sections with regards to the slenderness of the flange and the slenderness of the web as shown in Table 6.

Table 6: List of specimens for study of local buckling of wide flange built-up stub columns

Specimen ID (in × in × in × in)	F _y (ksi)	L (in)	Flange	Web	B (in)	H (in)	t _r (in)	t _w (in)
W6×6×0.2×0.2	100	17.72	Slender	Slender	5.91	5.91	0.20	0.20
W6×6×0.3×0.3	100	17.72	Slender	Non-Slender	5.91	5.91	0.28	0.28
W6×6×0.4×0.4	100	17.72	Non-Slender	Non-Slender	5.91	5.91	0.39	0.39
W6×6×0.4×0.2	100	17.72	Non-Slender	Slender	5.91	5.91	0.39	0.20
W12×12×0.6×0.6	100	35.20	Slender	Non-Slender	12.60	12.60	0.55	0.55
W12×12×0.4×0.4	100	35.20	Slender	Slender	12.60	12.60	0.39	0.39
W12×12×0.7×0.7	100	35.20	Non-Slender	Non-Slender	12.60	12.60	0.67	0.67
W12×12×0.7×0.4	100	35.20	Non-Slender	Slender	12.60	12.60	0.67	0.39
W10×16×0.3×0.3	100	41.50	Slender	Slender	9.84	15.75	0.29	0.29
W10×16×0.3×0.6	100	41.50	Slender	Non-Slender	9.84	15.75	0.29	0.63
W10×16×0.6×0.6	100	41.50	Non-Slender	Non-Slender	9.84	15.75	0.63	0.63
W10×16×0.6×0.3	100	41.50	Non-Slender	Slender	9.84	15.75	0.63	0.29
W6×6×0.2×0.2	140	17.72	Slender	Slender	5.91	5.91	0.20	0.20
W6×6×0.3×0.3	140	17.72	Slender	Non-Slender	5.91	5.91	0.28	0.28
W6×6×0.4×0.4	140	17.72	Non-Slender	Non-Slender	5.91	5.91	0.39	0.39
W6×6×0.4×0.2	140	17.72	Non-Slender	Slender	5.91	5.91	0.39	0.20
W12×12×0.6×0.6	140	35.20	Slender	Non-Slender	12.60	12.60	0.55	0.55
W12×12×0.4×0.4	140	35.20	Slender	Slender	12.60	12.60	0.39	0.39
W12×12×0.7×0.7	140	35.20	Non-Slender	Non-Slender	12.60	12.60	0.79	0.67
W12×12×0.7×0.4	140	35.20	Non-Slender	Slender	12.60	12.60	0.79	0.39
W10×16×0.3×0.3	140	41.50	Slender	Slender	9.84	15.75	0.29	0.29
W10×16×0.3×0.6	140	41.50	Slender	Non-Slender	9.84	15.75	0.29	0.71
W10×16×0.6×0.6	140	41.50	Non-Slender	Non-Slender	9.84	15.75	0.63	0.71
W10×16×0.6×0.3	140	41.50	Slender	Slender	9.84	15.75	0.63	0.29

4.1.2 RESIDUAL STRESS

Although the effect of residual stresses on the behavior of HS3 stub columns is relatively less when compared with CMS columns, there is a need to apply them to simulate the expected, realistic behavior of local buckling in stub columns. The relationship between the yield strength of HS3 and residual stresses was unknown, so three different empirical residual stress models were used. The residual stresses for the wide flange built-up specimens were obtained using the following residual stress models from the experimental studies used to benchmark the experimental test: Ban et al. (2013) for 140 ksi (960 MPa) specimens, Cao et al. (2020) for 120 ksi (800 MPa) specimens

and Sun et al. (2019) for 100 ksi (690 MPa) specimens. The residual stresses obtained from the models were applied to the cross-section of the FE model using the distribution shown in Table 3. Table 7 shows the applied residual stress along the cross-section of flange and web for all built-up wide flange specimens of W6×6. Appendix A has information on applied residual stresses in the remaining built-up sections.

Table 7: Applied residual stresses in built-up specimen

Specimen ID	F_y (ksi)	Flange Residual Stress Distribution (ksi)	Web Residual Stress Distribution (ksi)
W6×6×0.2 ×0.2	100		
W6×6×0.3 ×0.3	100		
W6×6×0.4 ×0.4	100		
W6×6×0.4 ×0.2	100		

4.1.3 RESULTS

All the specimens analyzed using ABAQUS failed by the local buckling mode. But this local buckling did not take place at the center for the majority of the stub column specimens. Most of the specimens showed both web and flange buckling. The specimen which had only non-slender elements failed by squash load before showing local buckling. These specimens predominantly showed only flange buckling as the local buckling mode. Fig.28 shows the local buckling modes observed in $W12 \times 12 \times 0.4 \times 0.4$ (slender-slender section) and $W12 \times 12 \times 0.7 \times 0.7$ (non-slender – non-slender section).

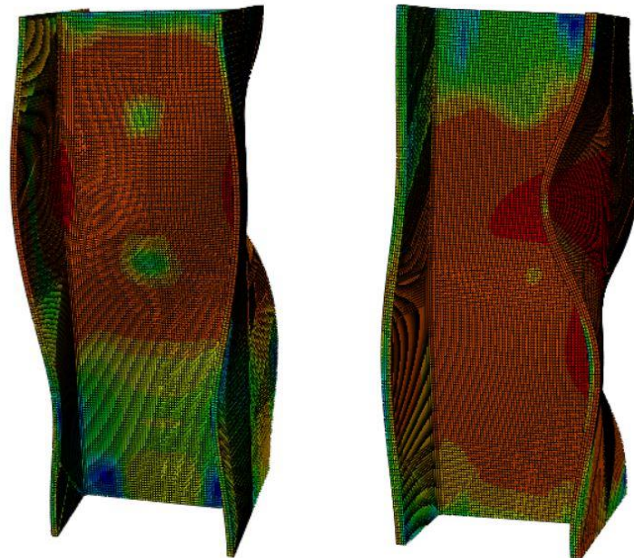


Fig. 28: Local buckling mode observed in $W12 \times 12 \times 0.4 \times 0.4$ (left) and $W12 \times 12 \times 0.7 \times 0.7$ (right) sections

The axial load obtained at the centroid of the cross-section was normalized by dividing it by the gross area of cross-section (A_g). Fig. 29 shows the comparison of normalized axial load with axial deformation for $W6 \times 6$ built-up stub columns of grade 100 ksi. The slenderness ratio for the web and the flange of $W6 \times 6 \times 0.2 \times 0.2$ was found to be 28.0 and 15.0. The limiting slenderness ratios for the web and flange (λ_r) of $W6 \times 6 \times 0.2 \times 0.2$ was found to be $25.4 < 28.0$ and $9.5 < 15.0$. This made the $W6 \times 6 \times 0.2 \times 0.2$ section the only stub column with both web and flange to have slender elements

among the other W6×6 sections in Fig. 29. This made the W6×6×0.2×0.2 section behave different (ultimate load being significantly lower) than the other W6×6 sections in Fig. 29. It can be seen from Fig. 29 that the W6×6×0.2×0.2 section with the lowest ultimate load and the stockier sections (with thicker webs and flanges) exhibited increased ultimate load.

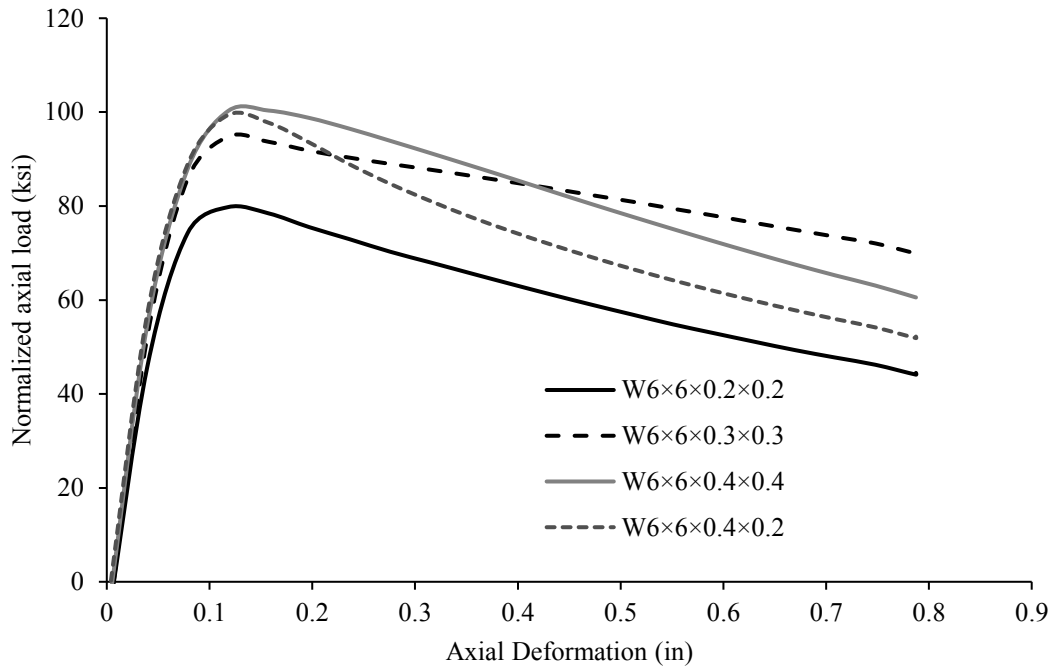


Fig. 29: Normalized axial load vs. axial deformation for W6×6 built-up stub columns of grade 100 ksi

Fig. 30 and Fig. 31 show the comparison of normalized axial load with axial deformation for W12×12 and W10×16 built-up stub columns of grade 100 ksi. Like the discussion in Fig. 29, W12×12×0.4×0.4 and W10×16×0.3×0.3 had both of its web and flange elements as slender. This made them behave different (had significantly lower ultimate load) from its counterparts as indicated in Fig. 30 and Fig. 31. As the section became thicker, the section slenderness decreased (web and flange slenderness) and the ultimate load increased. Appendix F has the information on the comparison curves of axial load with axial deformation for all built-up W shapes.

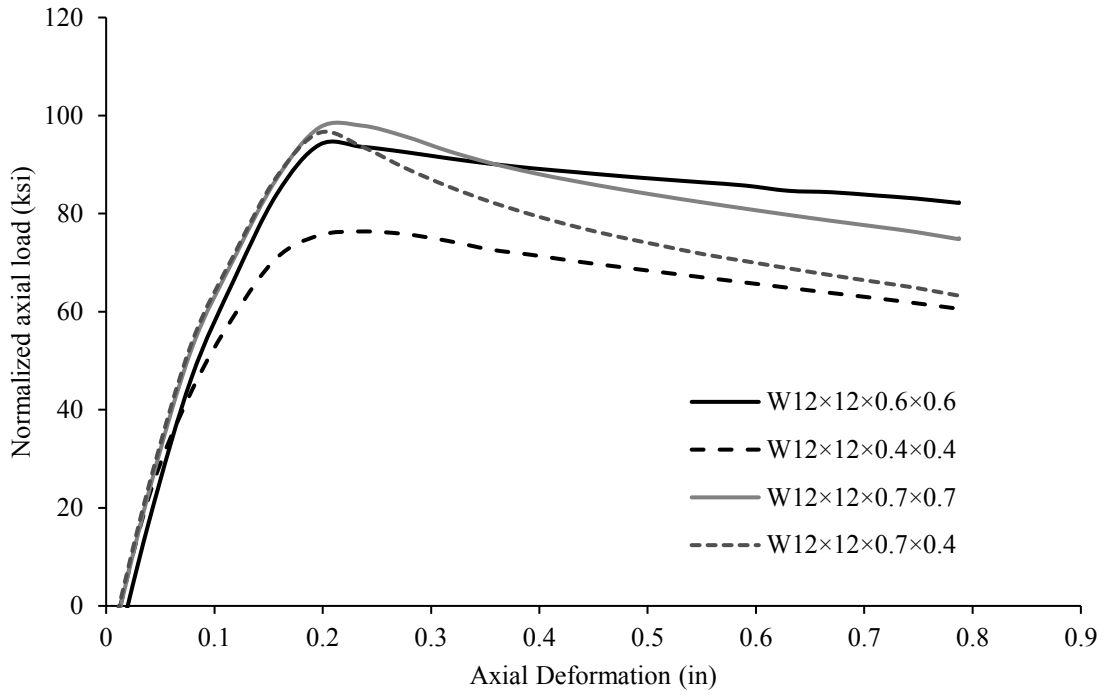


Fig. 30: Normalized axial load vs. axial deformation for W12×12 built-up stub columns of grade 100 ksi

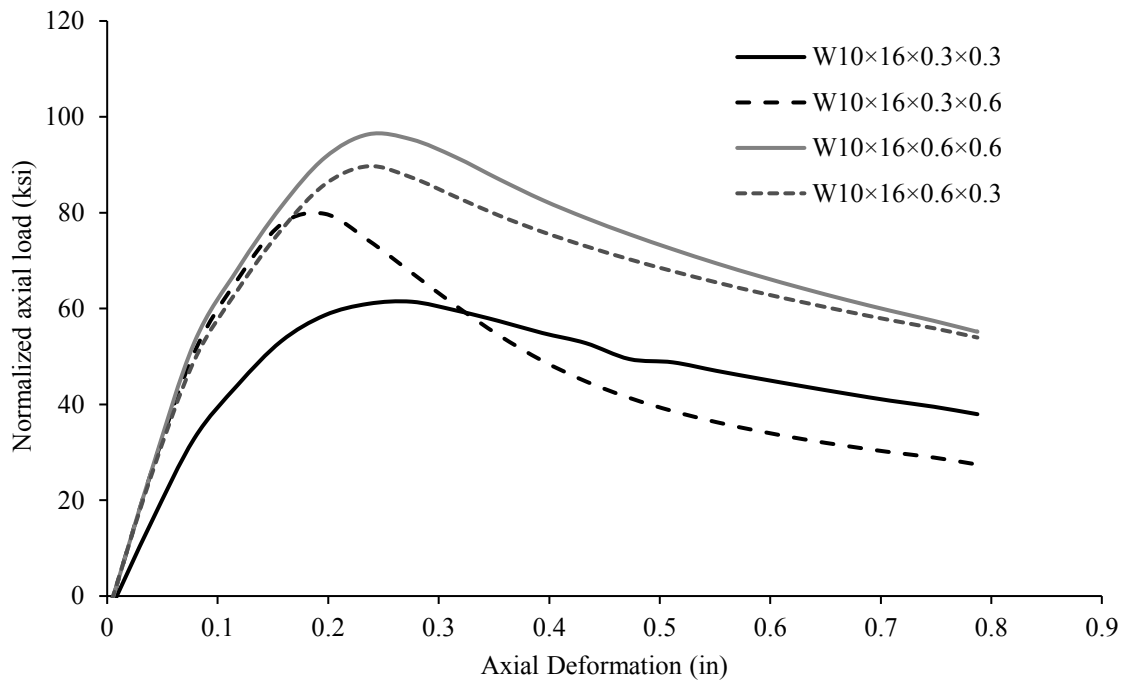


Fig. 31: Normalized axial load vs. axial deformation for W10×16 built-up stub columns of grade 100 ksi

Fig. 32, Fig. 33, and Fig. 34 show the comparison of normalized axial load with axial deformation for W6×6, W12×12, and W10×16 built-up stub columns of grade 140 ksi. Like the discussion in Fig. 29, sections W6×6×0.2×0.2, W6×6×0.2×0.2, and W10×16×0.3×0.3 in Fig. 32, Fig. 33, and Fig. 34 had both of its web and flange elements as slender. This made these sections have the significantly lowest ultimate load than other sections. And, as the sections became thicker, the section slenderness decreased (web and flange slenderness) and the ultimate load increased.

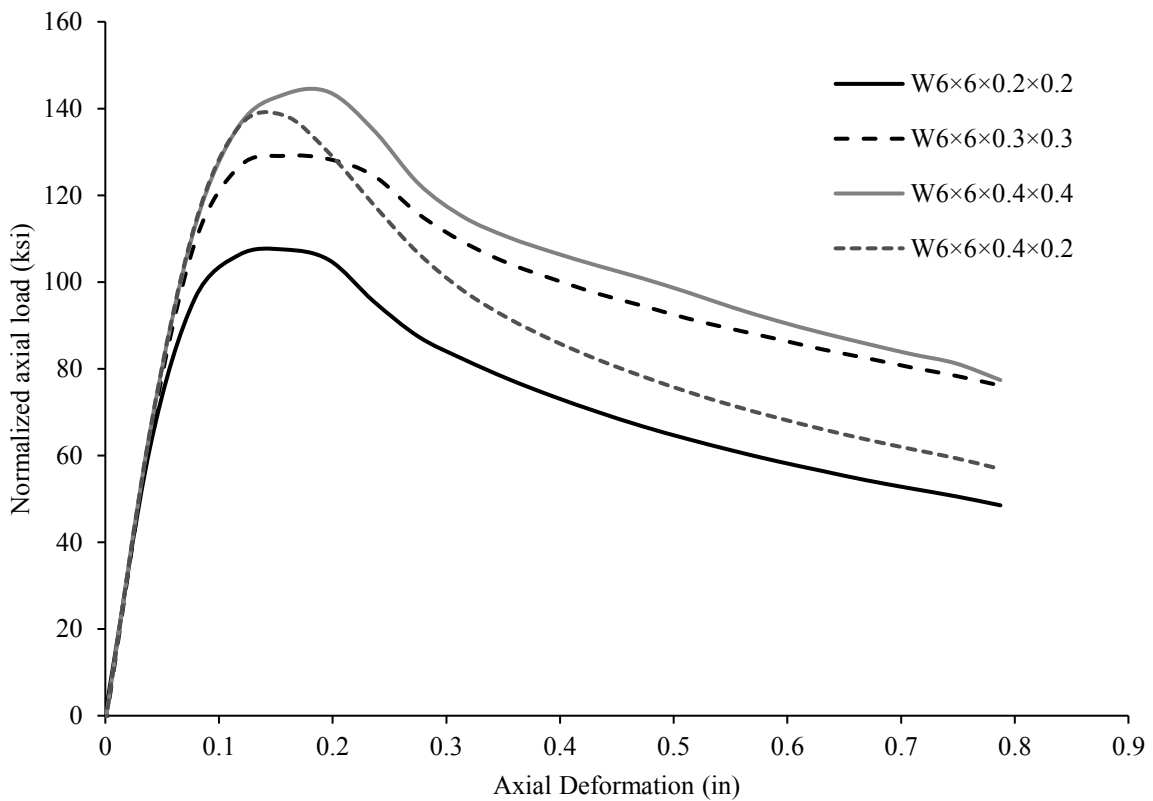


Fig. 32: Normalized axial load vs. axial deformation for W6×6 built-up stub columns of grade 140 ksi

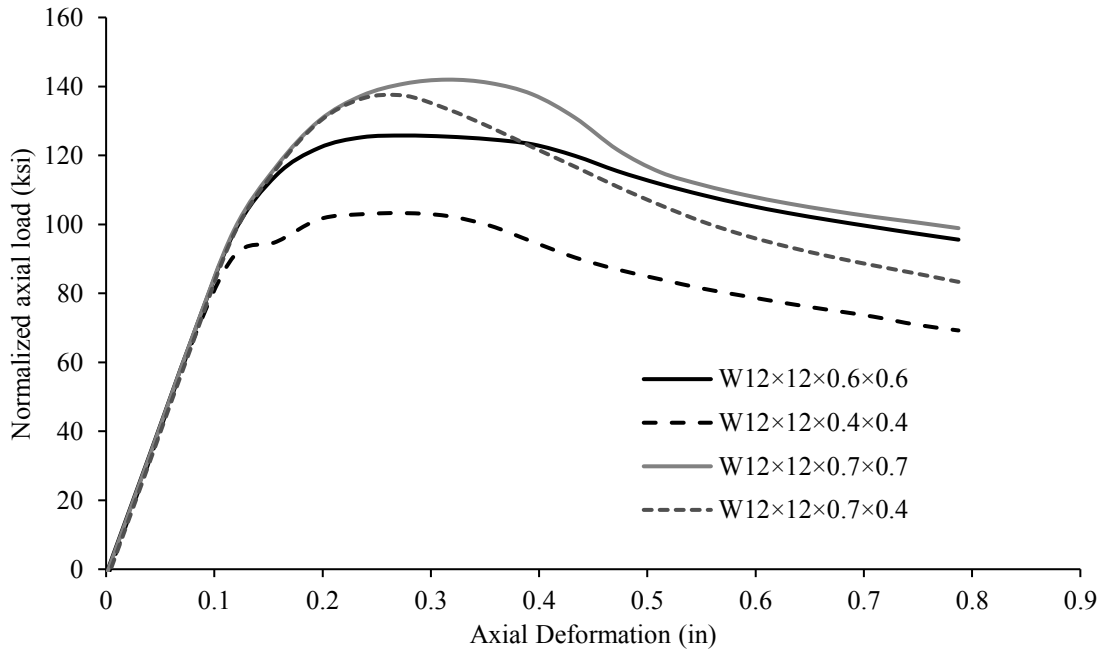


Fig. 33: Normalized axial load vs. axial deformation for W12x12 built-up stub columns of grade 140 ksi

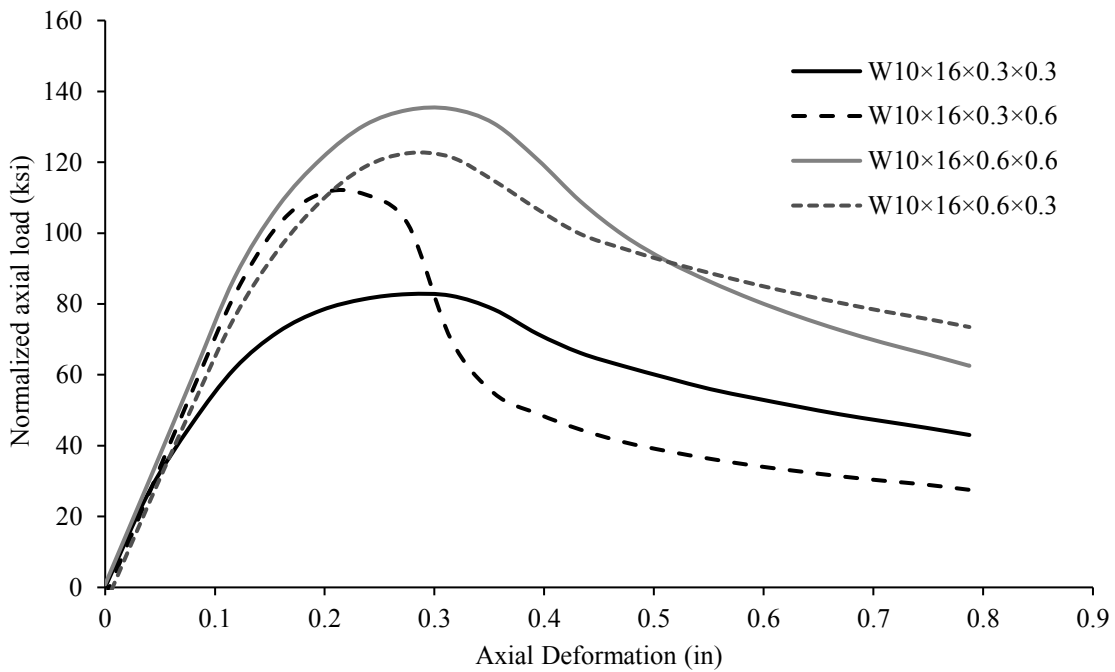


Fig. 34: Normalized axial load vs. axial deformation for W10x16 built-up stub columns of grade 140 ksi

Similar built-up sections were compared with each other by varying the yield strength of the specimen to understand the impact of yield strength on the ultimate load of the stub column as

shown in Fig. 35. It was found that the ultimate load of the specimen increased with an increase in the yield strength of the specimen. This result was consistent across all the built-up sections considered for analysis. This increase in the ultimate load was most dominant in stockier sections and less prevalent in slender sections. This might be due to the impact of yield strength being more predominant in stockier sections. Fig. 34 shows the comparison of axial load vs. axial deformation curves of built-up W12×12 sections with different steel grades. When comparing W12×12×0.7 sections of 100 ksi and 140 ksi, there was a 62% increase in ultimate load. While comparing W12×12×0.4 sections of 100 ksi and 140 ksi, there was only 35% increase in ultimate load.

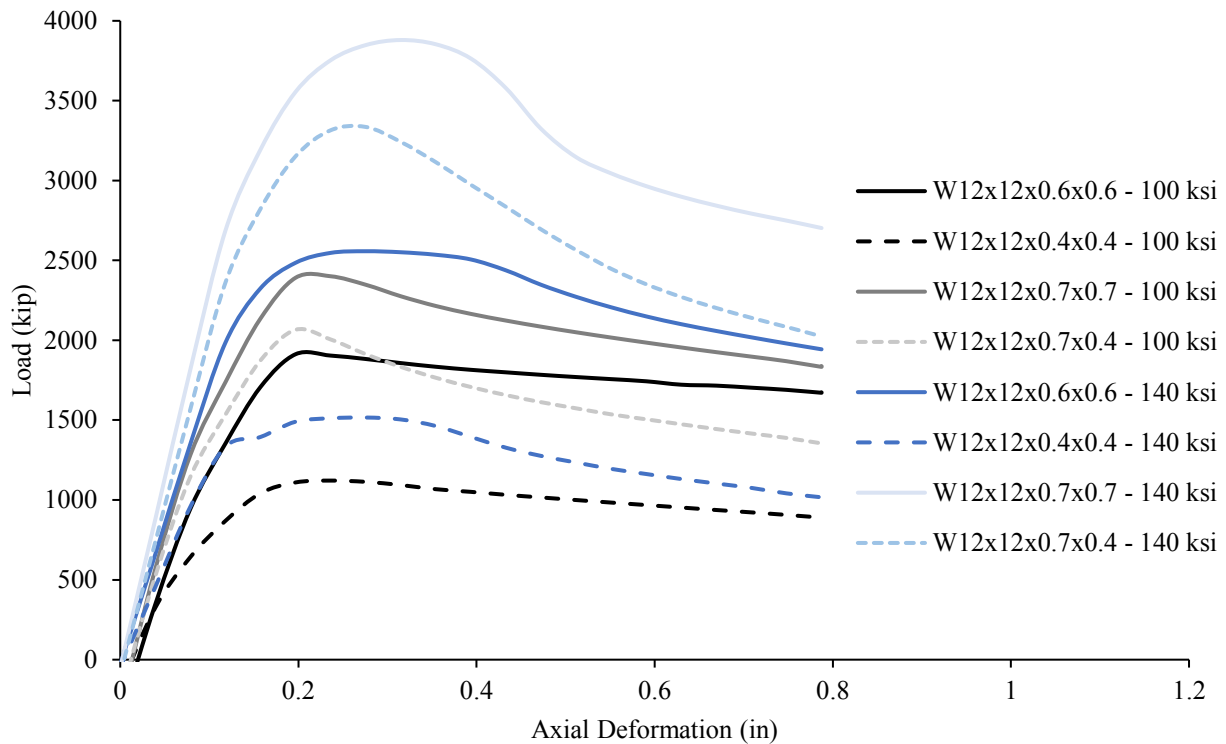


Fig. 35: Comparison of Axial load vs. axial deformation for built-up W12×12 with different steel grades

4.1.4 EVALUATION OF AISC DESIGN EQUATIONS

The applicability of local buckling equations and flexural buckling equations from AISC 360 (2016) to calculate the nominal compressive strength of the column (P_n) were evaluated. The local buckling equations for columns were given by Section E7 of the AISC (2016) *Specification* for sections with slender elements and the flexural buckling equations were given by Section E3 of the AISC (2016) *Specification*. The nominal compressive strength (P_n) for the slender elements is the lowest value based on the critical stress (F_{cr}) as determined by the limit states of flexural buckling, torsional buckling, and flexural torsional buckling in interaction with the local buckling. Equation E7-1 gives the expression for P_n as shown below.

$$P_n = F_{cr}A_e \quad (2)$$

where A_e is the summation of effective areas of the cross-section obtained by the reduced effective width b_e and reduced effective depth d_e , as given by equations E7-2 and E7-3 in the *specification*. Appendix E gives a detailed information on the calculation of nominal compressive strength (P_n) for 100 ksi W12×12×0.6×0.6 built-up column.

Table 8 gives a detailed comparison of ABAQUS simulated ultimate load (P_u) and local buckling load (P_L) with AISC nominal compressive strength (P_n) from the FE model for 100 ksi built-up stub columns. The specimen ID indicates the depth, width, flange thickness (t_f), and web thickness (t_w) of the column; for instance, W6×6×0.2×0.2 represents the original W6 column from Table 6. The element thicknesses corresponding to each column cross-section are given in Table 6. Among the twelve tests conducted, the mean value of P_u/P_n was found to be 1.02 with a coefficient of variation (COV) of 2.65%, and the mean value of P_L/P_n was found to be 1.02 with a COV of 2.55%. The local buckling load and the ultimate load were different for thicker cross-sections and

there is a need to study them. The local buckling load was equal to the ultimate load in more than 90% of the cases and was less than the ultimate load, but within 2% for the remaining cases. This meant that the local buckling load (P_L) can be used to calculate the strength of the column in all cases. A failure model or damage data applied to the FE model would give a better picture of the understanding of the relationship between the two quantities.

Table 9 gives a detailed comparison of simulated ultimate load (P_u) and local buckling load (P_L) with AISC nominal compressive strength (P_n) from the FE model for 140 ksi built-up columns. Among the twelve tests, the mean value of P_u/P_n was found to be 1.08 with a COV of 5.02%, and the mean value of P_L/P_n was found to be 1.07 with a COV of 4.66%. This means that the design method in the AISC *Specification* can be used in the design of wide flange built-up section columns of grade 100 ksi and 140 ksi.

Table 8: Comparison of AISC compressive strength with ultimate load and local buckling load for 100 ksi built-up columns

Specimen ID (in × in × in × in)	L (in)	P_u (kip)	P_n (kip)	P_u / P_n	P_L (kip)	P_L / P_n
W6×6×0.2×0.2	17.72	280.96	272.54	1.03	280.96	1.03
W6×6×0.3×0.3	17.72	459.05	460.34	1.00	459.05	1.00
W6×6×0.4×0.4	17.72	679.93	662.80	1.03	679.35	1.02
W6×6×0.4×0.2	17.72	573.42	553.32	1.04	573.42	1.04
W12×12×0.6×0.6	35.20	1912.36	1907.85	1.00	1912.36	1.00
W12×12×0.4×0.4	35.20	1121.13	1106.60	1.01	1109.66	1.00
W12×12×0.7×0.7	35.20	2400.71	2401.14	1.00	2391.13	1.00
W12×12×0.7×0.4	35.20	2065.56	2063.37	1.00	2065.56	1.00
W10×16×0.3×0.3	41.50	617.95	570.71	1.08	613.60	1.08
W10×16×0.3×0.6	41.50	1219.58	1246.51	0.98	1219.58	0.98
W10×16×0.6×0.6	41.50	2084.78	2049.83	1.02	2084.78	1.02
W10×16×0.6×0.3	41.50	1492.99	1439.88	1.04	1492.99	1.04
Mean				1.018		1.017
COV				2.648%		2.553%

Table 9: Comparison of AISC compressive strength with ultimate load and local buckling load for 140 ksi built-up columns

Specimen ID (in × in × in × in)	L (in)	P _u (kip)	P _n (kip)	P _u / P _n	P _L (kip)	P _L / P _n
W6×6×0.2×0.2	17.72	378.52	336.75	1.12	378.52	1.12
W6×6×0.3×0.3	17.72	625.13	599.00	1.04	625.13	1.04
W6×6×0.4×0.4	17.72	974.35	919.44	1.06	970.76	1.06
W6×6×0.4×0.2	17.72	798.46	755.60	1.06	798.46	1.06
W12×12×0.6×0.6	35.20	2557.30	2475.05	1.03	2546.98	1.03
W12×12×0.4×0.4	35.20	1516.05	1362.43	1.11	1489.90	1.09
W12×12×0.7×0.7	35.20	3879.64	3719.45	1.04	3848.01	1.03
W12×12×0.7×0.4	35.20	3335.56	3212.56	1.04	3314.70	1.03
W10×16×0.3×0.3	41.50	832.81	686.11	1.21	818.93	1.19
W10×16×0.3×0.6	41.50	1832.90	1777.23	1.03	1829.43	1.03
W10×16×0.6×0.6	41.50	3076.64	2945.11	1.04	3069.13	1.04
W10×16×0.6×0.3	41.50	2039.77	1860.05	1.10	2039.77	1.10
Mean				1.075		1.069
COV				5.023%		4.663%

The results of the twenty-four FE analyses of built-up sections are summarized in the following figures. The load ratio of the ultimate load (P_u) obtained by FE analysis and the nominal compressive strength (P_n) determined from AISC 360 (2016) were plotted against the interactive slenderness of the column. The interactive slenderness is being defined as $(\lambda_f/\lambda_{rf})(\lambda_w/\lambda_{rw})$, which is calculated as the flange slenderness relative to its limiting ratio multiplied by the web slenderness relative to its limiting ratio. Because both web and flange slenderness varied in this parametric study, simply comparing the web slenderness or the flange slenderness did not produce meaningful relationships.

The interactive slenderness considers the combined effect of web and flange slenderness on the column behavior. This relationship between load ratio and interactive slenderness for built-up members is shown in Fig. 36. Fig. 37 and Fig. 38 show the comparison of P_u from FE analysis and P_n. The load ratio (P_u/P_n) in Fig. 36 was greater than 1.0 for more than 95% of specimens tested, which demonstrated that the nominal strength predicted by AISC 360 (2016) for HS3 built-up

columns was conservative for both 100 ksi and 140 ksi specimens. The 140 ksi specimens were more conservative than the 100 ksi specimens. There was not much difference in the load ratio (P_u/P_n) with low interactive slenderness (≤ 2.0). There was a slight increase in load ratio with an increase in interactive slenderness greater than 2.0. This suggested that the local buckling equations were slightly more conservative at larger slenderness limits. The diagonal line in Fig. 37 and Fig. 38 show an exact match between P_u and P_n values. The values above this line indicate a higher P_u value and the values below the line indicate a higher P_n value. The values on the line indicate an exact match between the P_u and P_n values. For 100 ksi specimen, there were more than 95% exact matches and for 140 ksi specimen, 90% of the points lay above the line. This indicated that for 140 ksi specimen, FE analysis produced higher ultimate load that the estimated by AISC 360 (2016).

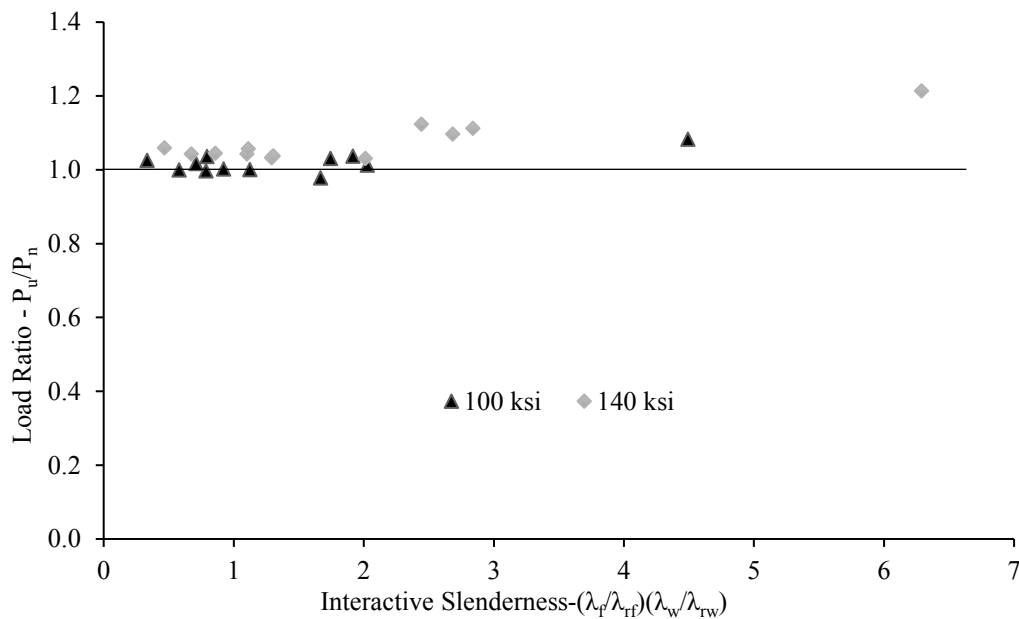


Fig. 36: Comparison of load ratio - P_u/P_n and interactive slenderness - $(\lambda_f/\lambda_{rf})(\lambda_w/\lambda_{rw})$ for built-up members

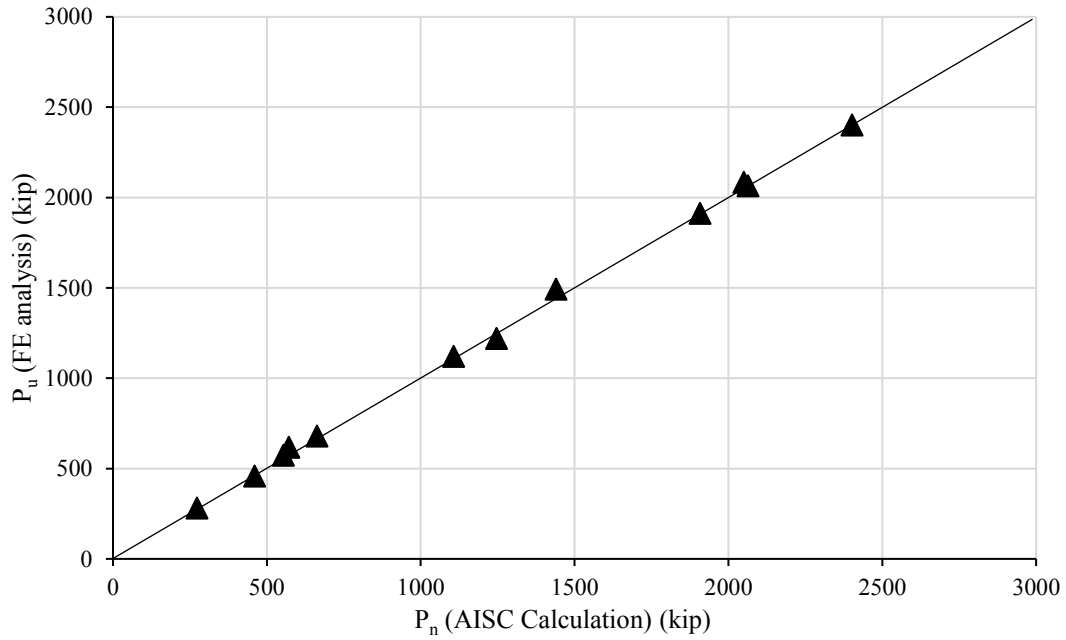


Fig. 37: Comparison of P_u (FE analysis) and P_n (AISC) for 100 ksi built-up members

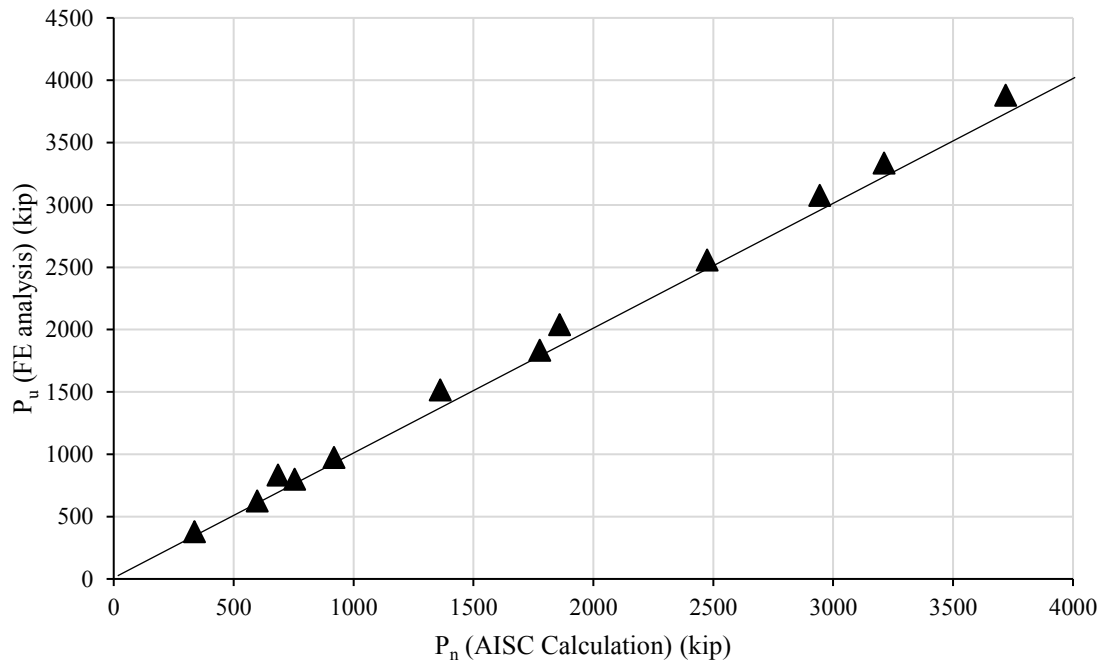


Fig. 38: Comparison of P_u (FE analysis) and P_n (AISC) for 140 ksi built-up members

A plot of load ratio (P_u/P_y) against the interactive slenderness of the column for built-up specimen is shown in Fig.39 and Fig.40 for 100 ksi and 140 ksi specimens respectively. P_y is the yield load of the specimen obtained from yield stress multiplied by gross cross-sectional area, A_g . From the graphs in Fig.39 and Fig.40, as the interactive slenderness increases, the load ratio (P_u/P_y) of the built-up column decreases. This means that as the section slenderness of the column increases, the ultimate load capacity of the column decreased in built-up members. This relationship is approximately linear. This shows that yielding across the entire cross-section has not occurred. This is to be expected in local buckling cases.

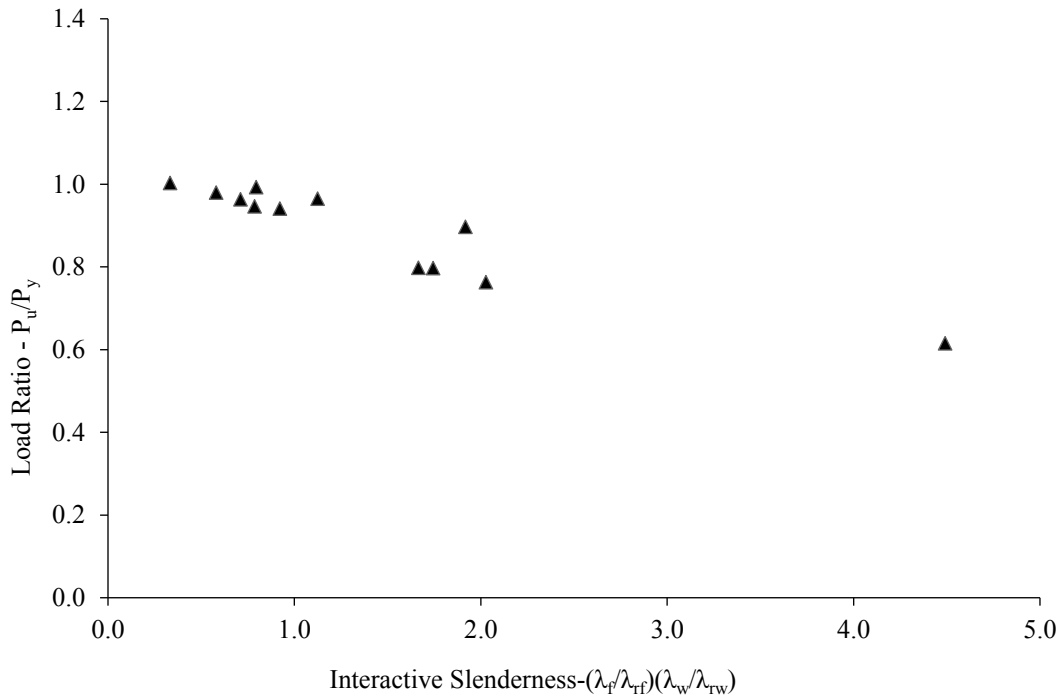


Fig. 39: Comparison of load ratio and interactive slenderness for 100 ksi built-up members

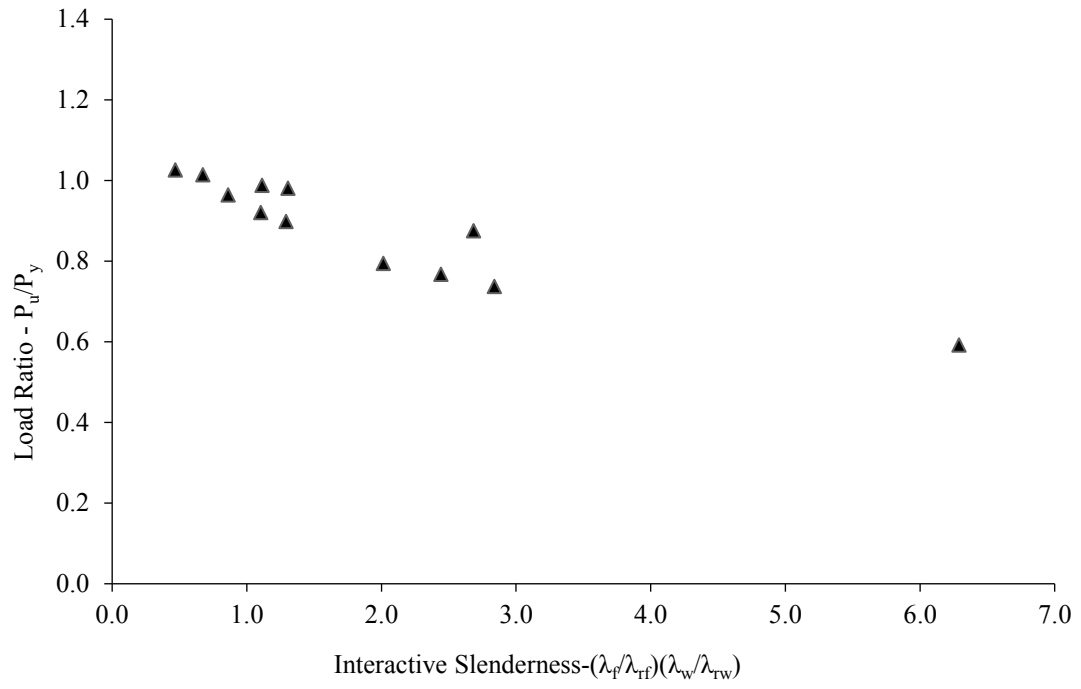


Fig. 40: Comparison of load ratio and interactive slenderness for 140 ksi built-up member

4.2 LOCAL BUCKLING OF ROLLED W SHAPES

4.2.1 PARAMETERS

Three initial column sizes: W10×11×1×0.6, W12×12×0.7×0.4, and W14×14×0.9×0.5 were selected and their flange and web thickness were varied for hot-rolled sections. These columns represent the dimensions of hot-rolled shapes of W10×88, W12×72, and W14×109 sections. A W10×88 section was written as W10×11×1×0.6 in Table 9 so that it was easier to compare thicknesses with other non-standard sections (not existent in practice). A W10×11×1×0.6 had a width (B) of 10.3 in., depth (H) of 10.8 in., web thickness of 0.99 in., and flange thickness of 0.6 in. respectively. For each of these columns, the thickness of the flange (t_f) and the thickness of the web (t_w) were varied while keeping the width and the depth of the original column size the same. The length consideration and thickness consideration for the hot-rolled specimen was the same as that in section 4.1.1. The modeling approach, material properties, boundary conditions, and initial geometrical imperfections were the same as those described in Chapter 3 for hot-rolled W shapes. Hot-rolled sections are currently available only up to 65 ksi in the United States market. And there is no mere possibility of 140 ksi specimen being produced before 120 ksi steel. This is the primary reason for choosing 120 ksi steel material over 140 ksi material for creating FE models. Each of the different permutations of column cross-sections was evaluated using 100 ksi and 120 ksi steel material for hot-rolled sections. From these various permutations, a total of twenty-four simulations were performed to study the parameters of yield strength, section slenderness. Table 10 shows the list of specimens that were chosen for the study of local buckling in HS3 hot-rolled stub columns. The limiting width-to-thickness ratios (λ_r) from AISC 360 (2016) were used to classify each element of rolled section in Table 10 as slender or non-slender. The AISC slenderness limits were applicable for steel grades only up to 65 ksi. These slenderness limits were used to test

their applicability in classifying the elements of rolled W shapes of 100 ksi and 120 ksi. Appendix C gives detailed information on AISC slenderness limits.

Table 10: List of specimens for study of local buckling of wide flange hot-rolled stub columns

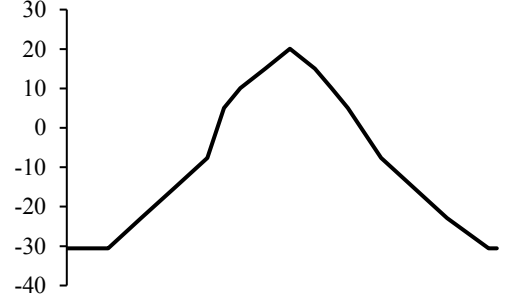
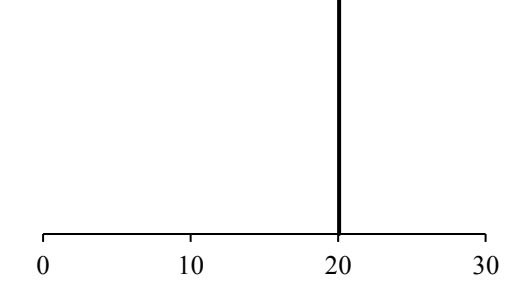
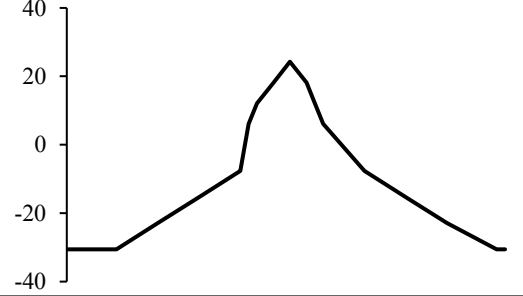
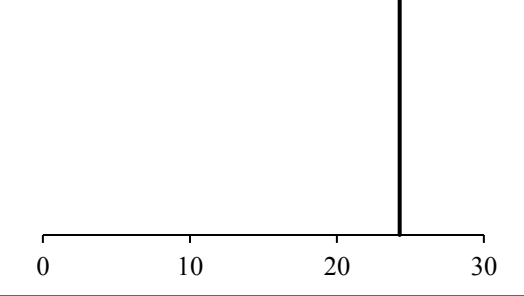
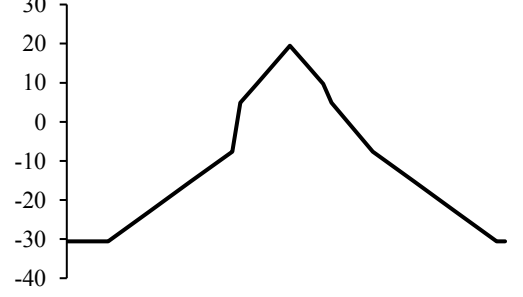
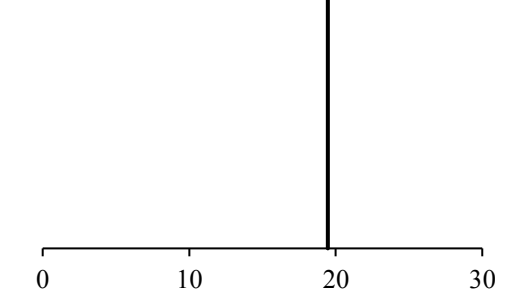
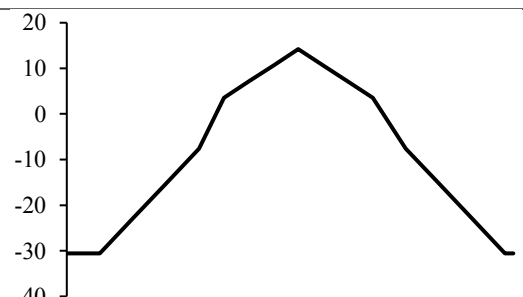
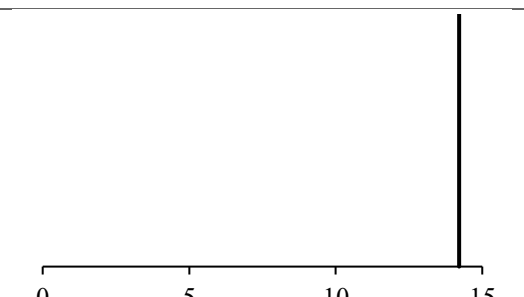
Specimen ID (in × in × in × in)	F_y (ksi)	L (in)	Flange	Web	B (in)	H (in)	t_f (in)	t_w (in)
W10×11×1×0.6	100	31.6	Non-Slender	Non-Slender	10.30	10.80	0.99	0.61
W10×11×1×0.3	100	31.6	Non-Slender	Slender	10.30	10.80	0.99	0.30
W10×11×0.5×0.3	100	31.6	Slender	Slender	10.30	10.80	0.50	0.30
W10×11×0.5×0.6	100	31.6	Slender	Non-Slender	10.30	10.80	0.50	0.61
W12×12×0.7×0.4	100	34.6	Non-Slender	Slender	12.00	12.30	0.67	0.43
W12×12×0.7×0.9	100	34.6	Non-Slender	Non-Slender	12.00	12.30	0.67	0.90
W12×12×0.5×0.9	100	34.6	Slender	Non-Slender	12.00	12.30	0.50	0.90
W12×12×0.5×0.4	100	34.6	Slender	Slender	12.00	12.30	0.50	0.43
W14×14×0.9×0.5	100	39.2	Non-Slender	Non-Slender	14.30	14.60	0.86	0.53
W14×14×0.7×0.5	100	39.2	Slender	Non-Slender	14.30	14.60	0.70	0.53
W14×14×0.7×0.3	100	39.2	Slender	Slender	14.30	14.60	0.70	0.30
W14×14×0.7×0.3	100	39.2	Non-Slender	Slender	14.30	14.60	0.86	0.30
W10×11×1×0.6	120	31.6	Non-Slender	Non-Slender	10.30	10.80	0.99	0.61
W10×11×1×0.3	120	31.6	Non-Slender	Slender	10.30	10.80	0.99	0.30
W10×11×0.5×0.3	120	31.6	Slender	Slender	10.30	10.80	0.50	0.30
W10×11×0.5×0.6	120	31.6	Slender	Non-Slender	10.30	10.80	0.50	0.61
W12×12×0.7×0.4	120	34.6	Slender	Slender	12.00	12.30	0.67	0.43
W12×12×0.9×0.9	120	34.6	Non-Slender	Non-Slender	12.00	12.30	0.90	0.90
W12×12×0.5×0.9	120	34.6	Slender	Non-Slender	12.00	12.30	0.50	0.90
W12×12×0.9×0.4	120	34.6	Non-Slender	Slender	12.00	12.30	0.90	0.43
W14×14×0.9×0.5	120	39.2	Non-Slender	Slender	14.30	14.60	0.86	0.53
W14×14×0.7×0.5	120	39.2	Slender	Slender	14.30	14.60	0.70	0.53
W14×14×0.7×0.7	120	39.2	Slender	Non-Slender	14.30	14.60	0.70	0.70
W14×14×0.9×0.7	120	39.2	Non-Slender	Non-Slender	14.30	14.60	0.86	0.70

4.2.2 RESIDUAL STRESS

The residual stresses in hot-rolled sections are different from built-up members due to the difference in the pattern of differential cooling and the stresses creating during the welding process of the built-up section. The residual stresses for the wide flange hot-rolled specimens were obtained from SSRC (2010) residual stress model. This residual stress model was originally developed by Galambos and Ketter (1959). Table 11 shows the applied residual stresses in the hot-

rolled W10×11 specimen. A detailed calculation of residual stresses is shown in Appendix A for more information. Appendix A has information on applied residual stresses in the remaining hot-rolled sections.

Table 11: Applied residual stresses in hot-rolled specimen

Specimen ID	F_y (ksi)	Flange Residual Stress Distribution (ksi)	Web Residual Stress Distribution (ksi)
W10×11×1×0.6	100		
W10×11×1×0.3	100		
W10×11×0.5×0.3	100		
W10×11×0.5×0.6	100		

4.2.3 RESULTS

Most of the specimens analyzed using ABAQUS failed by the local buckling mode. Like built-up shapes, the local buckling did not happen at the center of the column for most hot-rolled shapes. All the specimens that showed local buckling mode showed both web and flange buckling. Fig.41 shows the local buckling mode observed in $W10\times11\times1\times0.6$ (slender-slender section). The specimens which had non-slender flange and web elements failed by flexural buckling. Fig.42 shows the flexural buckling modes observed in $W10\times11\times0.5\times0.3$ (non-slender – non-slender section). Among the many sections considered for analysis, the stocky sections had higher ultimate load and when the section slenderness was increased there was a decrease in the ultimate load. Fig. 43 shows the comparison of axial load with axial deformation for $W10\times11$ hot-rolled stub columns of grade 100 ksi. It can be seen from Fig. 43 that the stockier sections (with thicker webs and flanges) exhibited increased ultimate load. There was a plateau observed in load deformation curves for all the stockier sections that underwent flexural buckling.

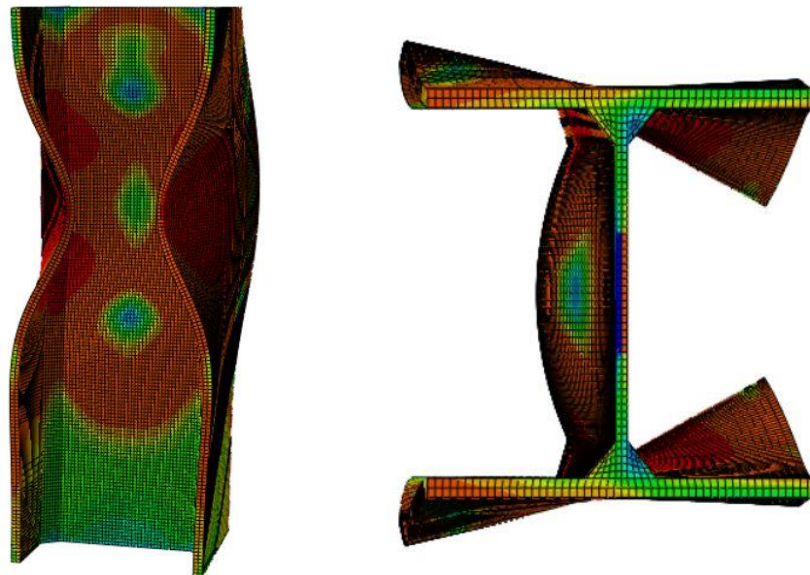


Fig. 41: Local buckling observed in $W10\times11\times0.5\times0.3$ column - left (front view), right (top view)

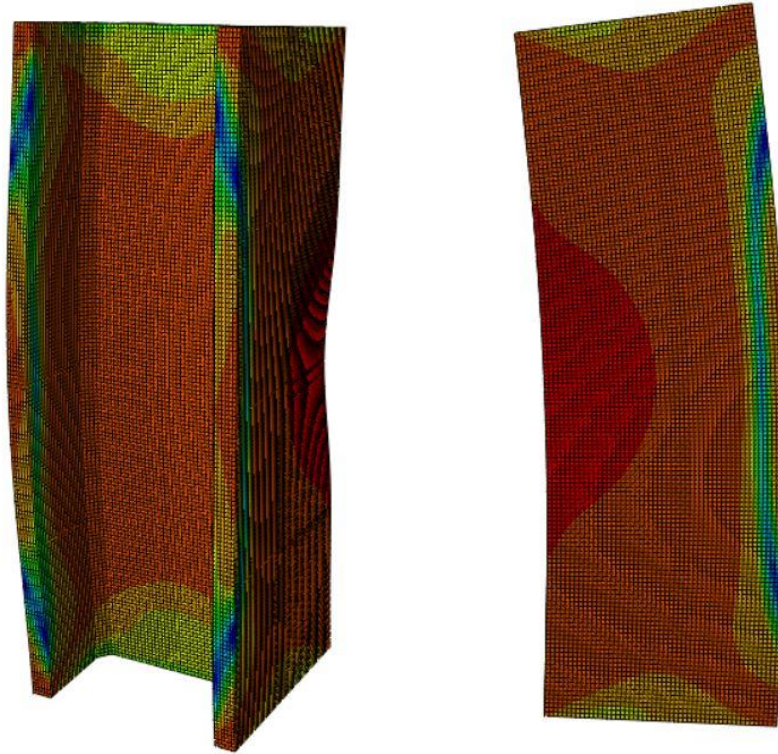


Fig. 42: Flexural buckling observed in $W10 \times 11 \times 1 \times 0.6$ column - left (3D view), right (side view)

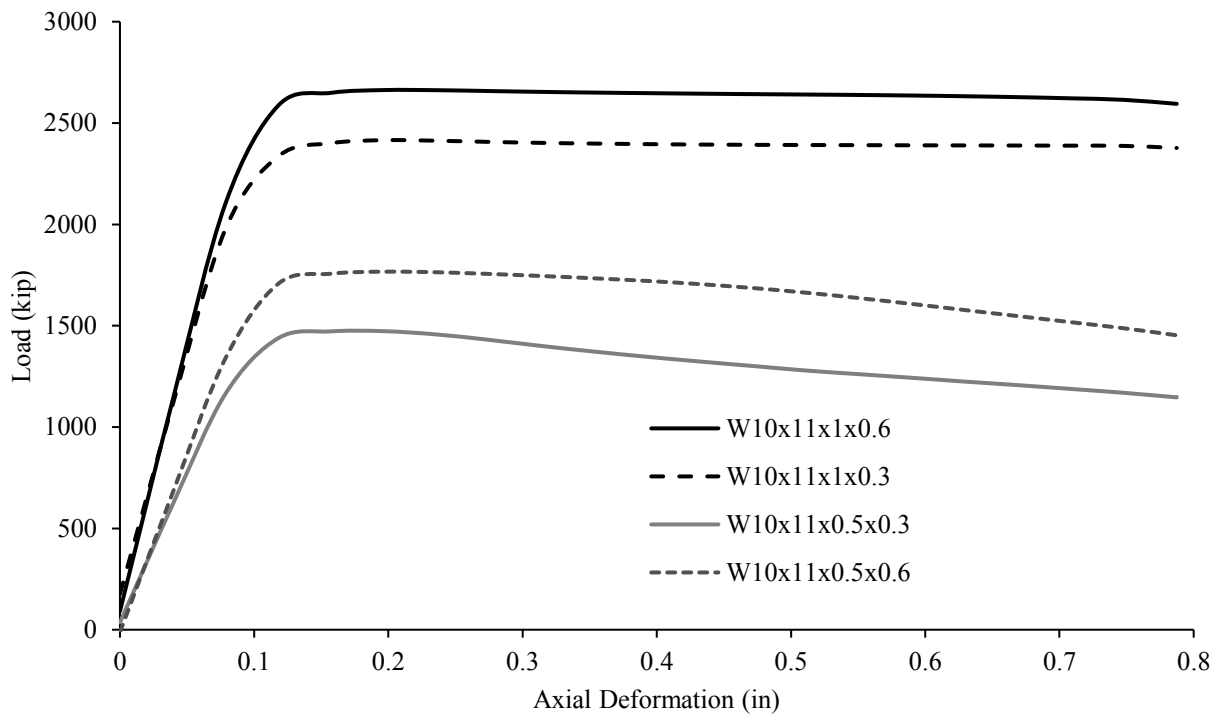


Fig. 43: Axial load vs. axial deformation for $W10 \times 11$ hot-rolled stub columns of grade 100 ksi

Fig. 44, and Fig. 45 show the comparison of axial load with axial deformation for W12×12, and W14×14 hot-rolled stub columns of grade 100 ksi. As the section became thicker, the section slenderness decreased (web and flange slenderness) and the ultimate load increased. It can be seen from the figures that the sections undergo plateauing after reaching the ultimate load. This indicated that such sections underwent flexural buckling instead of displaying local buckling behavior. This behavior of hot-rolled sections was consistent throughout and it was the same for 120 ksi sections. Fig. 46, Fig. 47, and Fig. 48 show the comparison of axial load with axial deformation for W10×11, W12×12, and W14×14 hot-rolled stub columns of grade 120 ksi. The axial load obtained at the centroid of the cross-section was normalized by dividing it by the gross area of cross-section (A_g). Appendix F has more information on the comparison curves of normalized axial load with axial deformation for all hot-rolled W shapes.

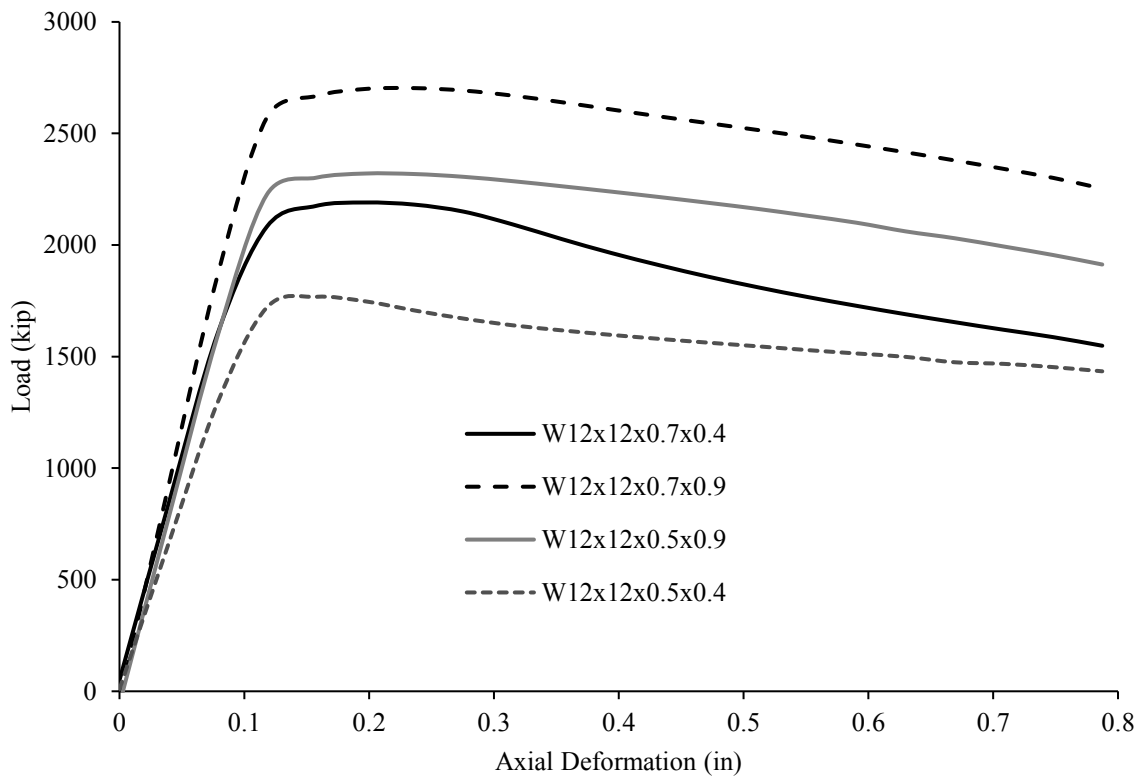


Fig. 44: Axial load vs. axial deformation for W12×12 hot-rolled stub columns of grade 100 ksi

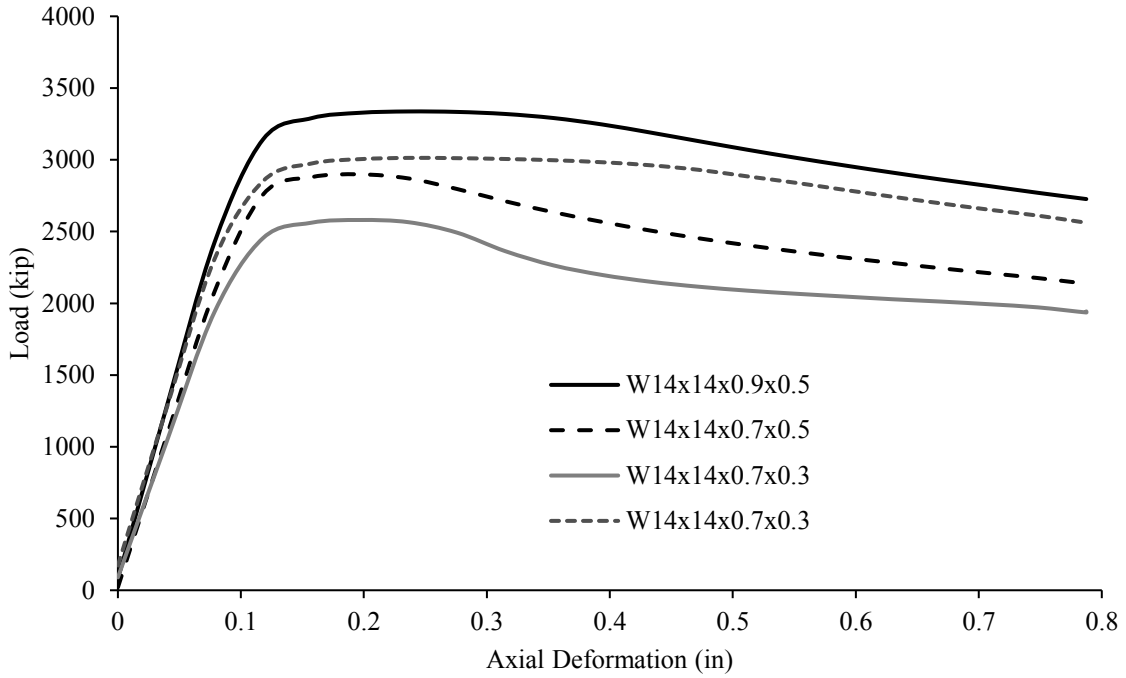


Fig. 45: Axial load vs. axial deformation for W14x14 hot-rolled stub columns of grade 100 ksi

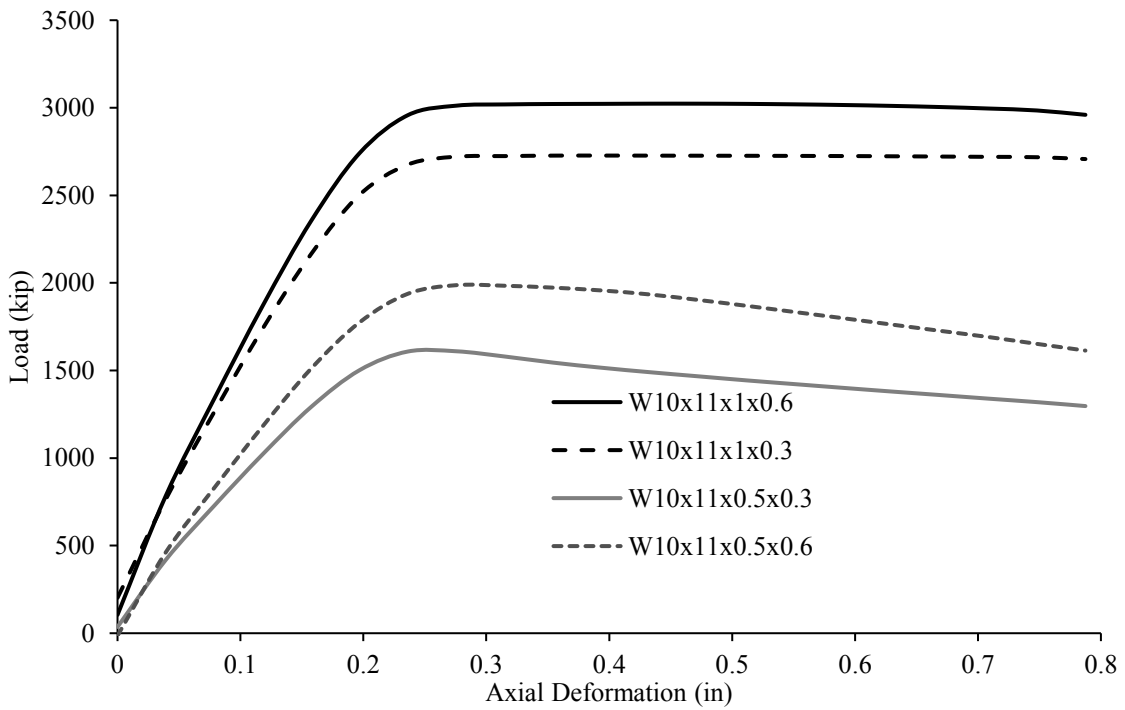


Fig. 46: Axial load vs. axial deformation for W10x11 hot-rolled stub columns of grade 120 ksi

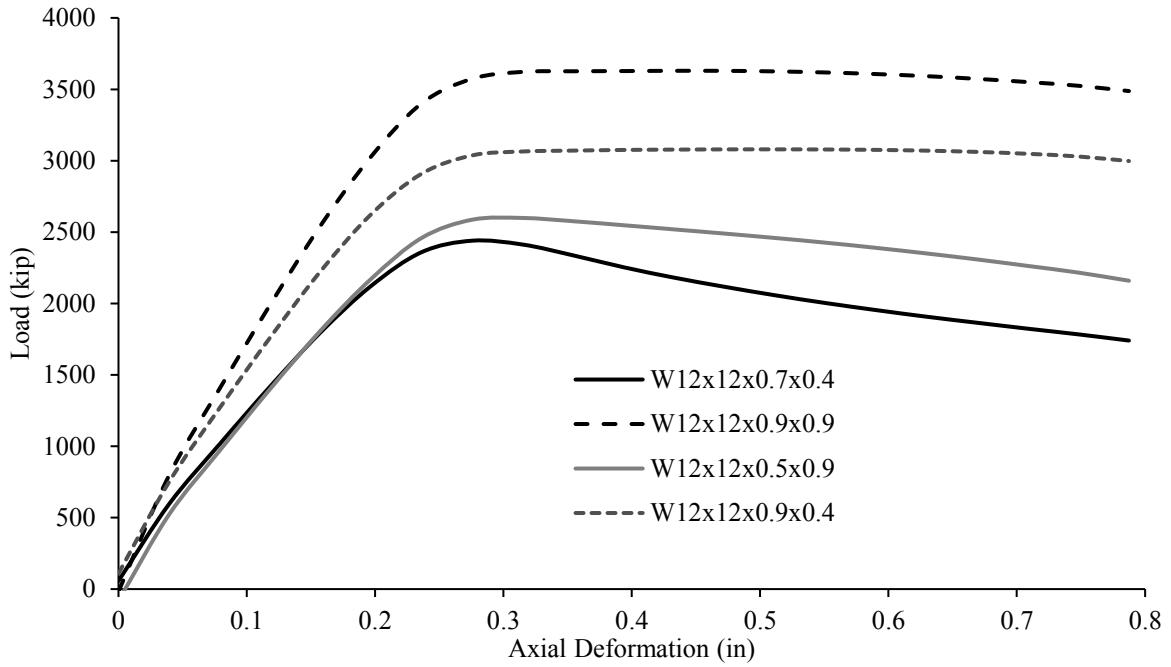


Fig. 47: Axial load vs. axial deformation for W12x12 hot-rolled stub columns of grade 120 ksi

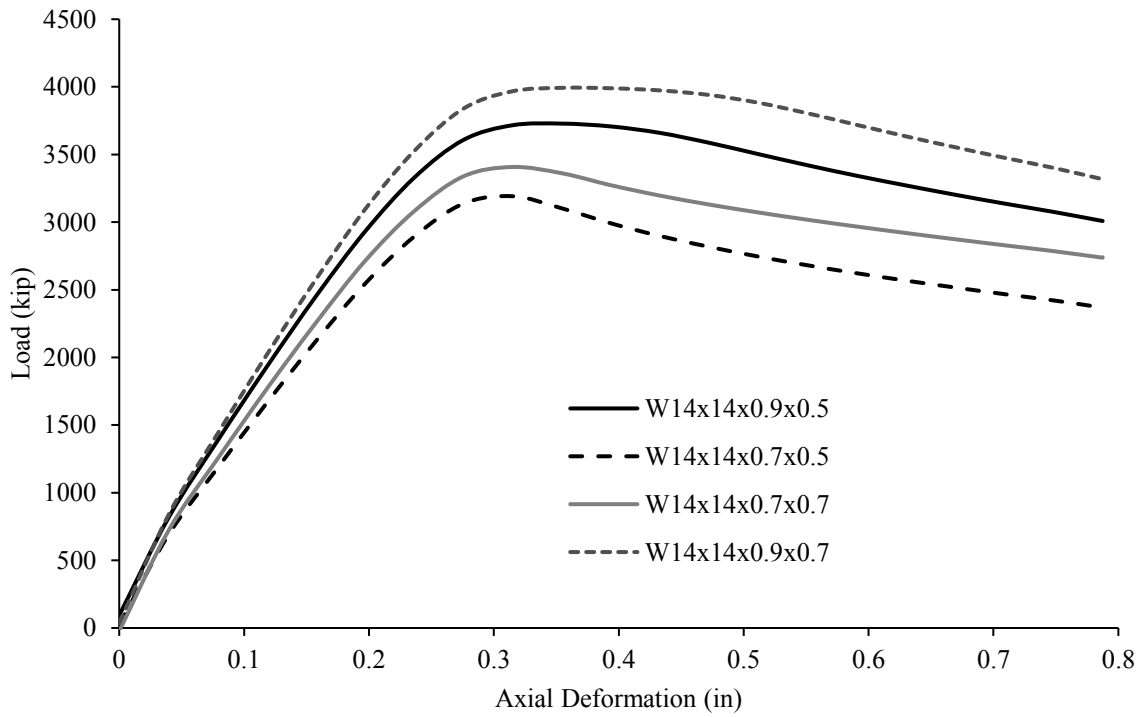


Fig. 48: Axial load vs. axial deformation for W14x14 hot-rolled stub columns of grade 120 ksi

The same observation was found when similar hot-rolled sections were compared with each other by varying the yield strength of the specimen as shown in Fig. 49. It was found that the ultimate load of the specimen increased with an increase in the yield strength of the specimen. This result was consistent across all the hot-rolled sections considered for analysis. This increase in the ultimate load was most dominant in stockier sections and less prevalent in slender sections. This might be due to the impact of yield strength being more predominant in stockier sections. Fig. 49 shows the comparison of axial load vs. axial deformation curves of built-up W12×12 sections with different steel grades. When comparing W12×12×0.9 sections of 100 ksi and 120 ksi, there was a 34% increase in ultimate load. While comparing W12×12×0.4 sections of 100 ksi and 140 ksi, there was only a 5% increase in ultimate load.

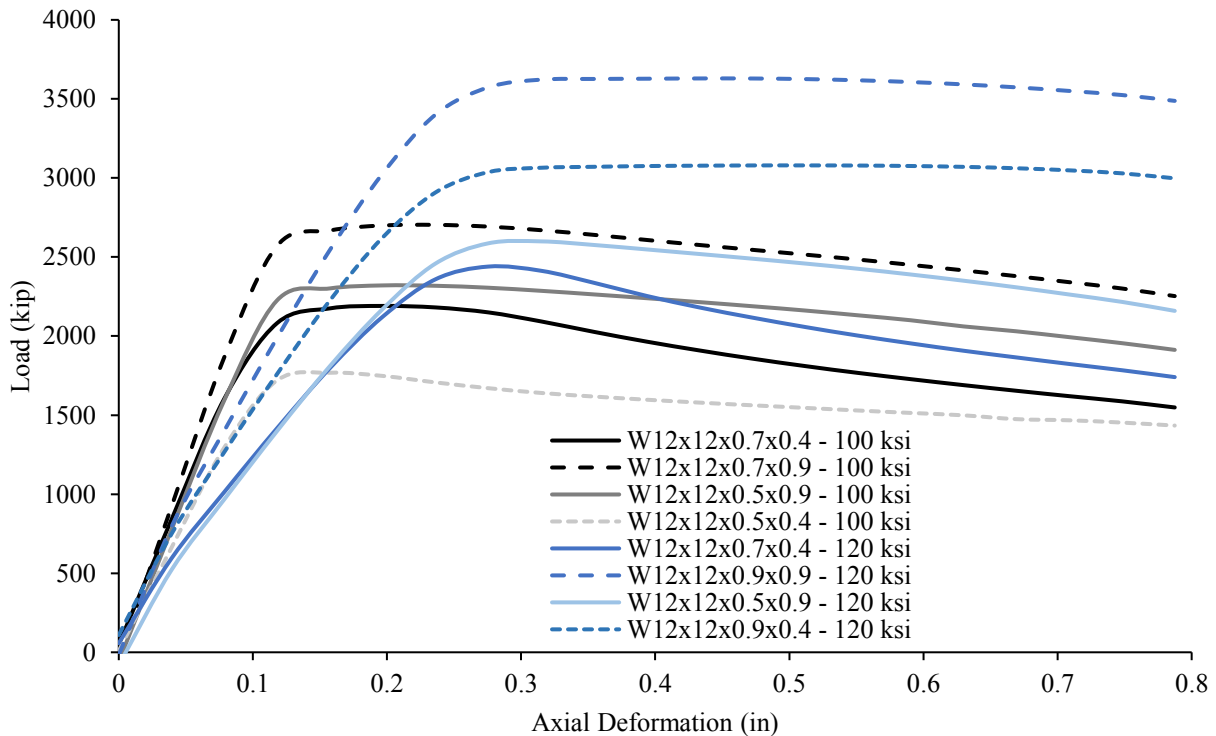


Fig. 49: Comparison of Axial load vs. axial deformation for hot-rolled W12×12 with different steel grades

Similarly, 100 ksi W12×12 sections were compared with each other for hot-rolled and built-up sections. Fig. 50 shows the comparison of axial load vs. axial deformation curves of 100 ksi W12×12 built-up sections with that of hot-rolled sections. The load deformation curves displayed plateau behavior in the case of stockier hot-rolled section, this was not the case with built-up sections. For W12×12×0.7×0.4 section, the hot-rolled section gave higher ultimate load than the same built-up section.

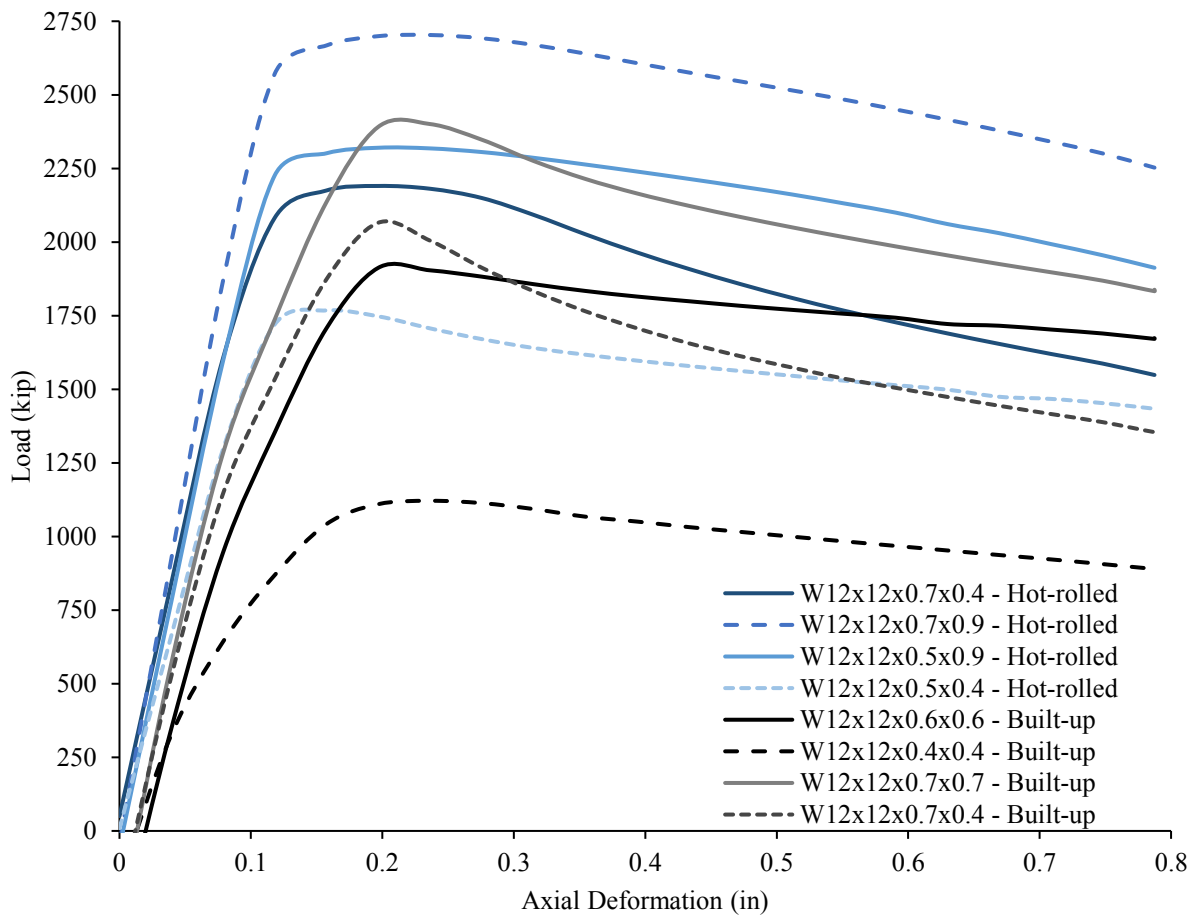


Fig. 50: Comparison of Axial load vs. axial deformation built-up W12×12 sections and hot-rolled W12×12 sections

4.2.4 EVALUATION OF AISC DESIGN EQUATIONS

Table 12 gives a detailed comparison of simulated ultimate load (P_u) and local buckling load (P_L) with AISC nominal compressive strength (P_n) from the FE model for 100 ksi hot-rolled columns. Among the twelve tests, the mean value of P_u/P_n was found to be 1.12 with a coefficient of variation (COV) of 5.2%, and the mean value of P_L/P_n was found to be 1.11 with a COV of 5.5%. Table 13 shows the detailed comparison of P_u and P_L for 120 ksi hot-rolled columns. Among the twelve tests, the mean value of P_u/P_n was found to be 1.04 with a COV of 5.46%, and the mean value of P_L/P_n was found to be 1.03 with a COV of 5.52%. This also means that the design method in the AISC *Specification* can be used in the design of wide flange hot-rolled section columns of grade 100 ksi and 120 ksi.

Table 12: Comparison of AISC compressive strength with ultimate load and local buckling load for 100 ksi hot-rolled columns

Specimen ID (in × in × in × in)	L (in)	P_u (kip)	P_n (kip)	P_u/P_n	P_L (kip)	P_L/P_n
W10×11×1×0.6	31.60	2662.53	2527.11	1.05	2649.09	1.05
W10×11×1×0.3	31.60	2415.16	2235.54	1.08	2400.70	1.07
W10×11×0.5×0.3	31.60	1472.87	1222.53	1.20	1472.03	1.20
W10×11×0.5×0.6	31.60	1766.49	1546.47	1.14	1756.60	1.14
W12×12×0.7×0.4	34.60	2190.46	2036.79	1.08	2175.21	1.07
W12×12×0.7×0.9	34.60	2703.11	2604.32	1.04	2667.82	1.02
W12×12×0.5×0.9	34.60	2320.25	2019.99	1.15	2301.58	1.14
W12×12×0.5×0.4	34.60	1767.79	1505.30	1.17	1767.79	1.17
W14×14×0.9×0.5	39.20	3336.73	3223.62	1.04	3290.23	1.02
W14×14×0.7×0.5	39.20	2898.55	2586.34	1.12	2879.16	1.11
W14×14×0.7×0.3	39.20	2580.39	2179.99	1.18	2561.66	1.18
W14×14×0.7×0.3	39.20	3013.13	2686.43	1.12	2974.30	1.11
Mean				1.115		1.107
COV				5.210%		5.506%

Table 13: Comparison of AISC compressive strength with ultimate load and local buckling load for 120 ksi hot-rolled columns

Specimen ID (in × in × in × in)	L (in)	P _u (kip)	P _n (kip)	P _u / P _n	P _L (kip)	P _L / P _n
W10×11×1×0.6	31.60	3023.34	3080.17	0.98	3011.98	0.98
W10×11×1×0.3	31.60	2727.00	2655.45	1.03	2720.81	1.02
W10×11×0.5×0.3	31.60	1609.69	1384.13	1.16	1609.69	1.16
W10×11×0.5×0.6	31.60	1987.17	1787.37	1.11	1987.17	1.11
W12×12×0.7×0.4	34.60	2439.64	2398.12	1.02	2439.75	1.02
W12×12×0.9×0.9	34.60	3629.33	3629.33	1.00	3621.82	1.00
W12×12×0.5×0.9	34.60	2598.80	2598.80	1.00	2598.80	1.00
W12×12×0.9×0.4	34.60	3079.36	3048.42	1.01	3064.52	1.01
W14×14×0.9×0.5	39.20	3728.24	3661.73	1.02	3728.24	1.02
W14×14×0.7×0.5	39.20	3191.44	2947.81	1.08	3191.44	1.08
W14×14×0.9×0.6	39.20	3407.74	3243.36	1.05	3361.54	1.04
W14×14×0.7×0.6	39.20	3992.65	4104.65	0.97	3992.65	0.97
Mean				1.036		1.034
COV				5.462%		5.522%

The results of the twenty-four FE analyses of built-up sections are summarized in the following figures. The relationship between load ratio (P_u / P_n) and interactive slenderness for hot-rolled members is shown in Fig. 51. Fig. 52 and Fig. 53 show the comparison of P_u from FE analysis and P_n . The load ratio (P_u / P_n) was greater than 1.0 for more than 95% of specimens tested, which demonstrated that the nominal strength predicted by AISC 360 (2016) for HS3 hot-rolled columns was conservative for both 100 ksi and 120 ksi specimens. There was not much difference in the load ratio (P_u / P_n) with low interactive slenderness (≤ 0.5). There was a slight increase in load ratio with an increase in interactive slenderness greater than 0.75. This also suggested that the local buckling equations were slightly more conservative at larger slenderness limits. The diagonal line in Fig. 52 and Fig. 53 shows an exact match between P_u and P_n values. The values above this line indicate a higher P_u value and the values below the line indicate a higher P_n value. The values on the line indicate an exact match between the P_u and P_n values. For 120 ksi specimens, there were more than 50% exact matches and the rest lay above the diagonal line. For 100 ksi specimens, all

the points lay above the line. This indicated that for 100 ksi specimen, FE analysis produced a higher ultimate load than that estimated by AISC 360 (2016).

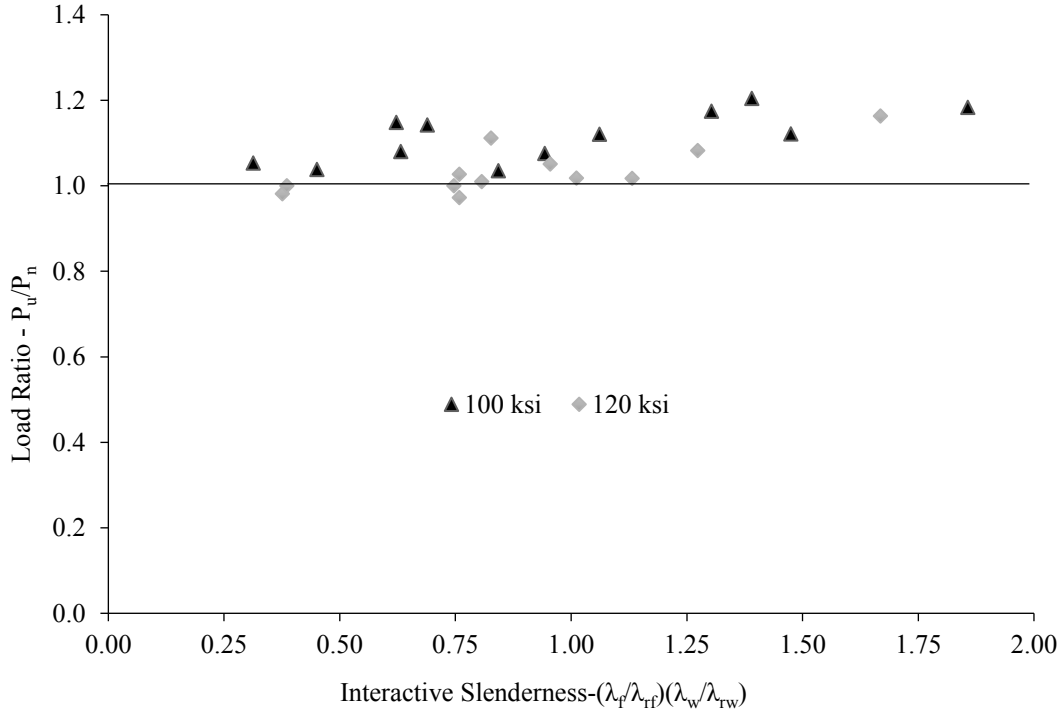


Fig. 51: Comparison of load ratio - P_u/P_n and interactive slenderness - $(\lambda_y/\lambda_{rf})(\lambda_w/\lambda_{rw})$ for hot-rolled members

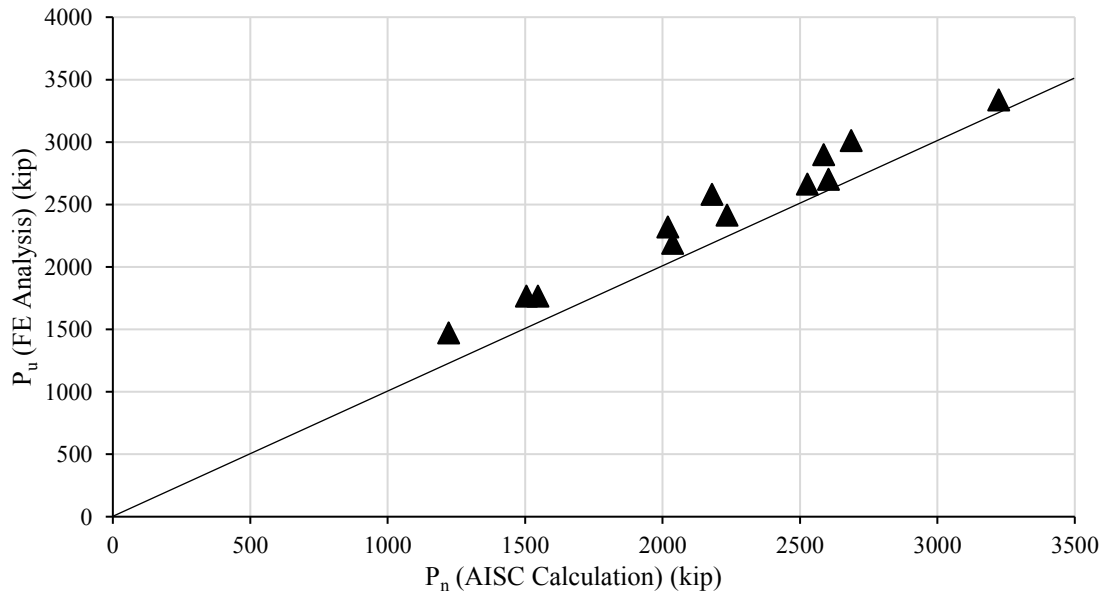


Fig. 52: Comparison of P_u (FE analysis) and P_n (AISC) for 100 ksi hot-rolled members

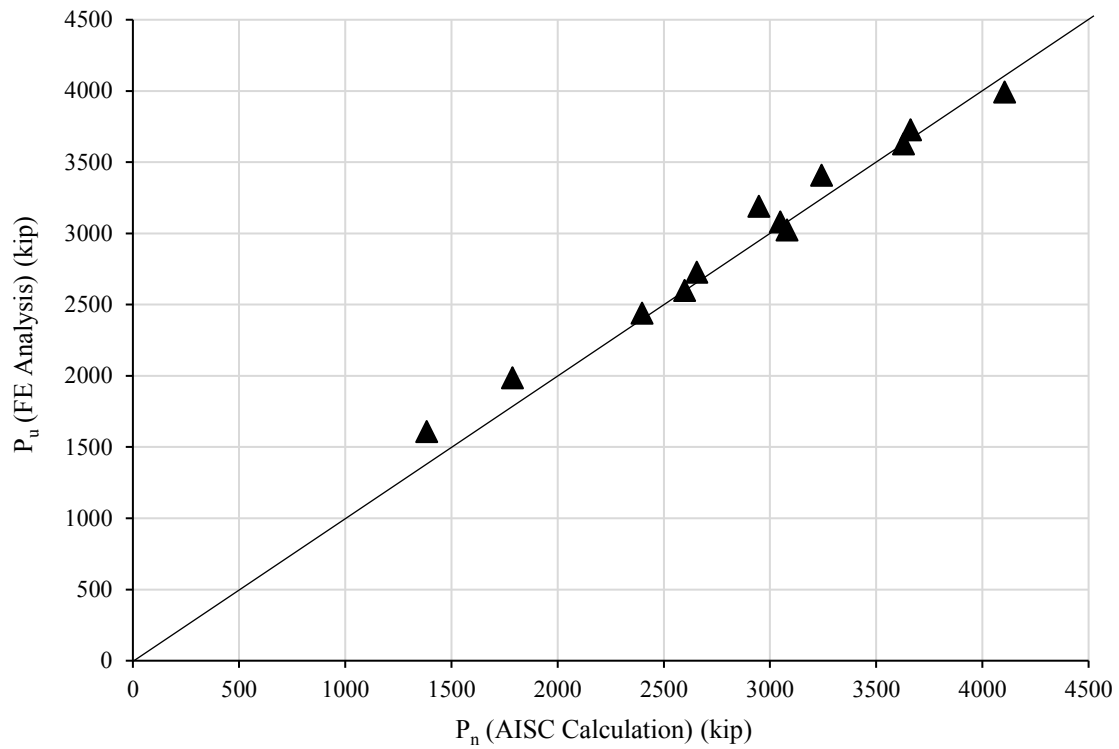


Fig. 53: Comparison of P_u (FE analysis) and P_n (AISC) for 120 ksi hot-rolled members

Fig.54 and Fig.55 represent the plots of load ratio (P_u/P_y) against the interactive slenderness of the column for a hot-rolled specimen of grade 100 ksi and 120 ksi respectively. P_y is the yield load of the specimen obtained from yield stress multiplied by gross cross-sectional area, A_g . From the graphs in Fig.54 and Fig.55, as the interactive slenderness increases, the load ratio (P_u/P_y) of the hot-rolled column was constant. This is probably due to the values of interactive slenderness being less than two. The load ratio (P_u/P_y) is also less than 1.0 for nearly all specimens. This shows that yielding across the entire cross-section has not occurred. This is to be expected in local buckling cases.

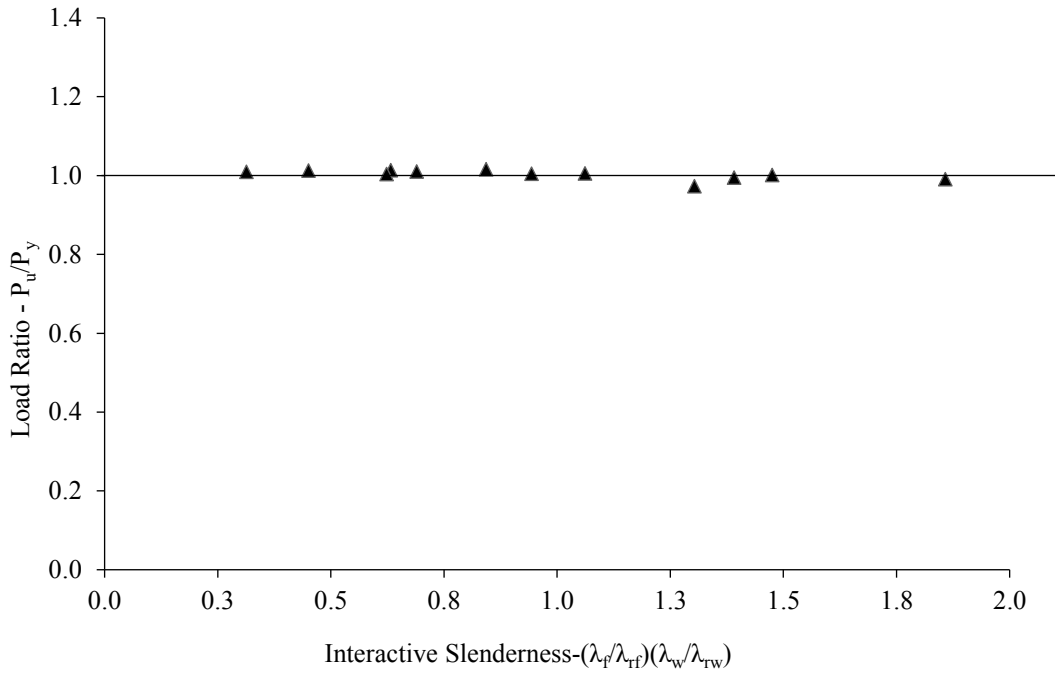


Fig. 54: Comparison of load ratio and interactive slenderness for 100 ksi hot-rolled members

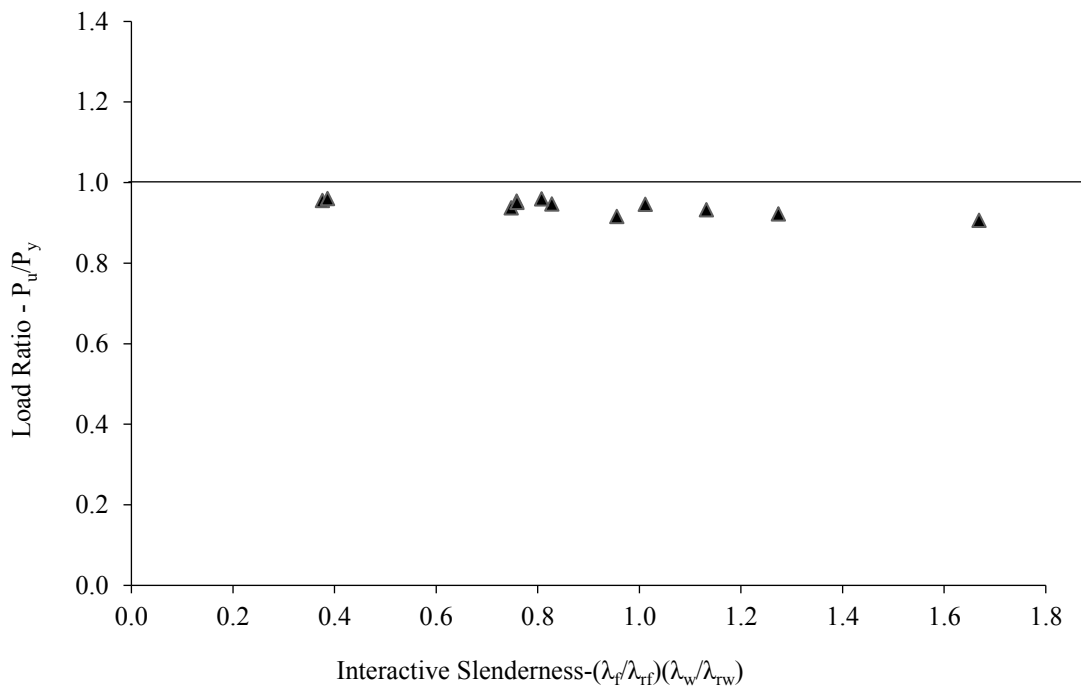


Fig. 55: Comparison of load ratio and interactive slenderness for 120 ksi hot-rolled members

4.2 INTERACTIVE BUCKLING OF BUILT-UP W SHAPES

In columns with high width-to-thickness ratios and intermediate member slenderness (global slenderness between 40 to 80), local buckling is observed. But the mode of failure is still flexural buckling. In such columns, the local buckling will instigate the process of flexural buckling. This mode of buckling is called interactive buckling. Interactive buckling mode may be observed in columns with slender elements (Cao et al., 2021). The most important parameters that affected the compressive strength are the yield strength, section slenderness, member slenderness, and load eccentricity. Since the study of interactive buckling is important, the parameters of section slenderness and load eccentricity were kept constant. W14×14×0.4 column was selected to study the interactive buckling phenomenon as it was a slender column with both flange and flange elements being slender. A parametric study was done to study the influence of member slenderness on the interactive buckling behavior in 120 ksi HS3 built-up wide flange columns. Table 14 shows the list of specimens that were chosen for the study of interactive buckling in columns. The validation of the modeling approach of built-up wide flange column subjected to interactive buckling is given in Chapter 3 of the report. The modeling approach, material properties, boundary conditions, and initial geometrical imperfections were the same as that of the I5 built-up column in Chapter 3. Chapter 3, Appendix A, and Appendix B give more information on the procedure and calculation of various parameters in the FE model.

A W14×14×0.4S62.5 column from Table 14 had a width (B) of 13.8 in., depth (H) of 13.8 in., thickness of both the web and the flange of 0.4 in. with member slenderness (λ) of 62.5. Member slenderness is defined as the ratio of effective length of the column to its weak axis radius of gyration. It is given by KL/r where K is the effective length factor (can be obtained from Table C-A-7.1 of AISC 360 (2016)), L is the lateral unbraced length of the column, and r is the radius of

gyration about the weak axis. Appendix C gives more information on AISC member slenderness limits. These columns closely represent the dimensions of hot-rolled shape of W14×109 section. But the section slenderness of both web and flange were larger than the AISC limiting slenderness limits. This meant that all the columns in Table 14 were made of slender elements. The length of the column was varied hence varying the member slenderness.

Table 14: List of specimens for study of interactive buckling of wide flange built-up columns

Specimen ID (in × in × in Sλ)	L (in)	λ	B (in)	H (in)	t_r (in)	t_w (in)
W14×14×0.4S62.5	204.28	62.50	13.78	13.78	0.39	0.39
W14×14×0.4S75	245.14	75.00	13.78	13.78	0.39	0.39
W14×14×0.4S87.5	285.99	87.50	13.78	13.78	0.39	0.39
W14×14×0.4S100	326.85	100.00	13.78	13.78	0.39	0.39
W14×14×0.4S112.5	367.70	112.50	13.78	13.78	0.39	0.39

Five different simulations were performed to obtain the ultimate load of the specimen. Cao et al. (2020) residual stress model was applied to all five simulations alongside the initial geometric imperfections obtained from Eigen Buckling analysis in ABAQUS. Mode 1 in Eigen Buckling analysis represented the global buckling mode as shown in Fig. 56. Mode 2 represented the local buckling mode as shown in Fig. 57. Mode 1 was applied a global imperfection of 0.25 in. and mode 2 was applied a local imperfection of 1/16 in. Both the modes were superimposed to obtain the interactive buckling mode in ABAQUS. A conservative value for global imperfection was obtained from ASTM A6 (2019) as 0.383 in. for W14×14×0.4S112.5 specimen. This global imperfection corresponds with L/960. The results from this magnitude of imperfection were then compared with the results from a global imperfection of 0.25 in. It was found that there was only 3.5% drop in the ultimate load. Appendix B gives more information on the allowances of initial

geometric imperfection as described in ASTM A6 (2019). Fig. 58 shows the interactive buckling mode in one of the test specimens. Both global and local buckling can be observed in Fig. 58.

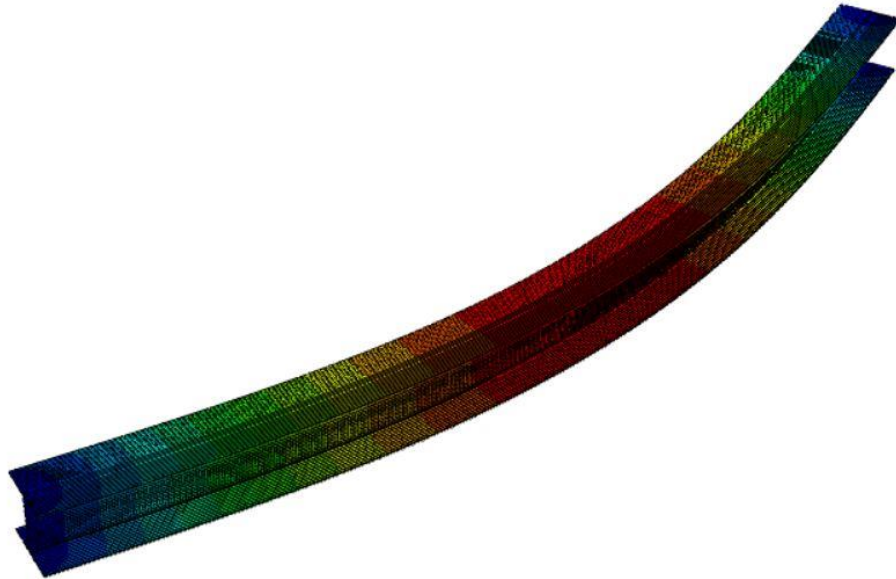


Fig. 56: Mode 1 of eigen buckling analysis for interactive buckling specimens

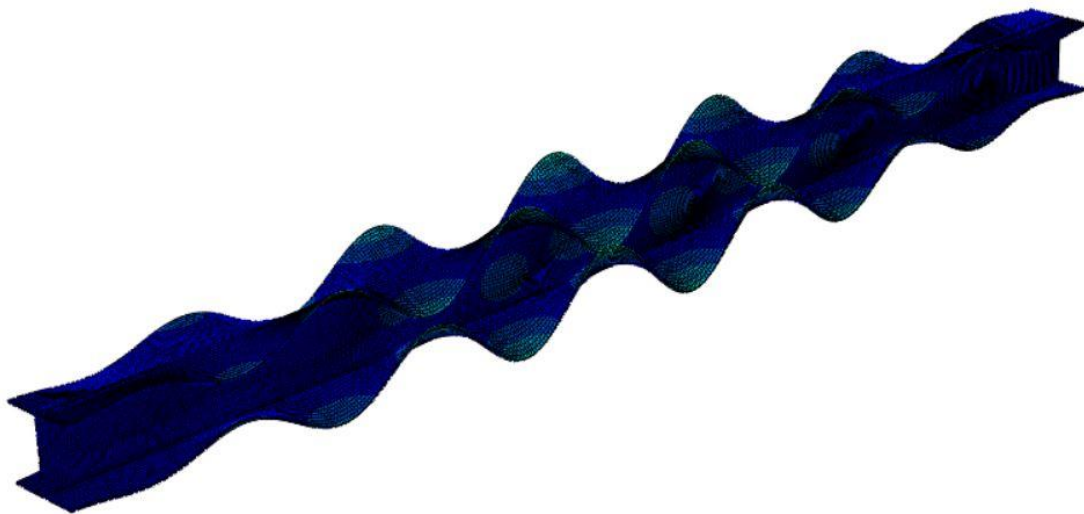


Fig. 57: Mode 2 of eigen buckling analysis for interactive buckling specimens

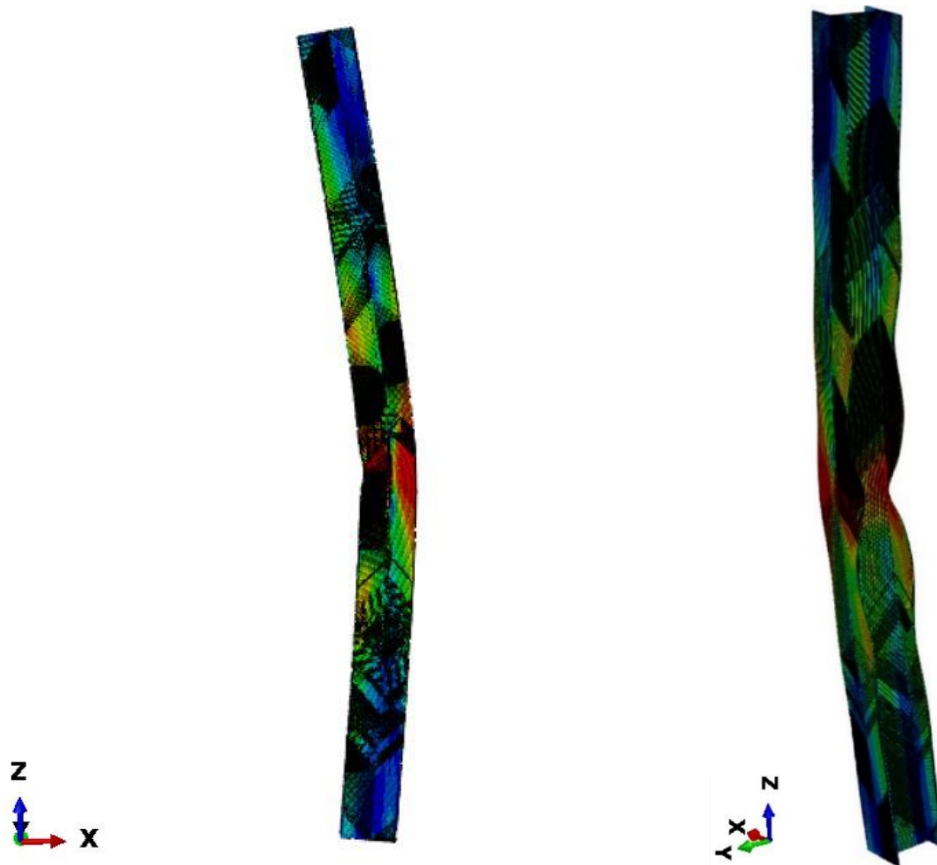


Fig. 58: Interactive buckling mode in one of the column specimens: a. Global buckling (left) b. Local buckling (right)

All five specimens analyzed using ABAQUS failed by interactive buckling mode. This is probably due to the following factors:

1. All the specimens considered had slender flange and slender web with low section slenderness.
2. The length of the specimen considered was considerably larger than the stub column length as given by the SSRC formula.
3. Both global buckling mode and local buckling mode were considered for analysis.

Shorter sections had higher ultimate load and when the member slenderness was increased (length increased), there was a decrease in the ultimate load. Fig. 59 shows the comparison of axial load with axial deformation for W14×14×0.4 built-up columns of grade 120 ksi. It can be seen from Fig. 59 and Fig. 60 that the shorter sections exhibited increased ultimate load.

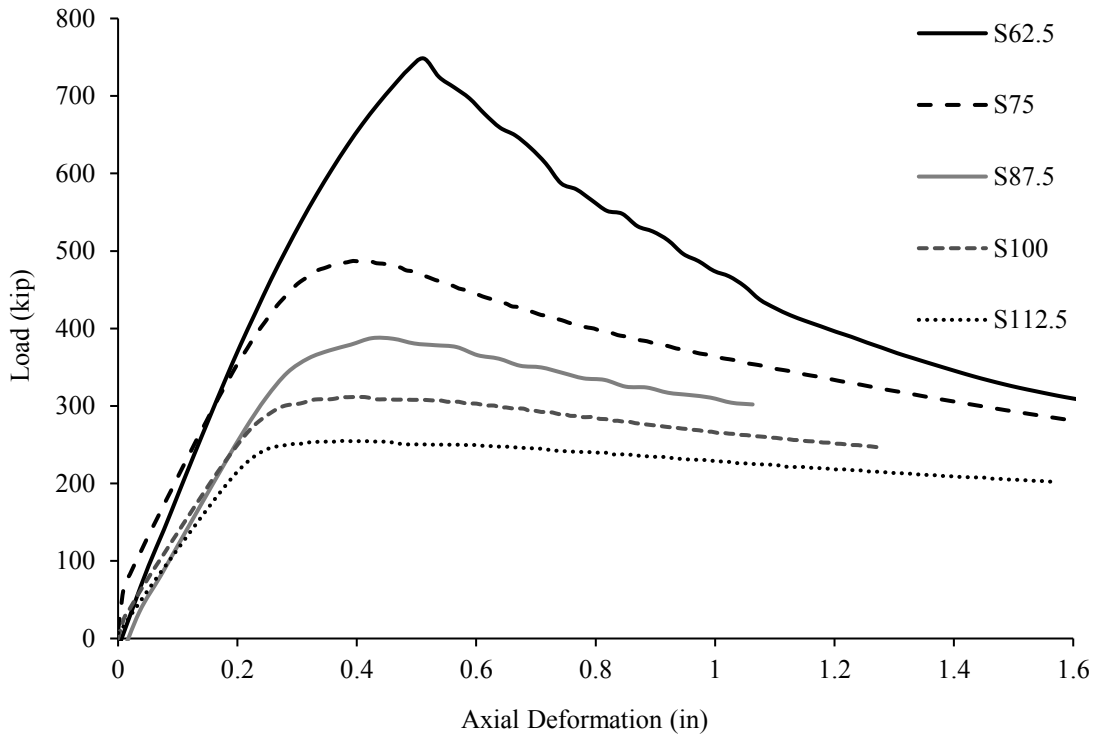


Fig. 59: Axial load vs. axial deformation for W14×14×0.4 built-up columns of grade 120 ksi

Fig. 60 also shows the AISC member slenderness limit alongside comparing the axial load with member slenderness for W14×14×0.4 built-up columns of grade 120 ksi. More information on AISC member slenderness limit is available in Appendix C of the report.

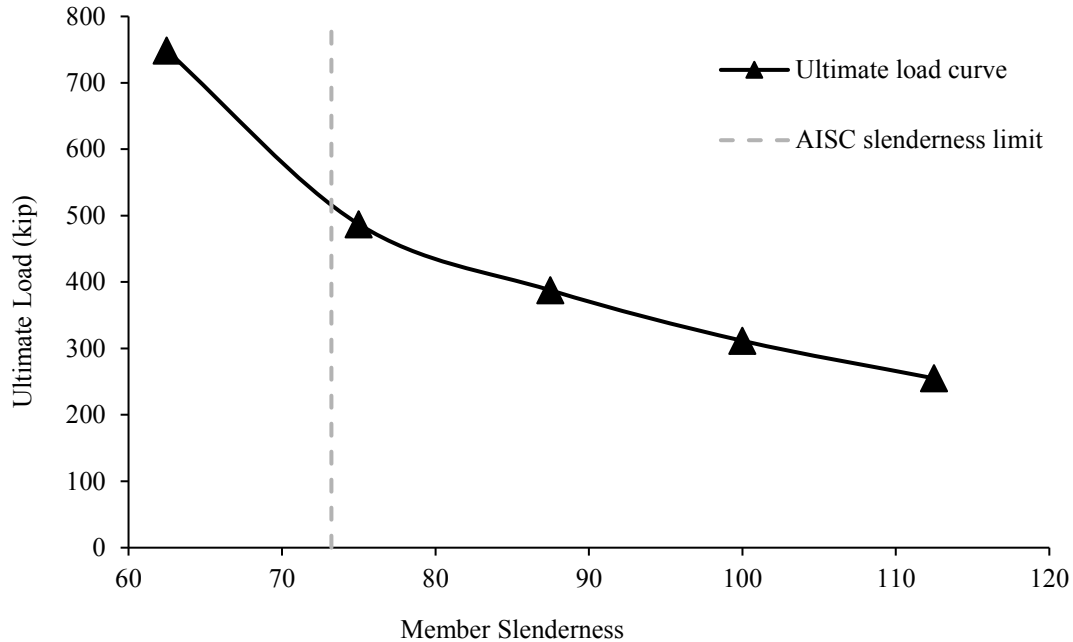


Fig. 60: Ultimate load vs member slenderness for W14x14x4 column

AISC 360 (2016) does not consider interactive buckling into account while designing compression members. The applicability of local buckling equations and flexural buckling equations from AISC 360 (2016) to calculate the nominal compressive strength of the column (P_n) is evaluated. Table 15 gives a detailed comparison of simulated ultimate load (P_u) with AISC nominal compressive strength (P_n) from the FE model for 120 ksi built-up columns. Among the five tests conducted, the mean value of P_u/P_n was found to be 0.814 with a coefficient of variation (COV) of 10.35%. A plot of P_u v/s P_n was plotted to compare the AISC predicted value and the value obtained from ABAQUS as shown in Fig. 61. The diagonal line indicated a perfect match between P_u and P_n . It was seen that all points fall below the solid line in Fig. 61. This meant that the AISC equation overpredicted the nominal strength of these columns. It can also be seen from Table 15 that for column W14x14x0.4S62.5, there was only 4% deviation between P_u and P_n . It can also be seen from Fig. 60 that the same column fell below the AISC member slenderness limit. This meant that

AISC design equations predicted a more accurate ultimate load below the member slender limit for 120 ksi built-up columns. But this needs to be backed up with more testing data.

Table 15: Comparison of AISC compressive strength with ultimate load for 120 ksi built-up columns

Specimen ID (in × in × in Sλ)	L (in)	P _u (kip)	P _n (kip)	P _u / P _n
W14×14×0.4S62.5	204.28	748.47	778.16	0.96
W14×14×0.4S75	245.14	487.15	639.21	0.76
W14×14×0.4S87.5	285.99	387.53	506.25	0.77
W14×14×0.4S100	326.85	311.55	401.09	0.78
W14×14×0.4S112.5	367.70	254.93	316.91	0.80
Mean				0.814
COV				10.346%

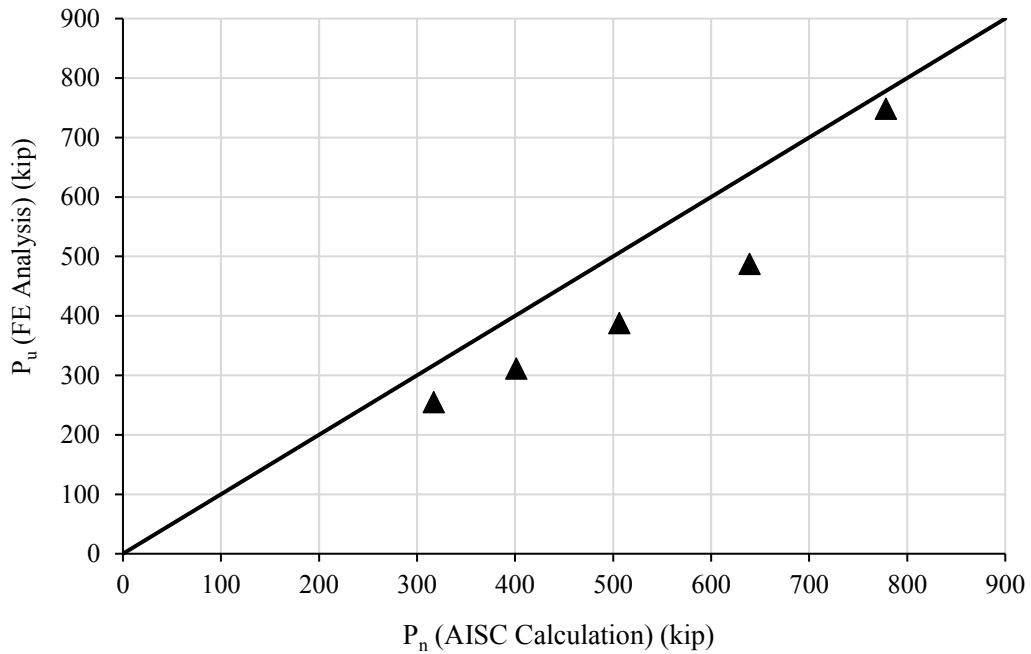


Fig. 61: Comparison of P_u (FE analysis) and P_n (AISC) for 120 ksi built-up columns

5.0 CONCLUSIONS AND FUTURE WORK

FE models generated in ABAQUS were validated through comparison with five HS3 stub columns from the experimental studies of Shi et al. (2015), Cao et al. (2020; 2021), and Sun et al. (2019). A parametric study was conducted with this FE model, to study the local buckling behavior of HS3 built-up and hot-rolled stub columns and interactive buckling behavior of HS3 built-up columns. This included twenty-four simulations each for study of local buckling of built-up and hot-rolled stub columns and five simulations for study of interactive buckling. The parameters of section slenderness, member slenderness, and yield strength and their impact on the ultimate load capacity of the column were studied. The ultimate load capacity and local buckling load for the wide flange stub columns of grade 100 ksi, 120 ksi, and 140 ksi were established. The numerical results obtained were compared with the design method in the *AISC Specification (2016)* to obtain the nominal strength of the column. These strengths are based on steels with yield strengths less than 65 ksi, so the applicability of this method for higher strength steels was studied.

The following are the conclusions of this research:

- The local buckling failure was very abundant in slender members, and it did not take place at the center of the column for most of the FE models. Local buckling failure also did not take place in stockier sections that had only non-slender elements. The first eigenvalue buckling mode dictated the buckling shape of the column which was in turn dependent upon the end conditions, member, and section slenderness of the column. As, the classification of these columns was purely based on limiting slenderness limits (λ_r) for CMS, this meant that these limits (λ_r) given in the *AISC Specification* were valid and can

be used for the classification of both built-up and hot-rolled HS3 steel columns of grade 100 ksi, 120 ksi, and 140 ksi.

- The ultimate load capacity of the stub columns decreased with an increase in section slenderness for both built-up and hot-rolled stub columns. This trend was almost linear for both built-up and hot-rolled shapes. The observation was very consistent across the grades of 100 ksi, 120 ksi, and 140 ksi column specimens.
- The ultimate load capacity of the columns increased with an increase in yield strength of the column for both built-up and hot-rolled stub columns. This trend was also linear for both built-up and hot-rolled shapes. The observation was also very consistent across the grades of 100 ksi, 120 ksi, and 140 ksi column specimens.
- Hot-rolled sections exhibited higher ultimate load capacity than their built-up counterparts. This was due to the values of compressive and tensile residual stresses in built-up shapes being double that of hot-rolled counterparts. This was primarily due to the difference in their residual stress models.
- For 100 ksi HS3 built-up stub columns, the design method in the AISC (2016) *Specification* nearly predicted the nominal strength of the column with a coefficient of variation (COV) of 2.7%. For 140 ksi HS3 built-up stub columns, the design method in the AISC (2016) *Specification* predicted the nominal strength with a COV of 5.0%. This means that the design method in the AISC (2016) *Specification* can be used in the design of wide flange built-up section columns of grade 100 ksi and 140 ksi stub columns.
- For 100 ksi HS3 hot-rolled stub columns, the design method in the AISC (2016) *Specification* nearly predicted the nominal strength of the column with a COV of 5.2%. For 120 ksi HS3 hot-rolled stub columns, the design method in the AISC (2016)

Specification predicted the nominal strength with a COV of 5.5%. This means that the design method in the AISC *Specification* can be used in the design of wide flange hot-rolled section columns of grade 100 ksi and 120 ksi stub columns.

- The ultimate load capacity of the columns decreased with an increase in member slenderness and the length of the column for 120 ksi built-up sections. This means that the shorter sections (columns that had shorter lengths) had higher ultimate load and when the member slenderness was increased (length increased), there was a decrease in the ultimate load for 120 ksi built-up sections.
- Although the AISC (2016) *Specification* does not consider interactive buckling into account, during the interactive buckling study - for sections below the member slenderness limit, the design method in the AISC *Specification* predicted the nominal strength of the column with a mean deviation of 3.8%. This meant that the AISC slenderness limit for CMS given in the AISC *Specification* was valid and can be used for the classification of built-up HS3 steel columns of grade 120 ksi.
- For 120 ksi HS3 built-up columns that were considered for the study of interactive buckling, the design method in the AISC (2016) *Specification* predicted the nominal strength of the column with a mean of 0.814 and coefficient of variation (COV) of 10.35%. This means that the design method in the AISC (2016) *Specification* slightly overestimated the ultimate load capacity of columns.

Additional studies are needed to ensure the applicability of the AISC *Specification* for a full range of member sizes, member length, and steel grades.

5.1 FUTURE WORK

This work was conducted in an effort to advance the use of HS3 and understand its implications on the design by drawing on existing experimental data. However, there were some assumptions that had to be made that needed to be verified with experimental testing before more definitive conclusions can be made. Several of these limitations and assumptions are discussed here which can extend the scope of this research:

- The analytical results for local buckling obtained through ABAQUS need to be confirmed with an experimental study. The applicability of the column design method for local buckling in the AISC (2016) *Specification* will need to be backed with experimental data so that it can be used for the design of HS3 columns. This is particularly important since rolled shapes are not typically produced in 100ksi and 120 ksi grades, so there is a lack of experimental testing on this material strength and shape.
- A comprehensive experimental study is required to confirm the applicability of current residual stress models for HS3 hot-rolled sections and their impact on the ultimate load capacity.
- Although the AISC (2016) *Specification* does not consider interactive buckling into account, there is still a need to study them. Additional studies are needed to further examine the interactive buckling behavior in HS3 columns. The amount of initial geometric imperfections contributing to interactive buckling need to be analyzed so that such behavior can be avoided during the design process.

6.0 REFERENCES

- AASHTO. 2017. *AASHTO LRFD Bridge Design Specifications*. Washington, D.C: AASHTO.
- ABAQUS. 2018. *Simulia ABAQUS*. Boston, Mass.: Dassault Systemes.
- AISC. 2016. *Specification for Structural Steel Buildings*. Chicago: AISC.
- Akhtar, F A, and R Chicchi. 2021. "Numerical investigation of the flexural buckling of high strength steel wide flange columns." *Proceedings of the Annual Stability Conference*. Louisville: Structural Stability Research Council.
- ASTM. 2019. *ASTM A6 / A6M - 19: Standard Specification for General Requirements for Rolled Structural Steel Bars, Plates, Shapes, and Sheet Piling*. American Society of Testing and Materials.
- Ban, H, and G Shi. 2018. "A Review of Research on High-Strength Steel Structures." *Proceedings of the Institution of Civil Engineers: Structures and Buildings* 625-641.
- Ban, H, G Shi, Y Shi, and M A Bradford. 2013. "Experimental Investigation of the Overall Buckling Behaviour of 960 MPa High Strength Steel Columns." *Journal of Constructional Steel Research* 256-266.
- Ban, H, G Shi, Y Shi, and Y Wang. 2012. "Overall Buckling Behavior of 460 MPa High Strength Steel Columns: Experimental Investigation and Design Method." *Journal of Constructional Steel Research* 140-150.
- Beg, D, and L Hladnik. 1996. "Slenderness Limit of Class 3 I Cross-Sections Made of High Strength Steel." *Journal of Constructional Steel Research* 201-217.
- Cao, X, G Zhao, Z Kong, H Shen, C Cheng, Z Chen, and S E Kim. 2020. "Experimental Study on Local Buckling of 800 MPa HSS Welded I-Section Columns under Axial Compression." *Thin-Walled Structures* 155 (10).
- Cao, X, R Zhong, Y Xu, C Cheng, S Liu, Z Chen, S E Kim, and Z Kong. 2021. "Local–Overall Interactive Buckling Behaviour of 800 MPa High Strength Steel Welded H-Section Members under Axial Compression." *Thin-Walled Structures* 164 (7).
- Cao, X, R Zhong, Y Xu, C Cheng, S Liu, Z Chen, S E Kim, and Z Kong. 2021. "Local–Overall Interactive Buckling Behaviour of 800 MPa High Strength Steel Welded H-Section Members under Axial Compression." (Thin-Walled Structures) 164 (7).
- Cao, X, L Gu, Z Kong, G Zhao, M Wang, S E Kim, D Jia, and C Ma. 2019. "Local Buckling of 800 MPa High Strength Steel Welded T-Section Columns under Axial Compression." *Engineering Structures* 194 (9).
- Chinese, Steel. 2017. *GB 50017-2017 Code for Design of Steel Structures (English Version)*. Code of China.

- Eurocode, BSI. 2007. *EN 1993-1-12: Eurocode3: Design of Steel Structures: Part 1-12: High Strength Steel*.
- Fahnestock, L, E Brannon, and G A Rassati. 2019. "Annotated Bibliography of Related Work." (AISC Ad Hoc Task Group Report on High Strength Steel) 1 (1).
- Farahi, M, A Heidarpour, X L Zhao, and R Al-Mahaidi. 2017. "Effect of Ultra-High Strength Steel on Mitigation of Non-Ductile Yielding of Concrete-Filled Double Skin Columns." *Construction and Building Materials* 147 (8).
- Galambos, T V, and Ketter R L. 1959. "Columns under combined bending and thrust." (J Eng Mech Div) 1 (85).
- Galambos, T V. 1968. *Structural Members and Frames*. Englewood Cliffs, N.J.: Prentice-Hall Inc.
- Hu, P C, E E Lundquist, and S B Batdorf. 1946. *Effect of Small Deviations from Flatness of Effective Width and Buckling of Plates and Compression*. TN: National Advisory Committee for Aeronautics.
- Javidan, F, A Heidarpour, X L Zhao, and J Minkkinen. 2016. "Application of High Strength and Ultra-High Strength Steel Tubes in Long Hybrid Compressive Members: Experimental and Numerical Investigation." *Thin-Walled Structures* 102 (5).
- Nassirnia, M, A Heidarpour, X L Zhao, and J Minkkinen. 2016. "Innovative Hollow Columns Comprising Corrugated Plates and Ultra High-Strength Steel Tubes." *Thin-Walled Structures* 101 (04).
- Rasmussen, K J, and G J Hancock. 1992. "Plate Slenderness Limits for High Strength Steel Sections." *Journal of Constructional Steel Research* 23 (3).
- Schillo, N, A Taras, and M Feldmann. 2018. "Assessing the Reliability of Local Buckling of Plates for Mild and High Strength Steels." *Journal of Constructional Steel Research* 142 (3).
- Schillo, N, and M Feldmann. 2018. "Interaction of Local and Global Buckling of Box Sections Made of High Strength Steel." *Thin-Walled Structures* 128 (7).
- Seif, M, and B Schafer. 2014. "Design of Locally Slender Structural Steel Columns." *Journal of Structural Engineering* 140 (4).
- Shi, G, C C Lin, Y Q Wang, Y J Shi, and Z Liu. 2011. "Finite Element Analysis on the Local Buckling Behavior of High Strength Steel Members under Axial Compression." *Advanced Materials Research* 1477 (82).
- Shi, G, F Hu, and Y Shi. 2014. "Recent Research Advances of High Strength Steel Structures and Codification of Design Specification in China." *International Journal of Steel Structures* 14 (4).
- Shi, G, K Xu, H Ban, and C Lin. 2016. "Local Buckling Behavior of Welded Stub Columns with Normal and High Strength Steels." *Journal of Constructional Steel Research* 119 (3).

- Shi, G, W Zhou, and C Lin. 2015. "Experimental Investigation on the Local Buckling Behavior of 960 MPa High Strength Steel Welded Section Stub Column." *Advances in Structural Engineering* 18 (3).
- Shi, G, W Zhou, Y Bai, and C Lin. 2014. "Local Buckling of 460 MPa High Strength Steel Welded Section Stub Columns under Axial Compression." *Journal of Constructional Steel Research* 100 (1).
- Shi, G, Z Zhang, L Zhou, L Yang, and W Zhou. 2020. "Experimental and Numerical Investigation on Local–Overall Interactive Buckling Behavior of Welded I-Section Steel Columns." *Thin-Walled Structures* 151 (6).
- SIMULIA. 2020. *ABAQUS*. Johnston, RI: Dassault Systemes.
- SSRC. 2010. *Guide to Stability Design Criteria for Metal Structures*. Hoboken, NJ: John Wiley and Sons.
- Su, A, Y Sun, Y Liang, and O Zhao. 2021. "Membrane Residual Stresses and Local Buckling of S960 Ultra-High Strength Steel Welded I-Section Stub Columns." *Thin-Walled Structures* 161 (4).
- Sun, Y, Y Liang, and O Zhao. 2019. "Testing, Numerical Modelling and Design of S690 High Strength Steel Welded I-Section Stub Columns." *Journal of Constructional Steel Research* 159 (8).
- Sunthorn, S., and R. Kittiphath. "The effect on rolling mill of waviness in hot rolled steel." *Int. J. Mater. Metall. Eng* (2014).
- Systemes, Dassault. 2014. *ABAQUS/CAE User's Manual, Version 6.14*. Dassault Systemes Simulia Corp.
- Tillman, S C, and A F Williams. 1989. "Buckling under Compression of Simple and Multicell Plate Columns." *Thin-Walled Structures* 8 (1).
- Usami, T, and Y Fukumoto. 1982. "Local and Overall Buckling of Welded Box Columns." *ASCE J Struct* 108 (3).
- Usami, T, and Y Fukumoto. 1984. "Welded Box Compression Members." *Journal of Structural Engineering* 110 (10).
- Yang, L, G Shi, M Zhao, and W Zhou. 2017. "Research on interactive buckling behavior of welded steel box-section columns." *Thin-Walled Structures* 115 (6).

APPENDIX A – RESIDUAL STRESSES

This section gives brief information on the calculation of residual stresses for a handful of built-up shapes and hot-rolled W shapes used in the benchmark study and parametric study. This section also shows the applied residual stresses in W shapes for all remaining sections in the parametric study.

A.1 CALCULATION OF RESIDUAL STRESSES

A.1.1 Calculation of Residual Stresses for 140 ksi built-up specimen:

This section gives brief information on the application of Ban et al. (2013) residual stress model on the I1 specimen used in the benchmark study. The dimensions of the I1 specimen are given in metric units.

$$B := 210 \text{ mm} \quad h_0 := 184.4 \text{ mm} \quad b_f := 98.1 \text{ mm} \quad t_e := 6 \text{ mm} \quad t_f := 13.93 \text{ mm}$$

$$t_w := 13.88 \text{ mm}$$

Empirical formula, units in mm and MPa

$$\sigma_{frc} := 100 \text{ MPa} - 930 \text{ MPa} \cdot \left(\frac{1}{\frac{b_f}{t_f}} \right) - 2205 \text{ MPa} \cdot \left(\frac{1 \text{ mm}}{t_f} \right) \quad (\text{A1-1})$$

$$\sigma_{wrc} := 20 \text{ MPa} - 2200 \text{ MPa} \cdot \left(\frac{1}{\frac{h_0}{t_w}} \right) - 660 \text{ MPa} \cdot \left(\frac{1 \text{ mm}}{t_w} \right) \quad (\text{A1-2})$$

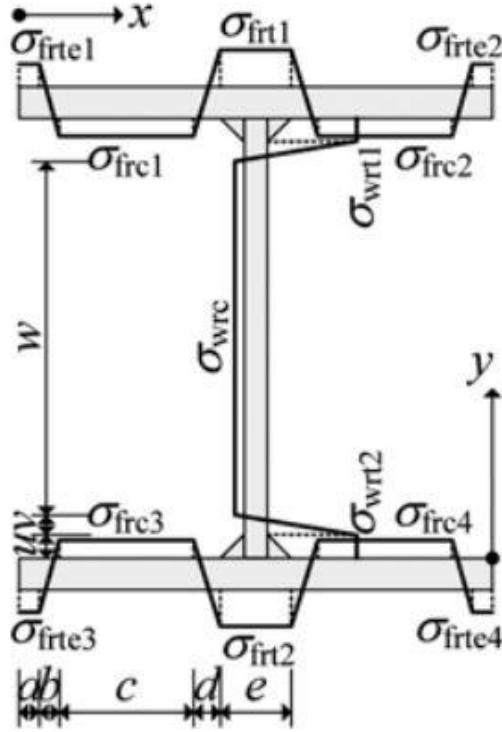


Fig. A 1: Ban et al. (2013) residual stress model

$$-960 \text{ MPa} \leq \sigma_{frc} \leq -96 \text{ MPa} \quad \text{and} \quad -960 \text{ MPa} \leq \sigma_{wrc} \leq -96 \text{ MPa}$$

$$\sigma_{frt} := 460 \text{ MPa} \quad \sigma_{wrt} := 460 \text{ MPa} \quad \sigma_{frte} := 288 \text{ MPa}$$

$$a := 0.1 (b_f - t_e) \quad a = 9.21 \text{ mm}$$

$$b := 0.1 (b_f - t_e) \quad b = 9.21 \text{ mm}$$

$$e := t_w + 2 t_e \quad e = 25.88 \text{ mm} \quad z := \frac{B - e}{2} - a - b \quad z = 73.64 \text{ mm}$$

$$z = c + d \quad \sigma_{frc} = -190.35 \text{ MPa} \quad \sigma_{wrc} = -193.147 \text{ MPa}$$

Applying equilibrium conditions,

$$\sigma_{frte} \cdot a + 0.25 \cdot b \cdot \sigma_{frte} + 0.25 \cdot b \cdot \sigma_{frc} + \sigma_{frc} \cdot c + 0.25 \cdot \sigma_{frc} + 0.25 \cdot d \cdot \sigma_{frt} + \sigma_{frt} \cdot \frac{e}{2} = 0$$

$$c + d = 73.64 \text{ mm}$$

$$190.35 \cdot c - 67.4125 d = 8829.719125 \text{ mm}$$

$$c = 53.514 \text{ mm}$$

$$d = 20.126 \text{ mm}$$

$$u := t_w$$

$$2(u+v)+w = h_0$$

Applying equilibrium conditions,

$$\sigma_{wrt} \cdot u + 0.25 \cdot v \cdot \sigma_{wrt} + 0.25 \cdot v \cdot \sigma_{wrc} + \sigma_{wrc} \cdot \frac{w}{2} = 0$$

$$2 v + w = 156.64 \text{ mm}$$

$$66.713 v - 96.574 w = -6384.8 \text{ mm}$$

$$v = 33.643 \text{ mm}$$

$$w = 89.354 \text{ mm}$$

A.1.2 Calculation of Residual Stresses for 120 ksi built-up specimen:

This section gives brief information on the application of Cao et al. (2020) residual stress model on the I3 specimen used in the benchmark study. The dimensions of the I3 specimen are given in metric units.

$$B := 309.3 \text{ mm} \quad H := 244 \text{ mm} \quad b_f := 150.995 \text{ mm} \quad h_0 := 229.3 \text{ mm}$$

$$t_f := 7.35 \text{ mm} \quad t_w := 7.31 \text{ mm} \quad t_e := 6 \text{ mm} \quad \text{Empirical formula, units in mm and MPa}$$

$$\frac{b_f}{t_f} = 20.544 > 6 \quad \text{OK} \quad \frac{h_0}{t_w} = 31.368 > 6 \quad \text{OK}$$

$$\sigma_{fc} := -670 \text{ MPa} + 33 \text{ MPa} \cdot \left(\frac{b_f}{t_f}\right) - 0.5 \text{ MPa} \left(\frac{b_f}{t_f}\right)^2 \quad (\text{A2-1})$$

$$\sigma_{wc} := -550 \text{ MPa} + 45 \text{ MPa} \cdot \left(\frac{h_0}{t_w}\right) - 1.36 \text{ MPa} \left(\frac{h_0}{t_w}\right)^2 \quad (\text{A2-2})$$

$$-800 \text{ MPa} \leq \sigma_{fc} \leq -80 \text{ MPa} \quad \text{and} \quad -800 \text{ MPa} \leq \sigma_{wc} \leq -80 \text{ MPa}$$

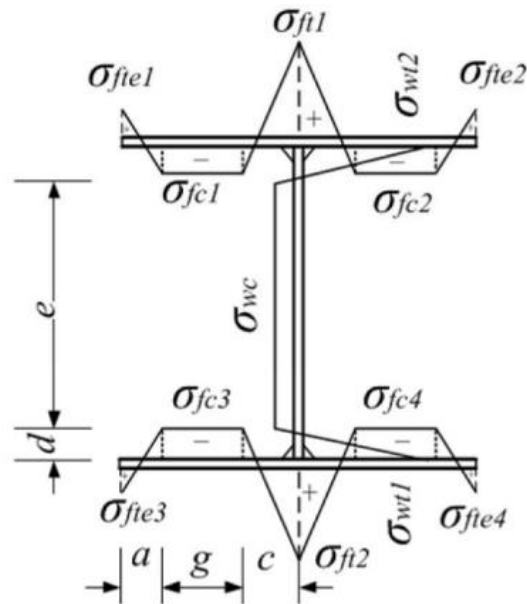


Fig. A 2: Cao et al. (2020) residual stress model

$$\sigma_{ft} := 380 \text{ MPa} \quad \sigma_{wt} := 380 \text{ MPa} \quad \sigma_{fte} := 135 \text{ MPa} \quad \sigma_{fc} = -203.082 \text{ MPa}$$

$$a := 2 t_f \quad a = 14.7 \text{ mm}$$

$$2(a+g+c) = B \quad \text{and} \quad 2d + e = h_0$$

Applying equilibrium conditions,

$$0.25 \sigma_{fte} \cdot a + 0.25 \cdot c \cdot \sigma_{ft} - 0.25 \cdot a \cdot \sigma_{fc} - \sigma_{fc} \cdot g - 0.25 \cdot c \cdot \sigma_{fc} = 0$$

$$g + c = 139.95 \text{ mm}$$

$$c = 115.931 \text{ mm}$$

$$g = 24.019 \text{ mm}$$

$$\sigma_{wc} = -476.613 \text{ MPa} \quad \sigma_{wt} = 380 \text{ MPa}$$

Applying equilibrium conditions,

$$0.5 \cdot 0.75 \cdot d \cdot \sigma_{wt} - 0.125 \cdot d \cdot \sigma_{wc} - \sigma_{wc} \cdot \frac{e}{2} = 0$$

$$2d + e = 229.3 \text{ mm}$$

$$d = 97.651 \text{ mm} \quad e = 33.997 \text{ mm}$$

A.1.3 Calculation of Residual Stresses for 100 ksi built-up specimen:

This section gives brief information on the application of Sun et al. (2019) residual stress model on the I4 specimen used in the benchmark study. The dimensions of the I4 specimen are given in metric units.

$$b_f := 99.35 \text{ mm} \quad h_0 := 189.41 \text{ mm} \quad \sigma_y := 702.6 \text{ MPa} \quad \text{Empirical formula, units in mm and MPa}$$

$$f_{ft} := 0.8 \cdot \sigma_y \quad f_{ft} = 562.08 \text{ MPa}$$

$$f_{wt} := 0.8 \cdot \sigma_y \quad f_{wt} = 562.08 \text{ MPa}$$

$$a := 0.225 b_f \quad b := 0.15 b_f \quad c := 0.075 h_0 \quad d := 0.225 h_0$$

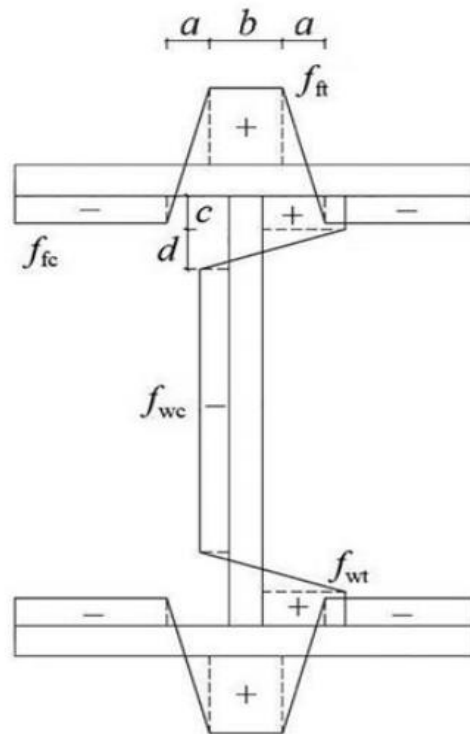


Fig. A 3: Sun et al. (2019) residual stress model

Applying equilibrium conditions,

$$0.25 f_{ft} \cdot a + 0.5 \cdot b \cdot f_{ft} - 0.25 \cdot a \cdot f_{fc} - f_{fc} \cdot \left(\frac{b_f}{2} - a - \frac{b}{2} \right) = 0$$

$$f_{fc} := \frac{0.25 \cdot a \cdot f_{ft} + 0.5 \cdot b \cdot f_{ft}}{\frac{b_f}{2} - 0.75 a - \frac{b}{2}}$$

$$f_{fc} = 287.895 \text{ MPa}$$

$$f_{wt} \cdot \left(c + \frac{d}{4} \right) - f_{wc} \cdot \left(\frac{d}{4} + \frac{h_0}{2} - c - d \right) = 0$$

$$f_{wt} := \frac{f_{wt} \cdot \left(c + \frac{d}{4} \right)}{\frac{h_0}{2} - c - 0.75 d}$$

$$f_{wt} = 287.895 \text{ MPa}$$

A.1.4 Calculation of Residual Stresses for 100 ksi hot-rolled specimen:

This section gives brief information on the application of Galambos et al. (1959) residual stress model on W10×11×1×0.6 hot-rolled specimen used in the parametric study. The dimensions of W10×11×1×0.6 specimen are given in metric units.

$$f_y := 702.6 \text{ MPa} \quad b_f := 261.62 \text{ mm} \quad d := 274.32 \text{ mm} \quad h_w := 224.028 \text{ mm}$$

$$t_w := 15.367 \text{ mm} \quad t_f := 25.146 \text{ mm} \quad \text{Empirical formula, units in mm and MPa}$$

$$\sigma_c := 0.3 f_y \tag{A4-1}$$

$$\sigma_t := \sigma_c \cdot \left(\frac{b_f \cdot t_f}{b_f \cdot t_f + t_w \cdot (d - 2 t_f)} \right) \tag{A4-2}$$

$$\sigma_c = 210.78 \text{ MPa}$$

$$\sigma_t = 138.371 \text{ MPa}$$

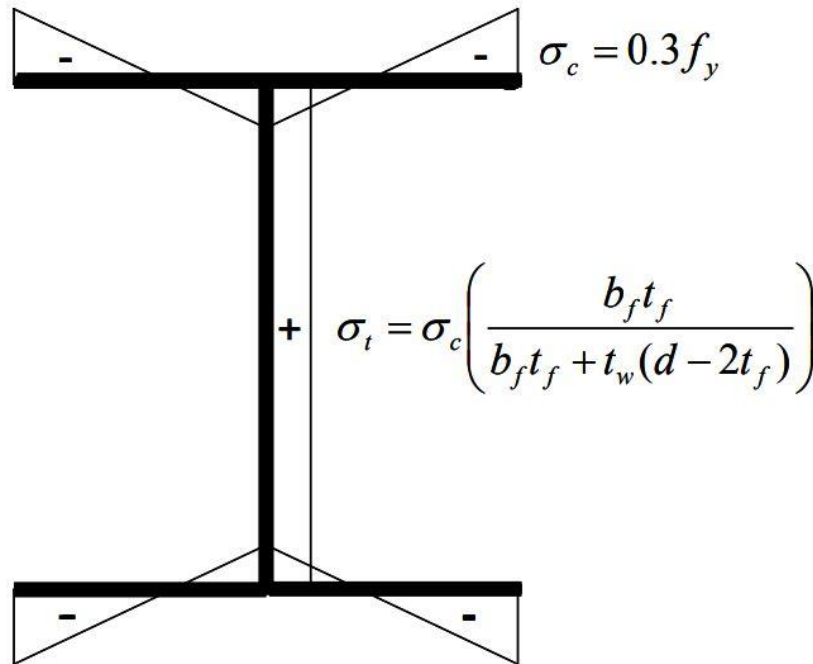


Fig. A 4: Galambos et al. (1959) residual stress model

A.2 RESIDUAL STRESSES IN BUILT-UP W SHAPES

This section shows the applied residual stresses in the remaining built-up W shapes of the parametric study. The table shown below is a continuation of Table 7 from Section 4.1.2.

Table A 1: Applied residual stresses in built-up specimen

Specimen ID	F_y (ksi)	Flange Residual Stress Distribution (ksi)	Web Residual Stress Distribution (ksi)
W12×12×0.6×0.6	100		
W12×12×0.4×0.4	100		
W12×12×0.7×0.7	100		
W12×12×0.7×0.4	100		

Table continued...

Specimen ID	F_y (ksi)	Flange Residual Stress Distribution (ksi)	Web Residual Stress Distribution (ksi)
W10×16×0.3×0.3	100		
W10×16×0.3×0.6	100		
W10×16×0.6×0.6	100		
W10×16×0.6×0.3	100		

Table continued...

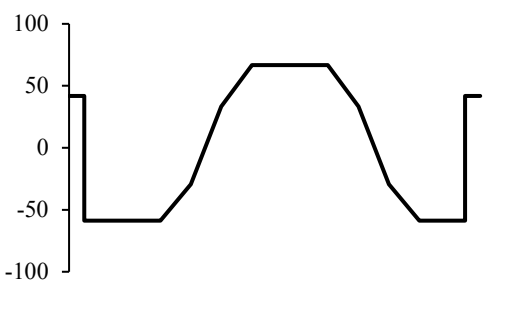
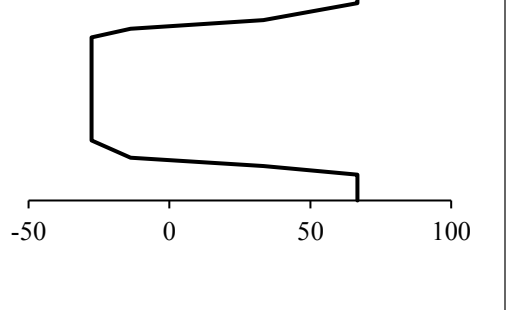
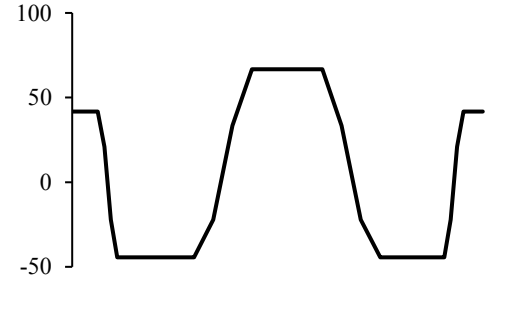
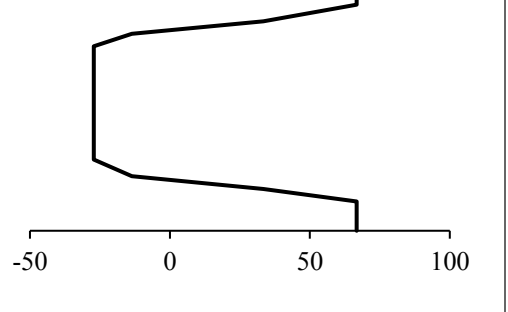
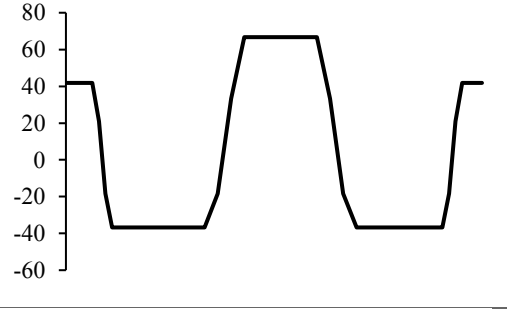
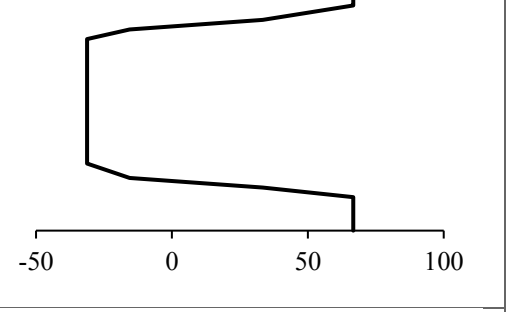
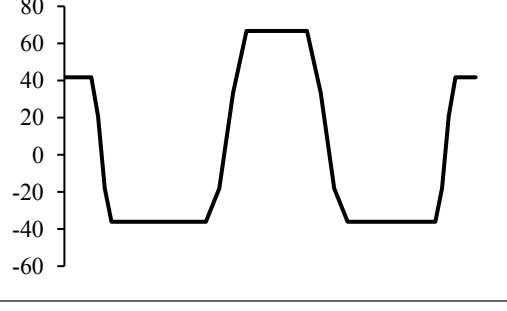
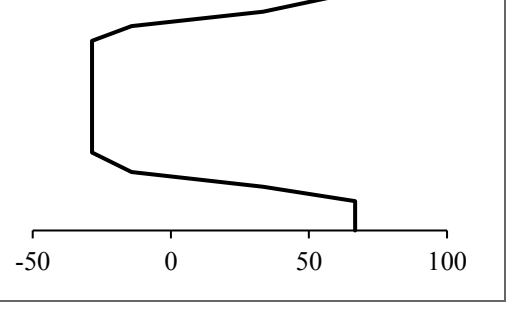
Specimen ID	F_y (ksi)	Flange Residual Stress Distribution (ksi)	Web Residual Stress Distribution (ksi)
W6×6×0.2 ×0.2	140		
W6×6×0.3 ×0.3	140		
W6×6×0.4 ×0.4	140		
W6×6×0.4 ×0.2	140		

Table continued...

Specimen ID	F_y (ksi)	Flange Residual Stress Distribution (ksi)	Web Residual Stress Distribution (ksi)
W12×12×0.6×0.6	140		
W12×12×0.4×0.4	140		
W12×12×0.7×0.7	140		
W12×12×0.7×0.4	140		

Table continued...

Specimen ID	F_y (ksi)	Flange Residual Stress Distribution (ksi)	Web Residual Stress Distribution (ksi)
W10×16×0.3×0.3	140		
W10×16×0.3×0.6	140		
W10×16×0.6×0.6	140		
W10×16×0.6×0.3	140		

A.3 RESIDUAL STRESSES IN HOT-ROLLED W SHAPES

This section shows the applied residual stresses in remaining hot-rolled W shapes of the parametric study. The table shown below is a continuation of Table 11 from Section 4.2.2.

Table A 2: Applied residual stresses in hot-rolled specimen

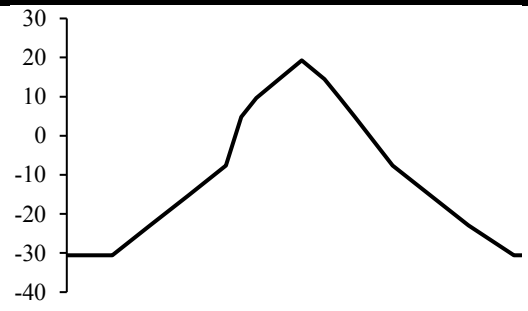
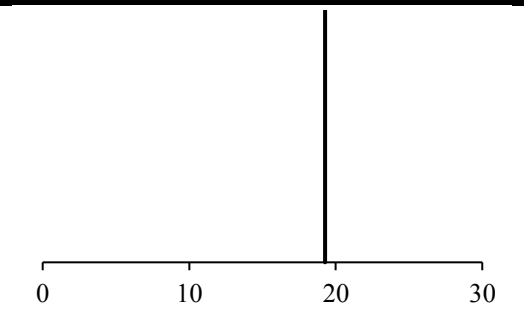
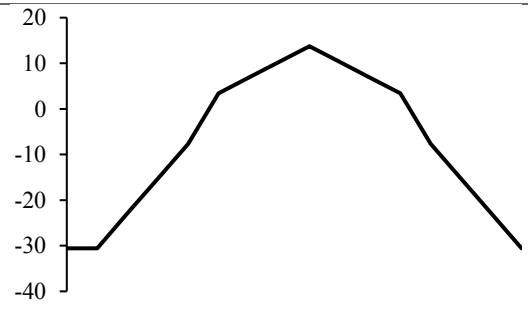
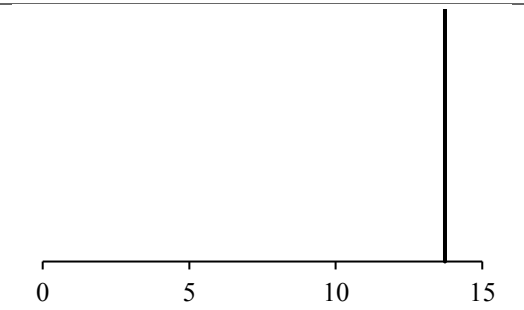
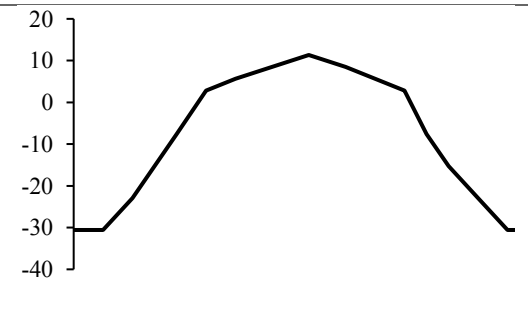
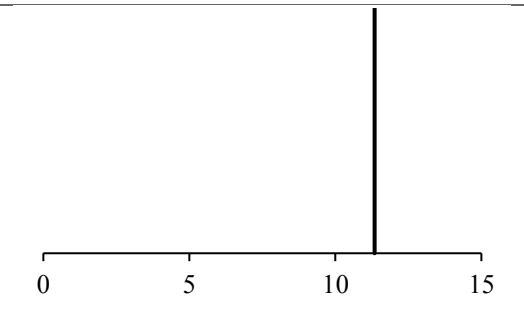
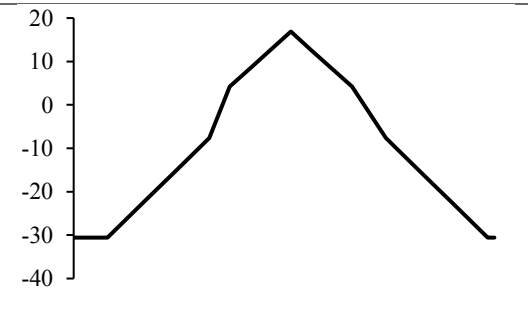
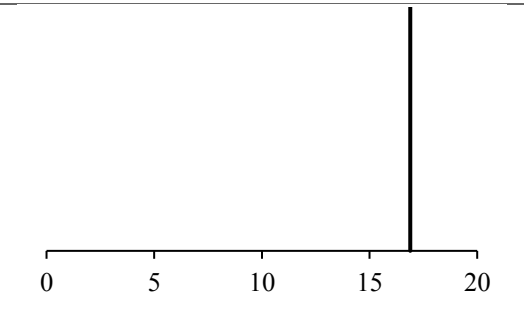
Specimen ID	F_y (ksi)	Flange Residual Stress Distribution (ksi)	Web Residual Stress Distribution (ksi)
W12×12×0.7×0.4	100		
W12×12×0.7×0.9	100		
W12×12×0.5×0.9	100		
W12×12×0.5×0.4	100		

Table continued...

Specimen ID	F_y (ksi)	Flange Residual Stress Distribution (ksi)	Web Residual Stress Distribution (ksi)
W14×14×0.9×0.5	100		
W14×14×0.7×0.5	100		
W14×14×0.7×0.3	100		
W14×14×0.7×0.3	100		

Table continued...

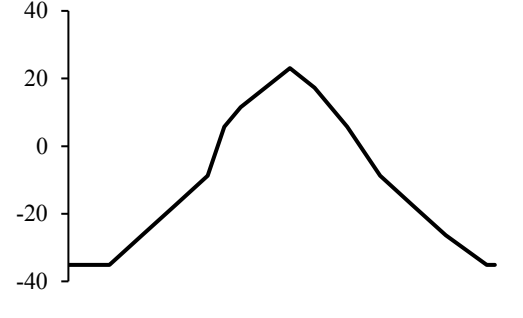
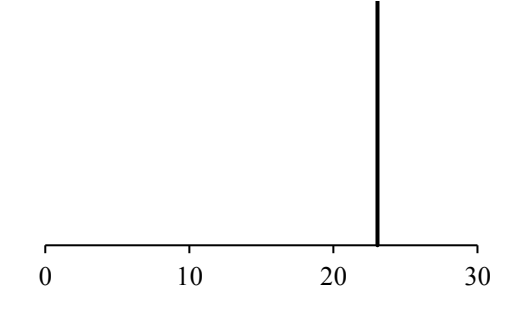
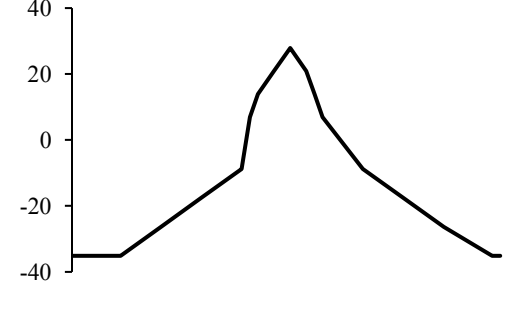
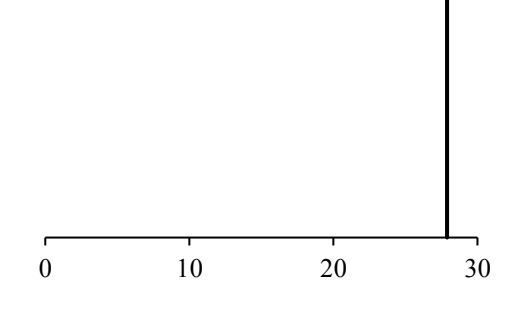
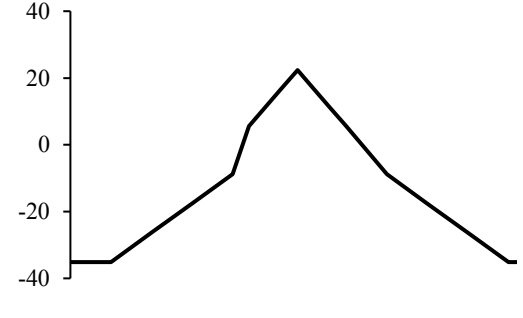
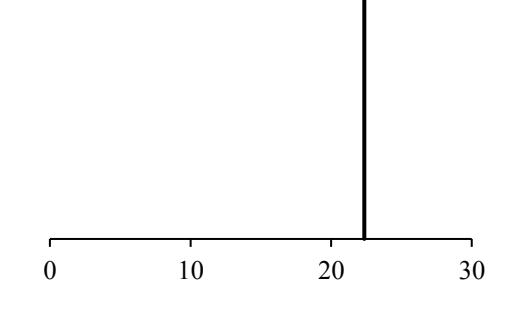
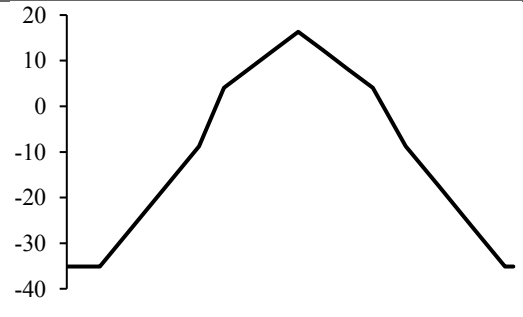
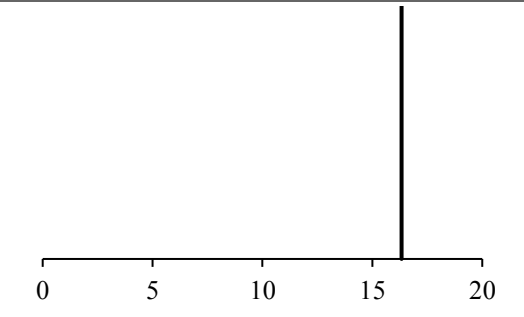
Specimen ID	F_y (ksi)	Flange Residual Stress Distribution (ksi)	Web Residual Stress Distribution (ksi)
W10×11×1×0.6	120		
W10×11×1×0.3	120		
W10×11×0.5×0.3	120		
W10×11×0.5×0.6	120		

Table continued...

Specimen ID	F_y (ksi)	Flange Residual Stress Distribution (ksi)	Web Residual Stress Distribution (ksi)
W12×12×0.7×0.4	120		
W12×12×0.9×0.9	120		
W12×12×0.5×0.9	120		
W12×12×0.9×0.4	120		

Table continued...

Specimen ID	F_y (ksi)	Flange Residual Stress Distribution (ksi)	Web Residual Stress Distribution (ksi)
W14×14×0.9×0.5	120		
W14×14×0.7×0.5	120		
W14×14×0.9×0.6	120		
W14×14×0.7×0.6	120		

APPENDIX B – INITIAL GEOMETRIC IMPERFECTIONS

This section gives a detailed information on the permissible variation in length, camber, and sweep limits for HS3 plates and hot-rolled W shapes.

B.1 Permitted variation in length and camber in HS3 plates

- Permitted Camber for High-Strength Low-Alloy Steel, and Alloy Steel Universal Mill Plates and High Strength Low-Alloy Steel and Alloy Steel Sheared, Special-Cut, or Gas-Cut Rectangular Plates is given by the following formula (ASTM, 2019).

$$\text{Permitted camber, in.} = \left(\frac{1}{8}\right) \left(\frac{\text{“Number of feet of length”}}{5}\right) \quad (\text{B1-1})$$

- For members that have both ends finished for contact bearing, the variation in overall length shall be equal to or less than 1/32 in. (AISC, 2016).
- For members that are equal to or less than 30 ft. in length, the variation shall be equal to or less than 1/16 in. (AISC, 2016).
- Permitted Variations from a Flat Surface for Standard Flatness High-Strength Low-Alloy Steel and Alloy Steel Plates, Hot Rolled or Thermally Treated (ASTM, 2019).
 - NOTE 1—When the longer dimension is under 36 in., the permitted variation from a flat surface shall not exceed 3/8 in. When the longer dimension is from 36 to 72 in. incl, the permitted variation from a flat surface shall not exceed 75 % of the tabular amount for the specified width.
 - NOTE 2—This table and these notes cover the permitted variations from a flat surface for circular and sketch plates, based upon the maximum dimensions of such plates.
 - NOTE 3—Where “...” appears in this table, there is no requirement.

- NOTE 4—Plates must be in a horizontal position on a flat surface when flatness is measured.

Table B 1: Permitted variations from flat surface for plates (ASTM, 2019)

Specified Thickness, in.	Specified Weight, lb/ft ²	Permitted Variations from a Flat Surface for Specified Widths, in. ^{A,B}										
		To 36, excl	36 to 48, excl	48 to 60, excl	60 to 72, excl	72 to 84, excl	84 to 96, excl	96 to 108, excl	108 to 120, excl	120 to 144, excl	144 to 168, excl	168 and Over
To 1/4, excl	To 10.2, excl	13/16	11/8	13/8	17/8	2	2 1/4	2 3/8	2 5/8	2 3/4
1/4 to 3/8, excl	10.2 to 15.3, excl	3/4	15/16	1 1/8	1 3/8	1 3/4	1 7/8	2	2 1/4	2 3/8
3/8 to 1/2, excl	15.3 to 20.4, excl	3/4	7/8	15/16	15/16	1 1/8	1 5/16	1 1/2	1 5/8	1 7/8	2 3/4	3 1/8
1/2 to 3/4, excl	20.4 to 30.6, excl	5/8	3/4	13/16	7/8	1	1 1/8	1 1/4	1 3/8	1 5/8	2 1/4	3
3/4 to 1, excl	30.6 to 40.8, excl	5/8	3/4	7/8	7/8	15/16	1	1 1/8	1 5/16	1 1/2	2	2 5/8
1 to 2, excl	40.8 to 81.7, excl	9/16	5/8	3/4	13/16	7/8	15/16	1	1	1	1 5/8	2 1/4
2 to 4, excl	81.7 to 163.4, excl	1/2	9/16	11/16	3/4	3/4	3/4	3/4	7/8	1	1 1/4	1 5/8
4 to 6, excl	163.4 to 245.1, excl	9/16	11/16	3/4	3/4	7/8	7/8	15/16	1 1/8	1 1/4	1 1/4	1 1/2
6 to 8, excl	245.1 to 326.8, excl	5/8	3/4	3/4	15/16	1	1 1/8	1 1/4	1 5/16	1 1/2	1 1/2	1 1/2
8 to 10, excl	326.8 to 409.0, excl	3/4	13/16	15/16	1	1 1/8	1 1/4	1 5/16	1 3/8	1 1/2	1 1/2	1 1/2
10 to 12, excl	409.0 to 490.1, excl	3/4	15/16	1 1/8	1 1/4	1 5/16	1 3/8	1 1/2	1 1/2	1 1/2	1 1/2	1 1/2
12 to 15, incl	490.1 to 613.0, incl	7/8	1	1 3/16	1 5/16	1 3/8	1 1/2	1 1/2	1 1/2	1 1/2	1 1/2	1 1/2

- ^A Permitted Variation from a Flat Surface for Length—The longer dimension specified is considered the length, and the permitted variation from a flat surface along the length shall not exceed the tabular amount for the specified width in plates up to 12 ft in length, or in any 12 ft for longer plates.
- ^B Permitted Variation from a Flat Surface for Width—The permitted variation from a flat surface across the width shall not exceed the tabular amount for the specified width.
- Permitted Variations in Waviness for Standard Flatness Plates (ASTM, 2019)
- NOTE 1—Waviness denotes the maximum deviation of the surface of the plate from a plane parallel to the surface of the point of measurement and contiguous to the surface of the plate at each of the two adjacent wave peaks, when the plate is resting on a flat horizontal surface, as measured in an increment of less than 12 ft of length. The permitted

variation in waviness is a function of the permitted variation from a flat surface as obtained from Table 13 or Table 14 of ASTM A6, whichever is applicable.

- NOTE 2—Plates must be in a horizontal position on a flat surface when waviness is measured.

Table B 2: Permitted variation in waviness (ASTM, 2019)

Permitted Variation from a Flat Surface (from Table 13 or Table 14), in.	Permitted Variation in Waviness, in., When Number of Waves in 12 ft is						
	1	2	3	4	5	6	7
5/16	5/16	1/4	3/16	1/8	1/8	1/16	1/16
3/8	3/8	5/16	3/16	3/16	1/8	1/16	1/16
7/16	7/16	5/16	1/4	3/16	1/8	1/8	1/16
1/2	1/2	3/8	5/16	3/16	3/16	1/8	1/16
9/16	9/16	7/16	5/16	1/4	3/16	1/8	1/8
5/8	5/8	1/2	3/8	1/4	3/16	1/8	1/8
11/16	11/16	1/2	3/8	5/16	3/16	3/16	1/8
3/4	3/4	9/16	7/16	5/16	1/4	3/16	1/8
13/16	13/16	5/8	7/16	5/16	1/4	3/16	1/8
7/8	7/8	11/16	1/2	3/8	1/4	3/16	1/8
15/16	15/16	11/16	1/2	3/8	5/16	1/4	3/16
1	1	3/4	9/16	7/16	5/16	1/4	3/16
1 1/8	1 1/8	7/8	5/8	1/2	3/8	1/4	3/16
1 1/4	1 1/4	15/16	11/16	1/2	3/8	5/16	1/4
1 3/8	1 3/8	1 1/16	3/4	9/16	7/16	5/16	1/4
1 1/2	1 1/2	1 1/8	7/8	5/8	1/2	3/8	1/4
1 5/8	1 5/8	1 1/4	15/16	11/16	1/2	3/8	5/16
1 3/4	1 3/4	1 5/16	1	3/4	9/16	7/16	5/16
1 7/8	1 7/8	1 7/16	1 1/16	13/16	9/16	7/16	5/16
2	2	1 1/2	1 1/8	7/8	5/8	1/2	3/8
2 1/8	2 1/8	1 5/8	1 3/16	7/8	11/16	1/2	3/8
2 1/4	2 1/4	1 11/16	1 1/4	15/16	11/16	9/16	3/8
2 3/8	2 3/8	1 13/16	1 5/16	1	3/4	9/16	7/16
2 1/2	2 1/2	1 7/8	1 7/16	1 1/16	13/16	9/16	7/16
2 5/8	2 5/8	2	1 1/2	1 1/8	13/16	5/8	7/16
2 3/4	2 3/4	2 1/16	1 9/16	1 1/8	7/8	5/8	1/2
2 7/8	2 7/8	2 3/16	1 5/8	1 3/16	15/16	11/16	1/2
3	3	2 1/4	1 11/16	1 1/4	15/16	11/16	9/16
3 1/8	3 1/8	2 3/8	1 3/4	1 5/16	1	3/4	9/16

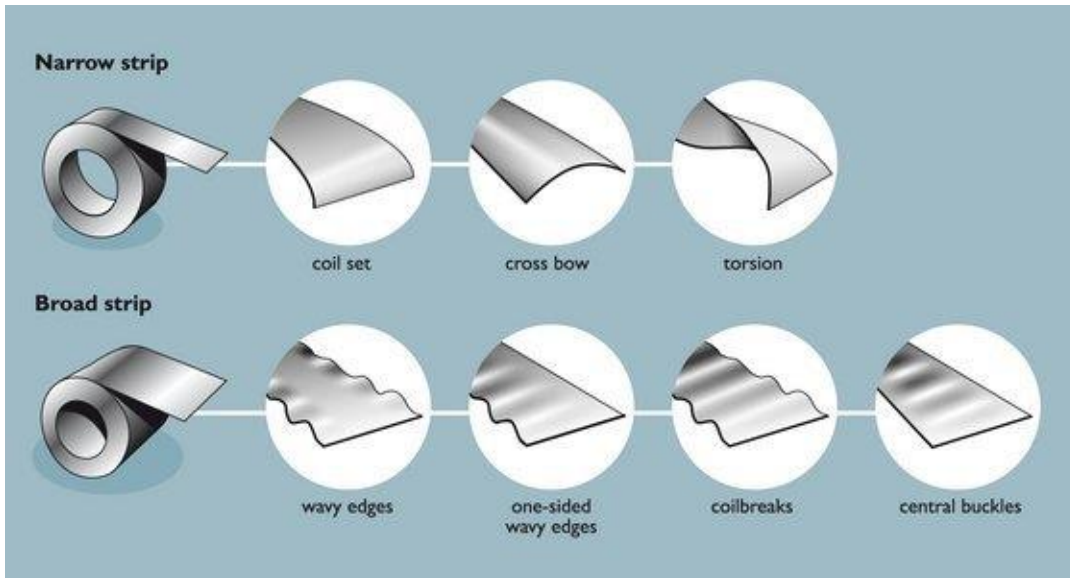


Fig. B 1: Flatness defects in hot-rolled steel: bow shaped defects and waviness defects (Sunthorn and Kittiphat, 2014)

B.2 Permitted variation in length, camber, and sweep in W shapes

- Permitted variations in length for hot-rolled W and HP Shapes (ASTM, 2019)

Table B 3: Permitted variations from length for wide flange sections (ASTM, 2019)

Permitted Variations from Specified Length for Lengths Given in Feet, in. ^{A, B}	
Over	Under
4	0

- ^A For HP and W shapes specified in the order for use as bearing piles, the permitted variations in length are plus 5 in. and minus 0 in. These permitted variations in length also apply to sheet piles.
- ^B The permitted variations in end out-of-square for W and HP shapes shall be 1/64 in. per inch of depth, or per inch of flange width if the flange width is larger than the depth.

- Permitted variations in straightness for hot-rolled W and HP Shapes (ASTM, 2019)

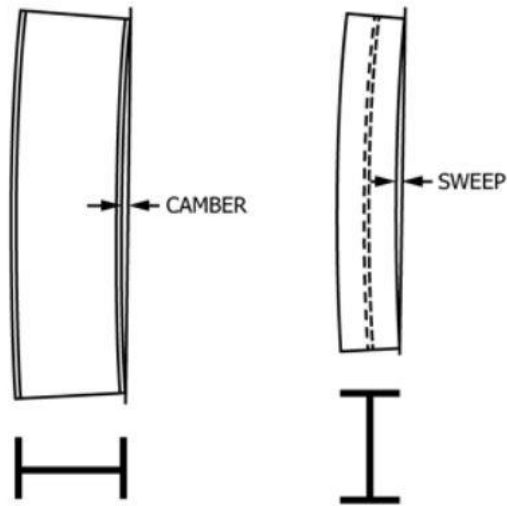


Fig. B 2: Camber and sweep in wide flange sections

$$\text{Permitted camber and sweep, in.} = \left(\frac{1}{8}\right) \left(\frac{\text{"Number of feet of length"}}{10}\right) \quad (\text{B2-1})$$

APPENDIX C – AISC SLENDERNESS LIMITS

This section gives brief information on AISC section slenderness limits and AISC member slenderness limits.

C.1 Section Slenderness Limit

Wide flange built-up and rolled sections can be classified based on their section slenderness ratios. Section slenderness ratio of the flange is the ratio of the half-width of the flange to the thickness of the flange. Similarly, section slenderness ratio of the web is the ratio of the depth of the web to the thickness of the web. AISC 360 (2016) *Specification* classifies the wide flange sections subject to axial compression as nonslender-element or slender-element sections based on the limiting width-to-thickness ratio (λ_r). Limiting width-to-thickness ratio (λ_r) is the value that AISC 360 (2016) uses to distinguish between nonslender-element or slender-element sections.

Limiting width-to-thickness ratio of the flange (λ_{rf}) for rolled wide flange sections is given by the following formula.

$$\lambda_{rf} = 0.56 \sqrt{\frac{E}{F_y}} \quad (C1-1)$$

Limiting width-to-thickness ratio of the flange (λ_{rf}) for built-up wide flange sections is given by the following formula.

$$\lambda_{rf} = 0.64 \sqrt{\frac{k_c E}{F_y}} \quad (C1-2)$$

Where k_c is given by, (C1-3)

$$k_c = \frac{4}{\sqrt{\frac{h_w}{t_w}}}$$

Limiting width-to-thickness ratio of the web (λ_{rw}) for both built-up and hot-rolled wide flange sections is given by the following formula.

$$\lambda_{rw} = 1.49 \sqrt{\frac{E}{F_y}} \quad (C1-4)$$

For a nonslender-element section, the section slenderness ratio of its compression elements shall not exceed λ_r . If the section slenderness ratio of any compression element exceeds λ_r , the section is a slender-element section.

C.2 Member Slenderness Limit

AISC 360 (2016) *Specification* distinguishes wide flange section columns as slender members and non-slender members based on their effective slenderness ratios. Effective slenderness ratio (λ) is defined as the ratio of length of the column to its weak axis radius of gyration. Limiting effective slenderness ratio (λ_l) is defined as the value that AISC 360 (2016) uses to separate slender and non-slender columns. For members designed based on compression, the effective slenderness ratio (λ) preferably should not exceed 200 (AISC, 2016).

Limiting effective slenderness ratio of the column (λ_l) for both built-up and hot-rolled wide flange sections is given by the following formula.

$$\lambda_l = 4.71 \sqrt{\frac{E}{F_y}} \quad (C2-1)$$

APPENDIX D – ABAQUS MACROS AND PYTHON CODE EDITING

This section gives brief information on ABAQUS macros used during the modeling process in the parametric study. This section also describes the Python script editing process that enabled easy automation and simplified the modeling process.

Macro is defined as an action or a set of actions that run repeatedly until the end goal is met. In this case, ABAQUS macros were used to model repeated sections of the FE model in ABAQUS. This process was very efficient and brought down the modeling time from around 1hr per model to under 10 min. Batch Python scripts were created with the help of the recorded ABAQUS macros and selective portions of the Python script were edited to account for the differences in the FE models. These edited Python scripts were imported as ABAQUS macro files to model the new FE model in ABAQUS. At first, during the modeling stage, ABAQUS macro is recorded to account for the repetitive process. It is done by going to the macro manager window in **File > Macro manager**, then click on **Create**.

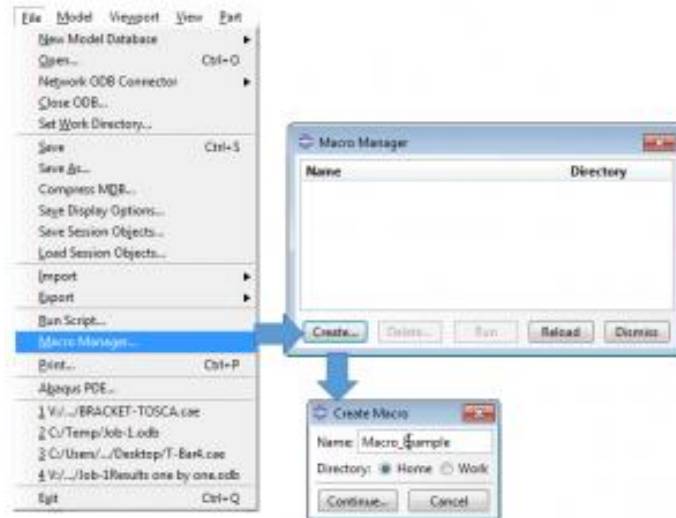


Fig. D 1: Steps for creating ABAQUS macro

Then, give a name to the ABAQUS macro and the location (**Home** or **Work** location) where it needs to be saved. Remember this file location is very important as it is required to retrieve the ABAQUS macro file to edit in later stages. Next, click on **Continue**. A window pops up that tells that the Macro is being recorded. Move the window to lower corner and start modelling in ABAQUS. Remember, do not close the previous window until recording is complete.

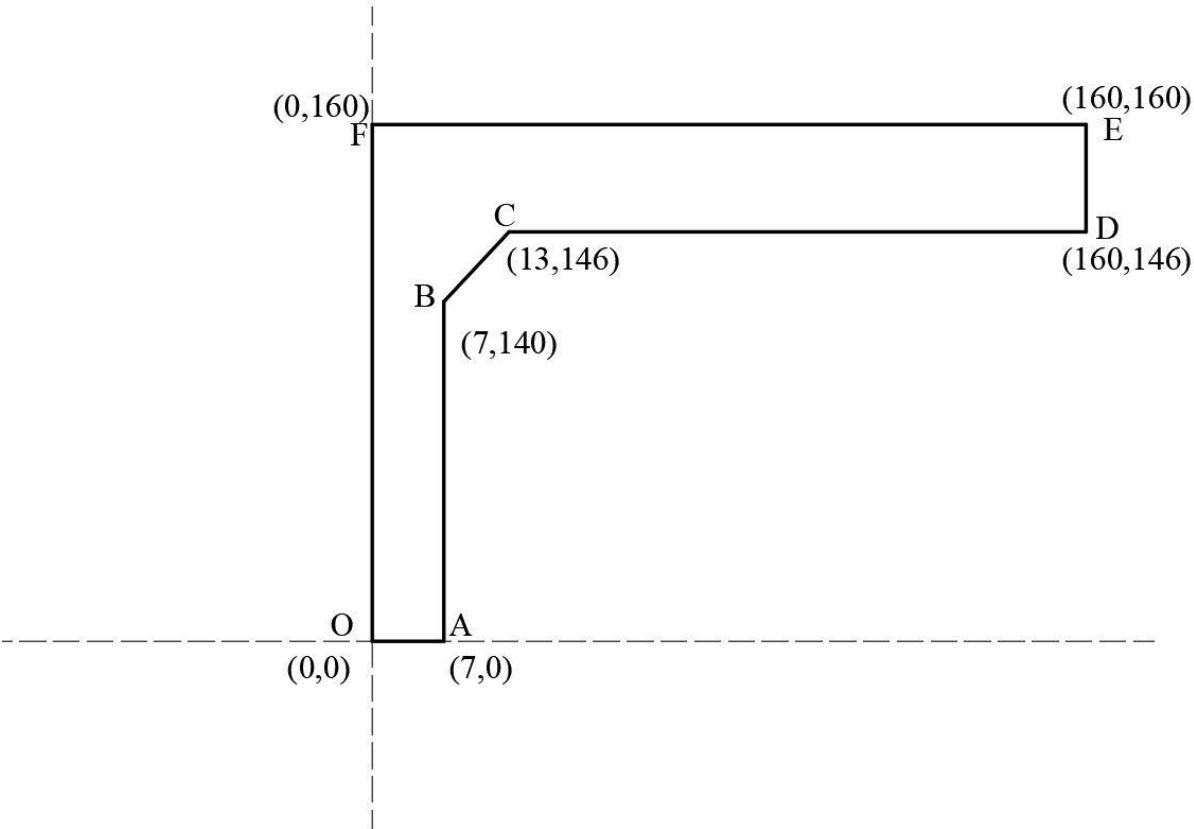


Fig. D 2: Schematic diagram showing part of I-section

One-fourth drawing of I-section was drawn in ABAQUS modeler. Remaining parts of the I-section was obtained by mirroring the one-fourth part. Fig. D2 shows a schematic diagram representing the drawing of one-fourth part of I-section in ABAQUS modeler. ABAQUS macros were stopped

before the end of repeat portion or at the beginning of analysis phase. The ABAQUS macro was saved as a Python script file in **.py** format.

The saved ABAQUS macro file was edited through Python script editor (Notepad++) to change the dimensions of the I-section as per the one-fourth section shown in Fig. D2 and the length of the specimen to create a new ABAQUS macro file. Many such ABAQUS macro files were created in batches as per new dimensions and material properties of the FE models.

Now, the newly edited ABAQUS macro-Python script is pasted on to the new work location of the next FE model. A new ABAQUS file was created to model the new I-section. The edited macro is run by going to **File > Macro manager**, then **run**. This starts modeling the new FE model as per new dimensions and material properties. Remember, the application of residual stresses is not a repetitive process and cannot be repeated by editing ABAQUS macros. So, this required the modeler to use multiple ABAQUS macros for the same FE model.

The following is an example of a Python script developed using ABAQUS macros for a FE model.

```
# -*- coding: mbcs -*-
# Do not delete the following import lines
from abaqus import *
from abaqusConstants import *
import __main__
def Till_EigenBuckling():
    import section
    import regionToolset
    import displayGroupMdbToolset as dgm
    import part
    import material
    import assembly
```

```

import step
import interaction
import load
import mesh
import optimization
import job
import sketch
import visualization
import xyPlot
import displayGroupOdbToolset as dgo
import connectorBehavior
s = mdb.models['Model-1'].ConstrainedSketch(name='__profile__',
    sheetSize=320.0)
g, v, d, c = s.geometry, s.vertices, s.dimensions, s.constraints
s.setPrimaryObject(option=STANDALONE)
s.Line(point1=(0.0, 0.0), point2=(3.5, 0.0))
s.HorizontalConstraint(entity=g[2], addUndoState=False)
s.Line(point1=(3.5, 0.0), point2=(3.5, 62))
s.VerticalConstraint(entity=g[3], addUndoState=False)
s.PerpendicularConstraint(entity1=g[2], entity2=g[3], addUndoState=False)
s.Line(point1=(3.5, 62), point2=(9.5, 68))
s.Line(point1=(9.5, 68), point2=(75, 68))
s.HorizontalConstraint(entity=g[5], addUndoState=False)
s.Line(point1=(75, 68), point2=(75, 75))
s.VerticalConstraint(entity=g[6], addUndoState=False)
s.PerpendicularConstraint(entity1=g[5], entity2=g[6], addUndoState=False)
s.Line(point1=(75, 75), point2=(0.0, 75))
s.HorizontalConstraint(entity=g[7], addUndoState=False)
s.PerpendicularConstraint(entity1=g[6], entity2=g[7], addUndoState=False)
s.Line(point1=(0.0, 75), point2=(0.0, 0.0))

```

```

s.VerticalConstraint(entity=g[8], addUndoState=False)
s.PerpendicularConstraint(entity1=g[7], entity2=g[8], addUndoState=False)
s.setAsConstruction(objectList=(g[2], g[8]))
s.copyMirror(mirrorLine=g[8], objectList=(g[2], g[3], g[4], g[5], g[6], g[7]))
session.viewports['Viewport: 1'].view.setValues(nearPlane=242.175,
    farPlane=361.223, width=566.5, height=306.56, cameraPosition=(106.825,
    72.8246, 301.699), cameraTarget=(106.825, 72.8246, 0))
s.copyMirror(mirrorLine=g[9], objectList=(g[3], g[4], g[5], g[6], g[7], g[8],
    g[10], g[11], g[12], g[13], g[14]))
p = mdb.models['Model-1'].Part(name='I150x150x5', dimensionality=THREE_D,
    type=DEFORMABLE_BODY)
p = mdb.models['Model-1'].parts['I150x150x5']
p.BaseSolidExtrude(sketch=s, depth=450)
s.unsetPrimaryObject()
p = mdb.models['Model-1'].parts['I150x150x5']
session.viewports['Viewport: 1'].setValues(displayedObject=p)
del mdb.models['Model-1'].sketches['__profile__']
mdb.save()
p = mdb.models['Model-1'].parts['I150x150x5']
c = p.cells
pickedCells = c.getSequenceFromMask(mask=('[#1 ]', ), )
v1, e, d1 = p.vertices, p.edges, p.datums
p.PartitionCellByPlaneThreePoints(point1=v1[24], point2=v1[32], point3=v1[33],
    cells=pickedCells)
p = mdb.models['Model-1'].parts['I150x150x5']
c = p.cells
pickedCells = c.getSequenceFromMask(mask=('[#2 ]', ), )
v2, e1, d2 = p.vertices, p.edges, p.datums
p.PartitionCellByPlaneThreePoints(point1=v2[8], point2=v2[12], point3=v2[24],
    cells=pickedCells)

```

```

p = mdb.models['Model-1'].parts['I150x150x5']
c = p.cells
pickedCells = c.getSequenceFromMask(mask=('#7'], ), )
v1, e, d1 = p.vertices, p.edges, p.datums
p.PartitionCellByPlaneThreePoints(point1=v1[27], point2=v1[37],
    cells=pickedCells, point3=p.InterestingPoint(edge=e[20], rule=MIDDLE))
session.viewports['Viewport: 1'].view.setValues(nearPlane=1698.13,
    farPlane=2587.35, width=107.104, height=57.9592, viewOffsetX=242.254,
    viewOffsetY=74.6255)
p = mdb.models['Model-1'].parts['I150x150x5']
c = p.cells
pickedCells = c.getSequenceFromMask(mask=('#a'], ), )
v2, e1, d2 = p.vertices, p.edges, p.datums
p.PartitionCellByPlaneThreePoints(point1=v2[39], point2=v2[21], point3=v2[36],
    cells=pickedCells)
p = mdb.models['Model-1'].parts['I150x150x5']
c = p.cells
pickedCells = c.getSequenceFromMask(mask=('#6'], ), )
v1, e, d1 = p.vertices, p.edges, p.datums
p.PartitionCellByPlaneThreePoints(point1=v1[16], point2=v1[35], point3=v1[12],
    cells=pickedCells)
session.viewports['Viewport: 1'].view.setValues(nearPlane=1727.48,
    farPlane=2670.31, width=748.482, height=405.039, viewOffsetX=-162.216,
    viewOffsetY=-36.0596)
mdb.save()
p = mdb.models['Model-1'].parts['I150x150x5']
c = p.cells
pickedCells = c.getSequenceFromMask(mask=('#6'], ), )
e1, d2 = p.edges, p.datums
pickedEdges =(e1[1], e1[5])

```

```

p.PartitionCellByExtrudeEdge(line=e1[85], cells=pickedCells, edges=pickedEdges,
    sense=FORWARD)
p = mdb.models['Model-1'].parts['I150x150x5']
c = p.cells
pickedCells = c.getSequenceFromMask(mask=('#48 ', ), )
e, d1 = p.edges, p.datums
pickedEdges =(e[27], e[29])
p.PartitionCellByExtrudeEdge(line=e[74], cells=pickedCells, edges=pickedEdges,
    sense=FORWARD)
p = mdb.models['Model-1'].parts['I150x150x5']
c = p.cells
pickedCells = c.getSequenceFromMask(mask=('#c ', ), )
v2, e1, d2 = p.vertices, p.edges, p.datums
p.PartitionCellByPlaneThreePoints(point1=v2[1], point2=v2[0], point3=v2[23],
    cells=pickedCells)
p = mdb.models['Model-1'].parts['I150x150x5']
c = p.cells
pickedCells = c.getSequenceFromMask(mask=('#44 ', ), )
v1, e, d1 = p.vertices, p.edges, p.datums
p.PartitionCellByPlaneThreePoints(point1=v1[30], point2=v1[45], point3=v1[27],
    cells=pickedCells)
p = mdb.models['Model-1'].parts['I150x150x5']
c = p.cells
pickedCells = c.getSequenceFromMask(mask=('#a00 ', ), )
v2, e1, d2 = p.vertices, p.edges, p.datums
p.PartitionCellByPlaneThreePoints(cells=pickedCells, point1=p.InterestingPoint(
    edge=e1[108], rule=MIDDLE), point2=p.InterestingPoint(edge=e1[71],
    rule=MIDDLE), point3=p.InterestingPoint(edge=e1[99], rule=MIDDLE))
p = mdb.models['Model-1'].parts['I150x150x5']
c = p.cells

```

```

pickedCells = c.getSequenceFromMask(mask=('[#c000 ]', ), )
v1, e, d1 = p.vertices, p.edges, p.datums
p.PartitionCellByPlaneThreePoints(cells=pickedCells, point1=p.InterestingPoint(
    edge=e[107], rule=MIDDLE), point2=p.InterestingPoint(edge=e[112],
    rule=MIDDLE), point3=p.InterestingPoint(edge=e[98], rule=MIDDLE))
p = mdb.models['Model-1'].parts['I150x150x5']
c = p.cells
pickedCells = c.getSequenceFromMask(mask=('[#11000 ]', ), )
v2, e1, d2 = p.vertices, p.edges, p.datums
p.PartitionCellByPlaneThreePoints(point1=v2[18], point2=v2[53], point3=v2[61],
    cells=pickedCells)
mdb.save()
session.viewports['Viewport: 1'].partDisplay.setValues(sectionAssignments=ON,
    engineeringFeatures=ON)
session.viewports['Viewport: 1'].partDisplay.geometryOptions.setValues(
    referenceRepresentation=OFF)
mdb.models['Model-1'].Material(name='Steel_690MPa_100ksi')
mdb.models['Model-1'].materials['Steel_690MPa_100ksi'].Density(table=((
    7.85e-09, ), ))
mdb.models['Model-1'].materials['Steel_690MPa_100ksi'].Elastic(table=((
    216290.0, 0.3), ))
mdb.models['Model-1'].materials['Steel_690MPa_100ksi'].Plastic(table=((
    657.6821849, 0.0), (675.8947626, 0.000576013), (685.2059269,
    0.001151695), (690.956526, 0.001727045), (696.7132867, 0.002302065), (
    700.8900191, 0.003163974), (705.4775295, 0.004598842), (710.4819796,
    0.006604204), (711.7019903, 0.008319891), (713.1253362, 0.010317812), (
    714.9553523, 0.012880716), (718.5954325, 0.015437069), (719.8185241,
    0.017137681), (723.0622035, 0.019118079), (726.108196, 0.020812448), (
    729.3657392, 0.02278559), (732.4245684, 0.024473761), (735.6959754,
    0.026439699), (738.7676414, 0.028121718), (742.4677979, 0.030639453), (

```

746.1771969, 0.033150865), (751.9518558, 0.035933946), (758.1670742, 0.039263451), (764.6179764, 0.042857948), (768.382317, 0.0453389), (772.1559, 0.047813711), (774.2765416, 0.050556337), (779.9438848, 0.053018285), (783.7457088, 0.055474187), (785.4545455, 0.05765216), (789.0556017, 0.059825399), (793.5233997, 0.063076427), (797.573231, 0.065777567), (802.0646486, 0.069009334), (804.2212333, 0.071694517), (806.1621595, 0.074105032), (809.8109688, 0.076242846), (812.1888601, 0.079174897), (814.7829234, 0.082363723), (819.1018143, 0.085277908), (821.051983, 0.087655941), (823.2188371, 0.090291584), (825.6023766, 0.09318279), (827.1191745, 0.095018306), (828.6359724, 0.096850459), (830.8028265, 0.099462011), (830.7796469, 0.101806591), (834.703164, 0.104145686), (836.6533327, 0.106479323), (837.0486332, 0.10932417), (838.9941806, 0.111645768), (841.1559, 0.114219015), (843.3176194, 0.116785657), (841.6779549, 0.119601376), (843.3991149, 0.121644203), (843.3179129, 0.123937406), (841.8461538, 0.126986853), (840.1371705, 0.129774034), (838.4055944, 0.132553468), (834.1907917, 0.134821818), (832.4104357, 0.137587277), (829.7756614, 0.139343141), (824.8676708, 0.140845717), (825.6933346, 0.141846181)))

mdb.save()

```
mdb.models['Model-1'].HomogeneousSolidSection(name='I150x150x5',
    material='Steel_690MPa_100ksi', thickness=None)
```

```
p = mdb.models['Model-1'].parts['I150x150x5']
```

```
c = p.cells
```

```
cells = c.getSequenceFromMask(mask=('#ffff' ], ), )
```

```
region = regionToolset.Region(cells=cells)
```

```
p = mdb.models['Model-1'].parts['I150x150x5']
```

```
p.SectionAssignment(region=region, sectionName='I150x150x5', offset=0.0,
    offsetType=MIDDLE_SURFACE, offsetField="",
    thicknessAssignment=FROM_SECTION)
```

mdb.save()

```

a = mdb.models['Model-1'].rootAssembly
a.DatumCsysByDefault(CARTESIAN)
p = mdb.models['Model-1'].parts['I150x150x5']
a.Instance(name='I150x150x5-1', part=p, dependent=ON)
a = mdb.models['Model-1'].rootAssembly
v1 = a.instances['I150x150x5-1'].vertices
verts1 = v1.getSequenceFromMask(mask=('[#0 #20000 ]', ), )
region1=regionToolset.Region(vertices=verts1)
a = mdb.models['Model-1'].rootAssembly
s1 = a.instances['I150x150x5-1'].faces
side1Faces1 = s1.getSequenceFromMask(mask=('[#40422200 #10906781 #1000048a ]',
), )
region2=regionToolset.Region(side1Faces=side1Faces1)
mdb.models['Model-1'].Coupling(name='LoadSideConstraint', controlPoint=region1,
    surface=region2, influenceRadius=WHOLE_SURFACE, couplingType=KINEMATIC,
    localCsys=None, u1=ON, u2=ON, u3=ON, ur1=OFF, ur2=OFF, ur3=OFF)
a = mdb.models['Model-1'].rootAssembly
v1 = a.instances['I150x150x5-1'].vertices
verts1 = v1.getSequenceFromMask(mask=('[#0 #40000 ]', ), )
region1=regionToolset.Region(vertices=verts1)
a = mdb.models['Model-1'].rootAssembly
s1 = a.instances['I150x150x5-1'].faces
side1Faces1 = s1.getSequenceFromMask(mask=('[#28301428 #c0630050 #20000910 ]',
), )
region2=regionToolset.Region(side1Faces=side1Faces1)
mdb.models['Model-1'].Coupling(name='PinnedSideConstraint',
    controlPoint=region1, surface=region2, influenceRadius=WHOLE_SURFACE,
    couplingType=KINEMATIC, localCsys=None, u1=ON, u2=ON, u3=ON, ur1=OFF,
    ur2=OFF, ur3=OFF)
mdb.save()

```

```

mdb.models['Model-1'].BuckleStep(name='Eigen_Buckling', previous='Initial',
    numEigen=50, vectors=58, maxIterations=100)
elemType1 = mesh.ElemType(elemCode=C3D8R, elemLibrary=STANDARD,
    kinematicSplit=AVERAGE_STRAIN, secondOrderAccuracy=OFF,
    hourglassControl=ENHANCED, distortionControl=DEFAULT)
elemType2 = mesh.ElemType(elemCode=C3D6, elemLibrary=STANDARD)
elemType3 = mesh.ElemType(elemCode=C3D4, elemLibrary=STANDARD)
p = mdb.models['Model-1'].parts['I150x150x5']
c = p.cells
cells = c.getSequenceFromMask(mask=('#ffff' ], ), )
pickedRegions =(cells, )
p.setElementType(regions=pickedRegions, elemTypes=(elemType1, elemType2,
    elemType3))
p = mdb.models['Model-1'].parts['I150x150x5']
p.seedPart(size=2.50, deviationFactor=0.1, minSizeFactor=0.1)
p = mdb.models['Model-1'].parts['I150x150x5']
p.generateMesh()
session.viewports['Viewport: 1'].view.setValues(nearPlane=1789.43,
    farPlane=2933.78, width=1075.64, height=584.024, viewOffsetX=56.3197,
    viewOffsetY=-58.5444)
a1 = mdb.models['Model-1'].rootAssembly
a1.regenerate()
a = mdb.models['Model-1'].rootAssembly
session.viewports['Viewport: 1'].setValues(displayedObject=a)
session.viewports['Viewport: 1'].assemblyDisplay.setValues(mesh=OFF, loads=ON,
    bcs=ON, predefinedFields=ON, connectors=ON)
session.viewports['Viewport: 1'].assemblyDisplay.meshOptions.setValues(
    meshTechnique=OFF)
a = mdb.models['Model-1'].rootAssembly
v1 = a.instances['I150x150x5-1'].vertices

```

```

verts1 = v1.getSequenceFromMask(mask=('[#0 #20000 ]', ), )
region = regionToolset.Region(vertices=verts1)
mdb.models['Model-1'].DisplacementBC(name='BC-LoadSide',
    createStepName='Initial', region=region, u1=SET, u2=SET, u3=SET,
    ur1=UNSET, ur2=UNSET, ur3=UNSET, amplitude=UNSET,
    distributionType=UNIFORM, fieldName="", localCsys=None)
a = mdb.models['Model-1'].rootAssembly
v1 = a.instances['I150x150x5-1'].vertices
verts1 = v1.getSequenceFromMask(mask=('[#0 #40000 ]', ), )
region = regionToolset.Region(vertices=verts1)
mdb.models['Model-1'].DisplacementBC(name='BC-PinnedSide',
    createStepName='Initial', region=region, u1=SET, u2=SET, u3=SET,
    ur1=UNSET, ur2=UNSET, ur3=SET, amplitude=UNSET,
    distributionType=UNIFORM, fieldName="", localCsys=None)
session.viewports['Viewport: 1'].assemblyDisplay.setValues(
    step='Eigen_Buckling')
mdb.models['Model-1'].boundaryConditions['BC-LoadSide'].setValuesInStep(
    stepName='Eigen_Buckling', u3=-20.0,
    buckleCase=PERTURBATION_AND_BUCKLING)
mdb.save()
import job
mdb.models['Model-1'].keywordBlock.synchVersions(storeNodesAndElements=False)
mdb.models['Model-1'].keywordBlock.replace(61, """
*Output, field, variable=PRESELECT
*NODE FILE
U""")
mdb.save()
session.viewports['Viewport: 1'].assemblyDisplay.setValues(loads=OFF, bcs=OFF,
    predefinedFields=OFF, connectors=OFF)
mdb.Job(name='Eigen Value', model='Model-1', description="", type=ANALYSIS,

```

```
atTime=None, waitMinutes=0, waitHours=0, queue=None, memory=90,  
memoryUnits=PERCENTAGE, getMemoryFromAnalysis=True,  
explicitPrecision=SINGLE, nodalOutputPrecision=SINGLE, echoPrint=OFF,  
modelPrint=OFF, contactPrint=OFF, historyPrint=OFF, userSubroutine="",  
scratch="", resultsFormat=ODB, multiprocessingMode=DEFAULT, numCpus=4,  
numDomains=4, numGPUs=0)
```

```
def OnlyResidualStressLeft():
```

```
    import section  
    import regionToolset  
    import displayGroupMdbToolset as dgm  
    import part  
    import material  
    import assembly  
    import step  
    import interaction  
    import load  
    import mesh  
    import optimization  
    import job  
    import sketch  
    import visualization  
    import xyPlot  
    import displayGroupOdbToolset as dgo  
    import connectorBehavior  
    session.viewports['Viewport: 1'].view.setValues(nearPlane=1556.03,  
        farPlane=2729.45, width=1311.24, height=679.055, viewOffsetX=-71.8191,  
        viewOffsetY=0.396545)  
    import job
```

```

mdb.models['Model-1'].keywordBlock.synchVersions(storeNodesAndElements=False)
mdb.models['Model-1'].keywordBlock.replace(62, ""
""")
mdb.save()
mdb.save()
a = mdb.models['Model-1'].rootAssembly
session.viewports['Viewport: 1'].setValues(displayedObject=a)
session.viewports['Viewport: 1'].assemblyDisplay.setValues(
    adaptiveMeshConstraints=ON)
del mdb.models['Model-1'].steps['Eigen_Buckling']
mdb.models['Model-1'].ExplicitDynamicsStep(name='LoadingE', previous='Initial',
    timePeriod=100.0, massScaling=((SEMI_AUTOMATIC, MODEL, AT_BEGINNING,
    0.0, 1e-06, BELOW_MIN, 0, 0, 0.0, 0.0, 0, None), ),
    improvedDtMethod=ON)
session.viewports['Viewport: 1'].assemblyDisplay.setValues(step='LoadingE')
mdb.save()
mdb.models['Model-1'].TabularAmplitude(name='Amp-1', timeSpan=STEP,
    smooth=SOLVER_DEFAULT, data=((0.0, 0.0), (1.0, 1.0)))
session.viewports['Viewport: 1'].assemblyDisplay.setValues(loads=ON, bcs=ON,
    predefinedFields=ON, connectors=ON, adaptiveMeshConstraints=OFF)
mdb.models['Model-1'].boundaryConditions['BC-LoadSide'].setValuesInStep(
    stepName='LoadingE', u3=-20.0, amplitude='Amp-1')
mdb.save()
session.viewports['Viewport: 1'].assemblyDisplay.setValues(mesh=ON, loads=OFF,
    bcs=OFF, predefinedFields=OFF, connectors=OFF)
session.viewports['Viewport: 1'].assemblyDisplay.meshOptions.setValues(
    meshTechnique=ON)
p = mdb.models['Model-1'].parts['I150x150x5']
elemType1 = mesh.ElemType(elemCode=C3D8R, elemLibrary=EXPLICIT,
    kinematicSplit=AVERAGE_STRAIN, secondOrderAccuracy=OFF,

```

```

hourglassControl=ENHANCED, distortionControl=DEFAULT)
elemType2 = mesh.ElemType(elemCode=C3D6, elemLibrary=EXPLICIT)
elemType3 = mesh.ElemType(elemCode=C3D4, elemLibrary=EXPLICIT)
p = mdb.models['Model-1'].parts['I150x150x5']
c = p.cells
cells = c.getSequenceFromMask(mask=('[#ffff ]', ), )
pickedRegions =(cells, )
p.setElementType(regions=pickedRegions, elemTypes=(elemType1, elemType2,
elemType3))
mdb.save()
a = mdb.models['Model-1'].rootAssembly
a.regenerate()
session.viewports['Viewport: 1'].setValues(displayedObject=a)
session.viewports['Viewport: 1'].assemblyDisplay.setValues(mesh=OFF,
adaptiveMeshConstraints=ON)
session.viewports['Viewport: 1'].assemblyDisplay.meshOptions.setValues(
meshTechnique=OFF)
mdb.models['Model-1'].fieldOutputRequests['F-Output-1'].setValues(variables=(
'S', 'MISES', 'PEEQ', 'LE', 'U', 'RF'), timeInterval=0.05)
mdb.models['Model-1'].historyOutputRequests['H-Output-1'].setValues(variables=(
'ALLIE', 'ALLKE'), timeInterval=0.05)
mdb.save()
mdb.save()
session.viewports['Viewport: 1'].assemblyDisplay.setValues(
adaptiveMeshConstraints=OFF)
mdb.Job(name='Final_LocalBuckling', model='Model-1', description="",
type=ANALYSIS, atTime=None, waitMinutes=0, waitHours=0, queue=None,
memory=90, memoryUnits=PERCENTAGE, explicitPrecision=DOUBLE_PLUS_PACK,
nodalOutputPrecision=SINGLE, echoPrint=OFF, modelPrint=OFF,
contactPrint=OFF, historyPrint=OFF, userSubroutine="", scratch="",

```

```
resultsFormat=ODB, parallelizationMethodExplicit=DOMAIN, numDomains=4,  
activateLoadBalancing=False, multiprocessingMode=DEFAULT, numCpus=4)  
mdb.save()  
mdb.models['Model-1'].keywordBlock.synchVersions(storeNodesAndElements=False)  
mdb.models['Model-1'].keywordBlock.replace(50, ""  
** -----  
**  
** STEP: LoadingE  
**  
*IMPERFECTION, FILE=EigenValue, STEP=1  
1,1.5875""")  
mdb.save()  
mdb.save()
```

APPENDIX E – CALCULATION OF NOMINAL COMPRESSIVE STRENGTH

Calculation of AISC nominal compressive strength for 100 ksi W12×12×0.6×0.6 built-up section:

$$\begin{aligned}
 E &:= 29000 \text{ ksi} & F_y &:= 100 \text{ ksi} & b_f &:= 12.598 \text{ in} & t_f &:= 0.551 \text{ in} \\
 d &:= 12.598 \text{ in} & t_w &:= 0.551 \text{ in} & L_c &:= 35.197 \text{ in} & h_0 &:= 11.496 \text{ in} \\
 \lambda_f &:= 11.432 & \lambda_w &:= 20.864 & G &:= 11200 \text{ ksi} & J &:= 2.077 \text{ in}^4 \\
 I_x &:= 573.822 \text{ in}^4 & I_y &:= 183.774 \text{ in}^4 & r_x &:= 5.313 \text{ in} & r_y &:= 3.007 \text{ in} \\
 C_w &:= 6661.975 \text{ in}^6 & \frac{L_c}{r_x} &= 6.625 & \frac{L_c}{r_y} &= 11.705 & k_c &:= 0.876 & A_g &:= 20.329 \text{ in}^2 \\
 \lambda_{rw} &:= 1.49 \cdot \sqrt{\frac{E}{F_y}} & \lambda_{rw} &= 25.374 & \lambda_{rw} &> \lambda_w & \text{web is non-slender} \\
 \lambda_{rf} &:= 0.64 \cdot \sqrt{\frac{E \cdot k_c}{F_y}} & \lambda_{rf} &= 10.201 & \lambda_{rf} &< \lambda_f & \text{Flange is slender}
 \end{aligned}$$

From section E3 of AISC (2016) *Specification*: Flexural Buckling

$$F_{ex} := \frac{\pi^2 E}{\left(\frac{L_c}{r_x}\right)^2} \quad F_{ex} = 6521.779 \text{ ksi} \quad (\text{E4-5})$$

$$F_{ey} := \frac{\pi^2 E}{\left(\frac{L_c}{r_y}\right)^2} \quad F_{ey} = 2089.071 \text{ ksi} \quad (\text{E4-6})$$

$$\lambda_l := 4.71 \sqrt{\frac{E}{F_y}} \quad \lambda_l = 80.208$$

$$\frac{L_c}{r_x} < \lambda_1 \quad F_{crx} := \left(0.658 \frac{F_y}{F_{ex}}\right) F_y \quad (\text{E3-2})$$

$$F_{crx} = 99.36 \text{ ksi}$$

$$\frac{L_c}{r_y} < \lambda_1 \quad F_{cry} := \left(0.658 \frac{F_y}{F_{ey}}\right) F_y \quad F_{cry} = 98.016 \text{ ksi} \quad F_{cr} := \min(F_{crx}, F_{cry})$$

$$P_n := F_{cr} \cdot A_g \quad (\text{E3-1})$$

$$P_n = 1992.576 \text{ kip}$$

From section E7 of AISC (2016) *Specification*: Local Buckling

$$c_1 := 0.22 \quad c_2 := 1.49 \quad F_{cr} = 98.016 \text{ ksi} \quad F_y = 100 \text{ ksi}$$

$$\lambda_{rf} \cdot \sqrt{\frac{F_y}{F_{cr}}} = 10.303 \quad \lambda_{rw} \cdot \sqrt{\frac{F_y}{F_{cr}}} = 25.629$$

$$F_{elf} := \left(c_2 \cdot \frac{\lambda_{rf}}{\lambda_f}\right)^2 \cdot F_y \quad F_{elf} = 176.763 \text{ ksi} \quad (\text{E7-5})$$

$$F_{elw} := \left(c_2 \cdot \frac{\lambda_{rw}}{\lambda_w}\right)^2 \cdot F_y \quad F_{elw} = 328.358 \text{ ksi}$$

$$\sqrt{\frac{F_{elf}}{F_{cr}}} = 1.343 \quad \sqrt{\frac{F_{elw}}{F_{cr}}} = 1.83$$

$$\lambda_f < \lambda_{rf} \cdot \sqrt{\frac{F_y}{F_{cr}}} \quad b_e := b_f \cdot \left(1 - c_1 \cdot \sqrt{\frac{F_{elf}}{F_{cr}}}\right) \cdot \sqrt{\frac{F_{elf}}{F_{cr}}} \quad (\text{E7-3})$$

$$b_e = 11.92 \text{ in}$$

$$\lambda_w > \lambda_{rw} \cdot \sqrt{\frac{F_y}{F_{cr}}} \quad h_e := h_0 \quad (E7-2)$$

$$h_e = 11.496 \text{ in} \quad A_e := 2 \cdot b_e \cdot t_f + h_e \cdot t_w \quad A_e = 19.47 \text{ in}^2$$

$$P_n := F_{cr} \cdot A_e \quad (E7-1)$$

$$P_n = 1908.361 \text{ kip}$$

So P_n from local buckling controls

$$P_n = 1908.361 \text{ kip}$$

APPENDIX F – AXIAL LOAD VS AXIAL DISPLACEMENT CURVES

This section gives a brief information on the comparison of axial load with axial deformation curves for built-up W shapes. This section also provides information on the comparison of normalized axial load with axial deformation of hot-rolled W shapes.

F.1 Axial load vs axial deformation curves for built-up W shapes

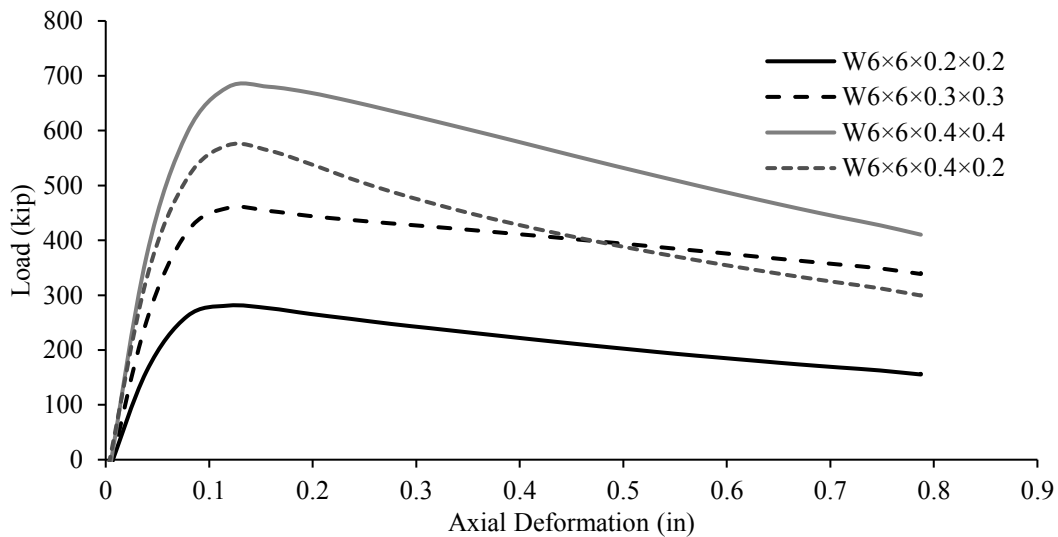


Fig. F 1: Axial load vs. axial deformation for W6x6 built-up stub columns of grade 100 ksi

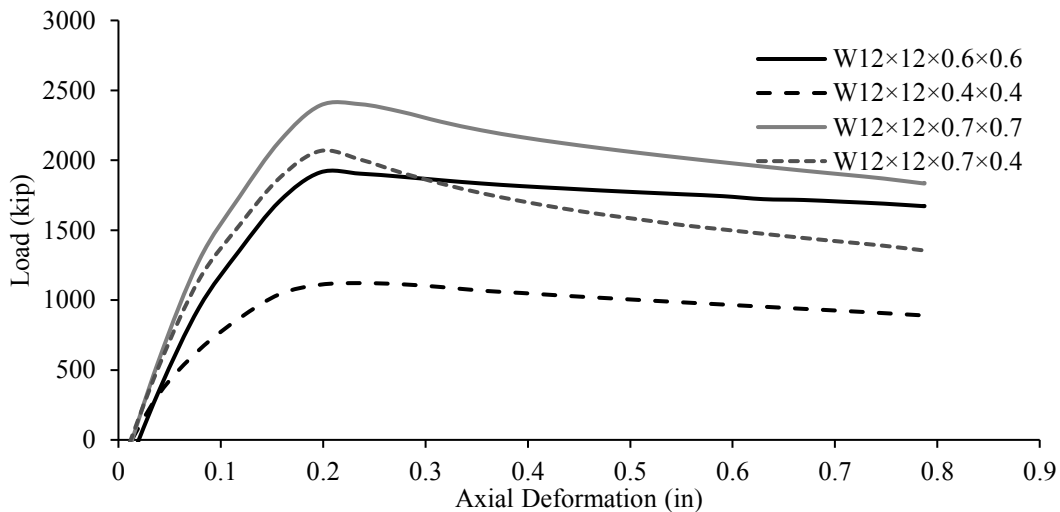


Fig. F 2: Axial load vs. axial deformation for W12x12 built-up stub columns of grade 100 ksi

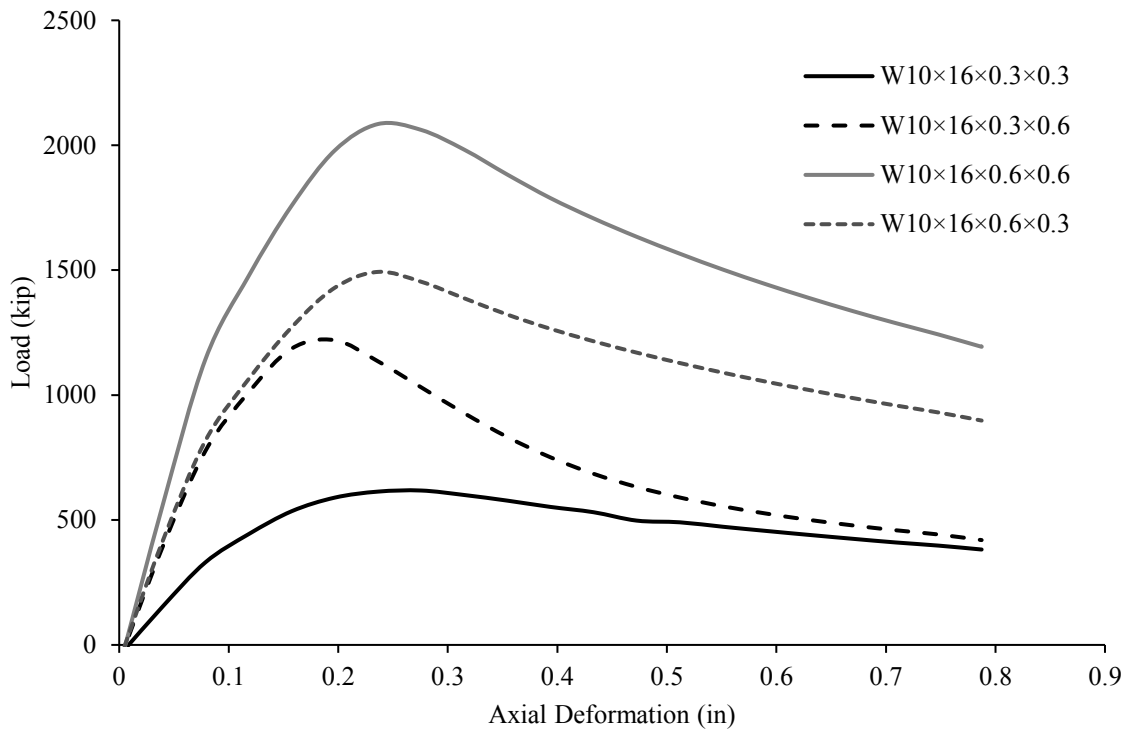


Fig. F 3: Axial load vs. axial deformation for W10×16 built-up stub columns of grade 100 ksi

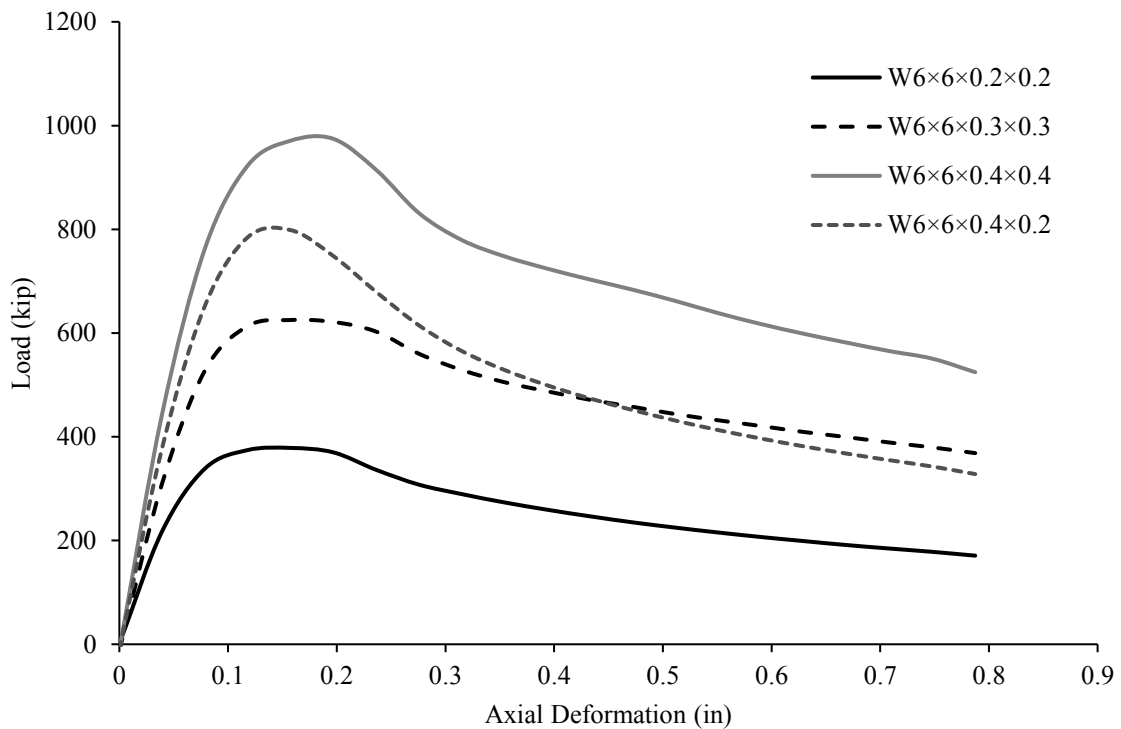


Fig. F 4: Axial load vs. axial deformation for W6×6 built-up stub columns of grade 140 ksi

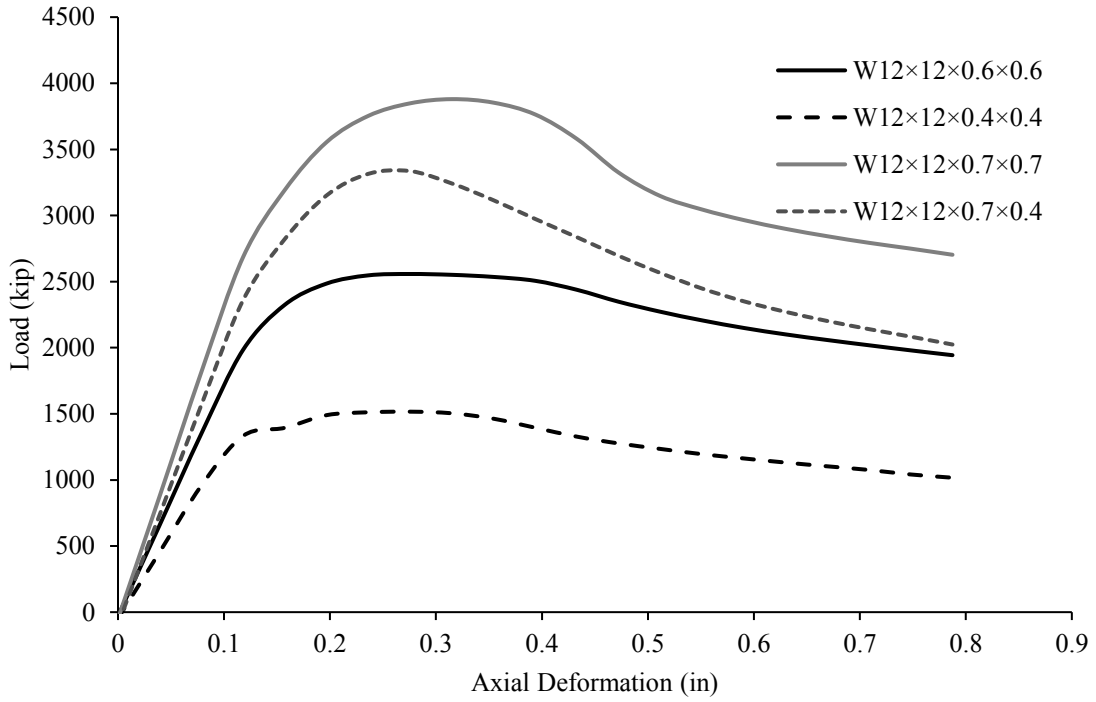


Fig. F 5: Axial load vs. axial deformation for W12x12 built-up stub columns of grade 140 ksi

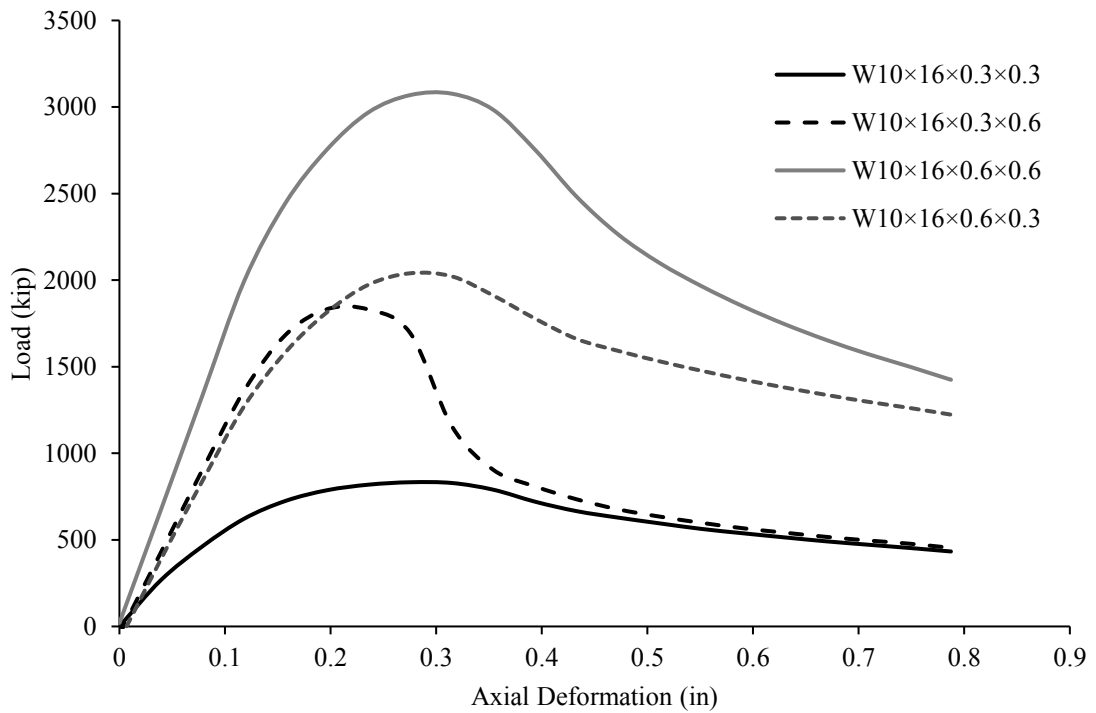


Fig. F 6: Axial load vs. axial deformation for W10x16 built-up stub columns of grade 140 ksi

F.2 Normalized axial load vs axial deformation for hot-rolled W shapes

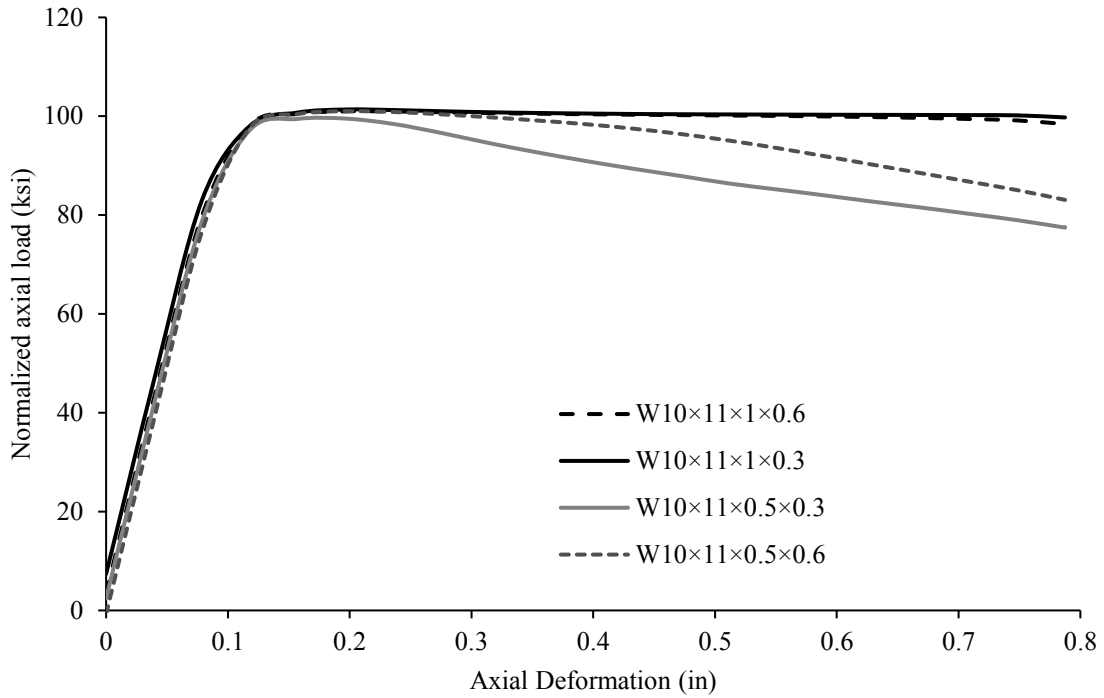


Fig. F 7: Normalized axial load vs. axial deformation for W10x11 hot-rolled stub columns of grade 100 ksi

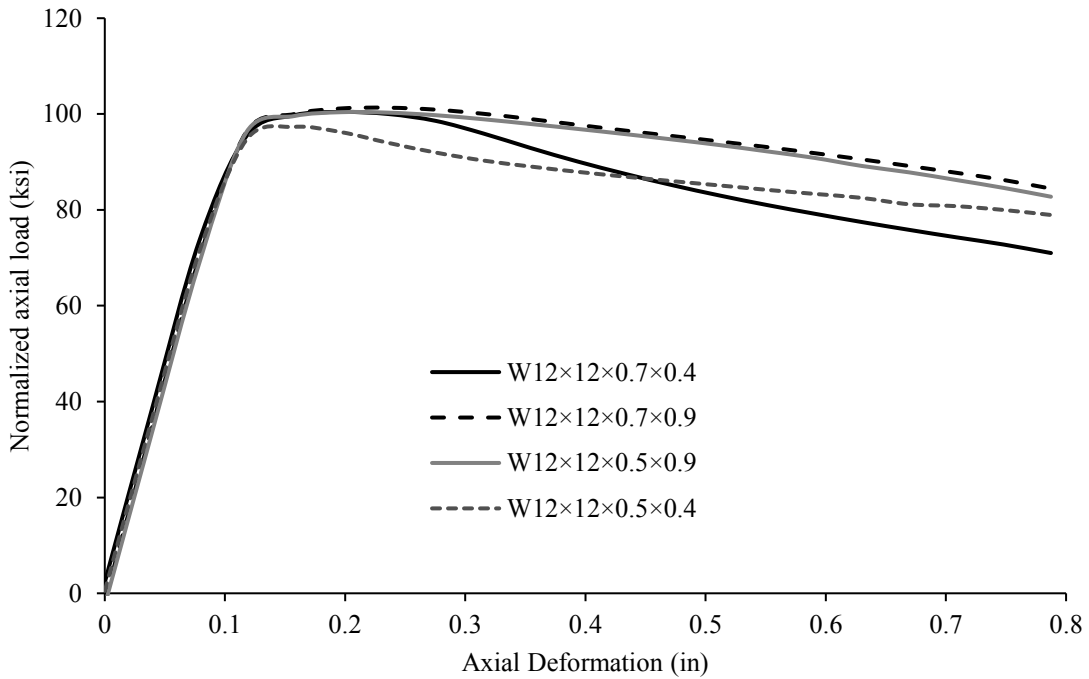


Fig. F 8: Normalized axial load vs. axial deformation for W12x12 hot-rolled stub columns of grade 100 ksi

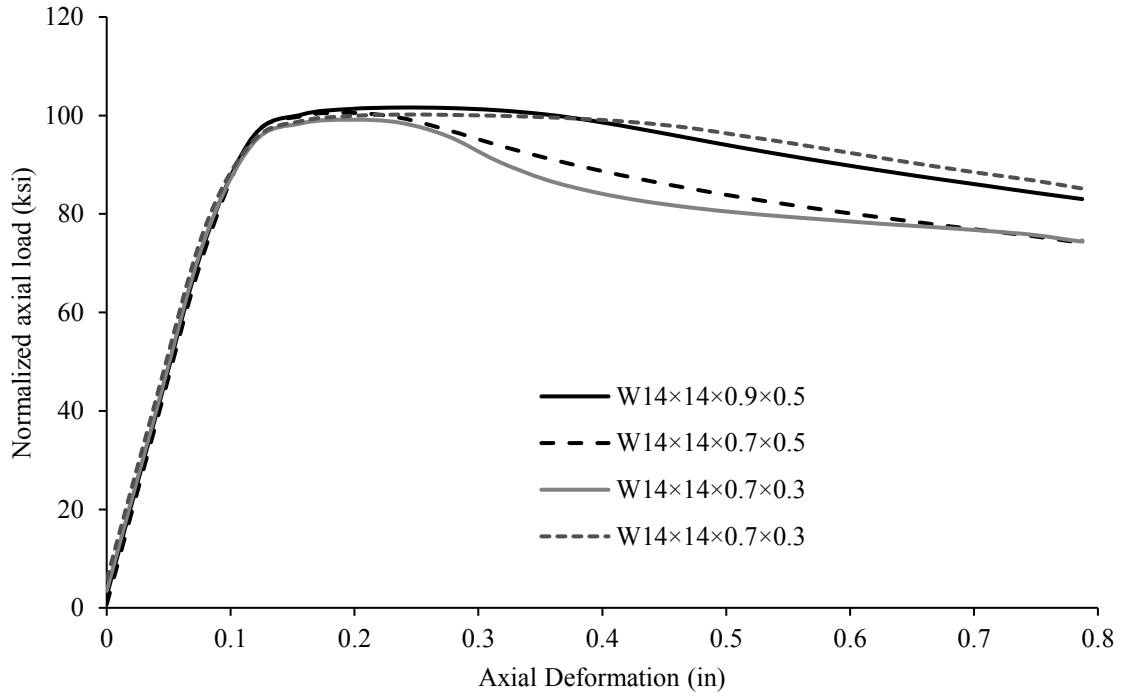


Fig. F 9: Normalized axial load vs. axial deformation for W14×14 hot-rolled stub columns of grade 100 ksi

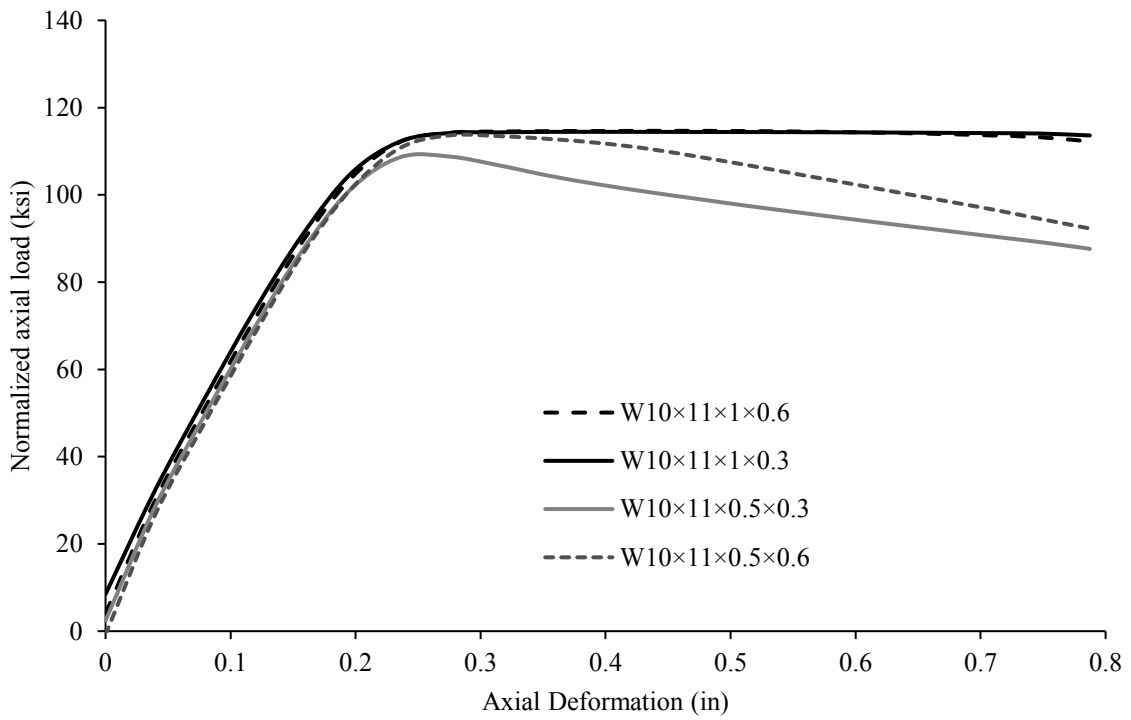


Fig. F 10: Normalized axial load vs. axial deformation for W10×11 hot-rolled stub columns of grade 120 ksi

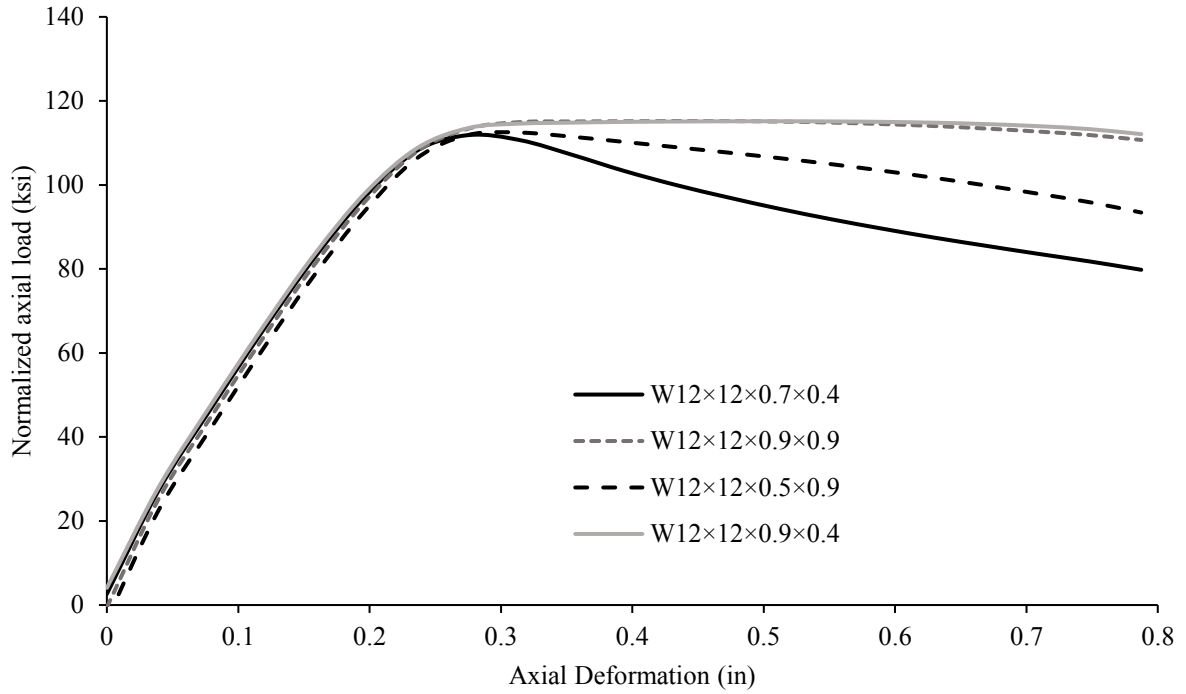


Fig. F 11: Normalized axial load vs. axial deformation for W12x12 hot-rolled stub columns of grade 120 ksi

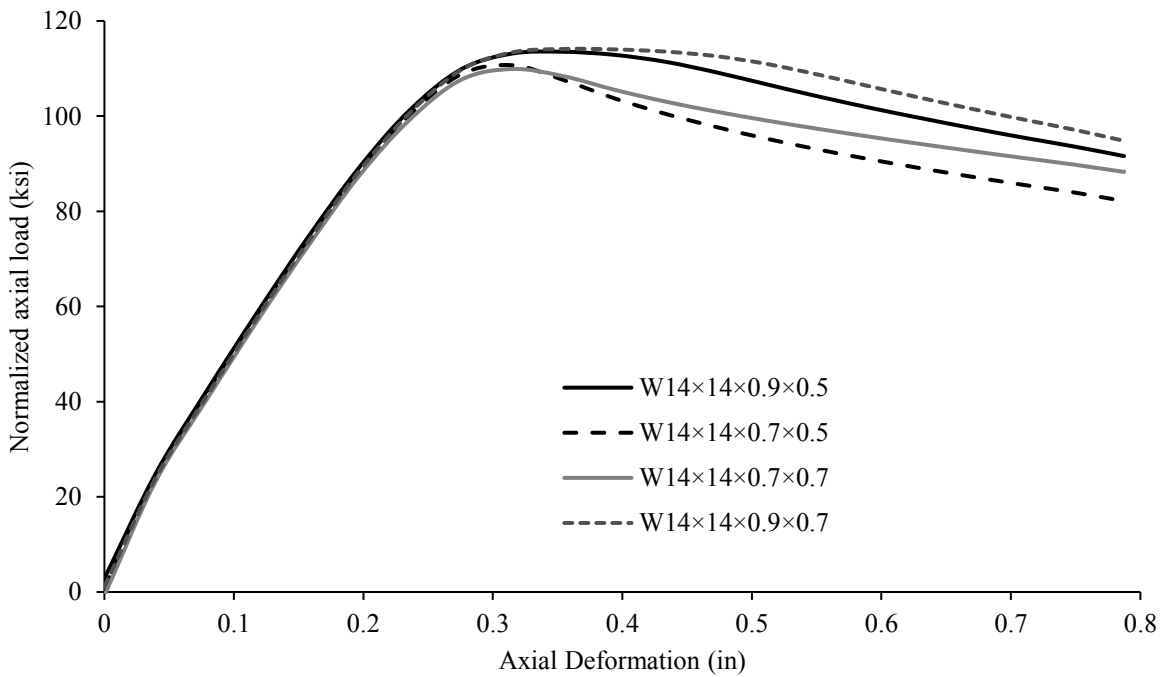


Fig. F 12: Normalized axial load vs. axial deformation for W14x14 hot-rolled stub columns of grade 120 ksi